Title
Biological applications of the SQUID microscope

Author
Chemla, Yann Robert

Publication Date
2001-05-01

LBNL-47923

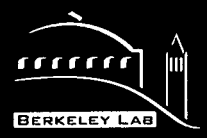

ERNEST ORLANDO LAWRENCE
BERKELEY NATIONAL LABORATORY

Biological Applications of the SQUID Microscope

Yann R. Chemla

Materials Sciences Division

May 2001

Ph.D. Thesis

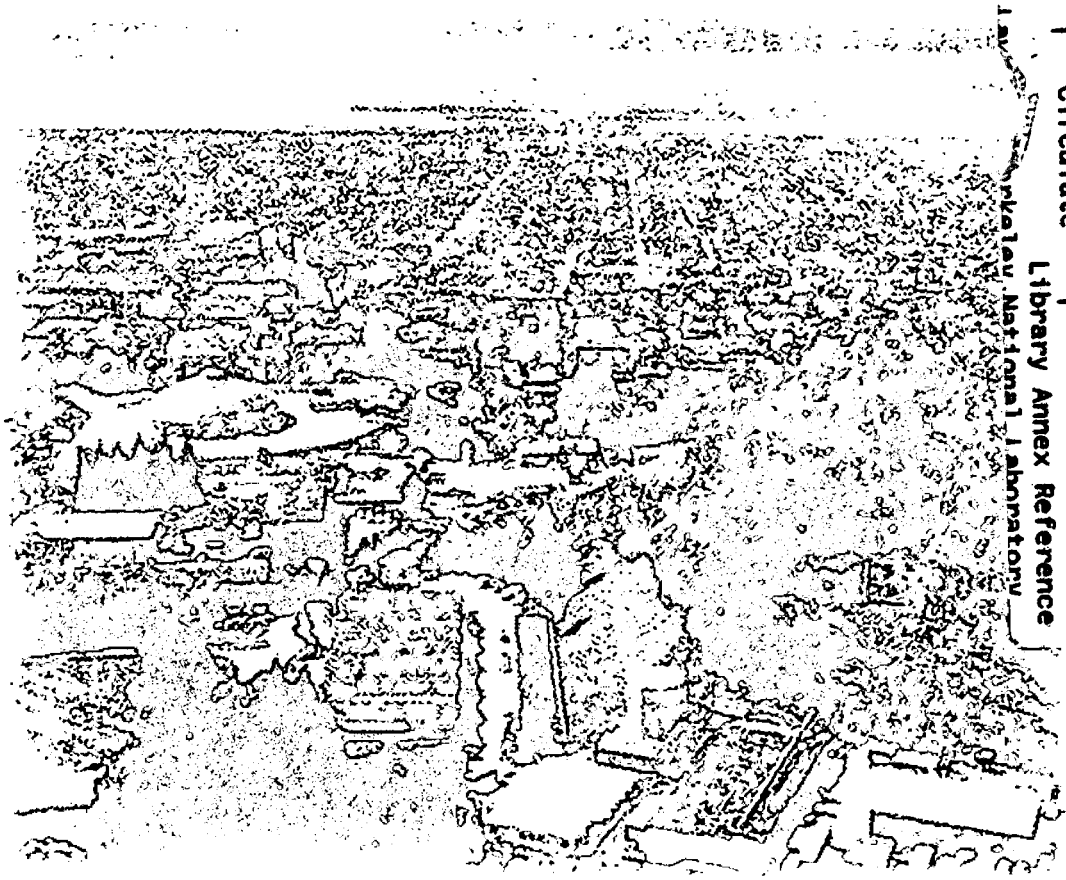

DISCLAIMER

LBNL-47923

Biological Applications of the SQUID Microscope

Yann Robert Chemla
(Ph.D. Thesis)

Department of Physics, University of California
and
Materials Sciences Division
Lawrenece Berkeley National Laboratory
University of California
Berkeley, CA 94720

May 2001

This work was supported by the Office of Basic Energy Sciences, Materials Sciences Division of the U.S. Department of Energy under contract number DE-AC03-76SF00098.

Biological Applications of the SQUID Microscope

by

Yann Robert Chemla

B.S. (Yale University) 1993
M.A. (University of California, Berkeley) 2000

A dissertation submitted in partial satisfaction of the
requirements for the degree of
Doctor of Philosophy

in

Physics

in the

GRADUATE DIVISION
of the
UNIVERSITY of CALIFORNIA at BERKELEY

Committee in charge:

Professor John Clarke, Chair
Professor Daniel S. Rohksar
Professor Harold Lecar

Spring 2001

Abstract

Biological Applications of the SQUID Microscope

by

Yann Robert Chemla

Doctor of Philosophy in Physics

University of California at Berkeley

Professor John Clarke, Chair

The recently developed "microscope" based on a high-T_c dc SQUID (Superconducting QUantum Interference Device) is used to detect the magnetic fields produced by biological samples maintained at room temperature and atmospheric pressure. The microscope consists of a SQUID placed on the end of a sapphire "cold finger" thermally anchored to a liquid nitrogen reservoir inside a vacuum enclosure. A 3-μm thick silicon nitride (SiN) membrane, located above the SQUID, acts as a vacuum window. Room temperature samples are placed on top of the window and can be brought within 15μm of the SQUID.

In Part I, the SQUID microscope is used to investigate magnetotactic bacteria, microorganisms which possess a permanent dipole moment. The magnetic field produced by the motion of the bacteria in growth medium is detected by the SQUID in the microscope. Measurements are performed on both motile and nonmotile bacteria. In the nonmotile case, we obtain the power spectrum of the magnetic flux noise produced by the rotational Brownian motion of the ensemble of bacteria. Furthermore, we measure the time-dependent flux produced by the ensemble in response to an applied uniform magnetic field. In the motile case, we obtain the magnetic flux power spectra produced by the swimming bacteria. Combined, these measurements determine the average rotational drag coefficient, magnetic moment, and the frequency and amplitude of the vibrational and rotational modes of the bacteria in a unified set of measurements. In addition, the microscope can easily resolve the motion of a single bacterium. This technique can be extended to any biological substance to which a suitable magnetic label can be attached.

In Part II, a technique is described for the specific, sensitive, quantitative, and

rapid detection of biological targets using superparamagnetic nanoparticle labels. In this technique, a mylar film to which the targets have been bound is placed on the microscope, typically $40\mu m$ from the SQUID. A suspension of magnetic nanoparticles carrying antibodies directed against the target is added to the mixture in the well, and one-second pulses of magnetic field are applied parallel to the SQUID. In the presence of this aligning field the nanoparticles develop a net magnetization, which relaxes when the field is turned off. Unbound nanoparticles relax rapidly by Brownian rotation and contribute no measurable signal. Nanoparticles that are bound to the target on the film are immobilized and undergo Néel relaxation, producing a slowly decaying magnetic flux which is detected by the SQUID. The ability to distinguish between bound and unbound labels allows one to run homogeneous assays, which do not require separation and removal of unbound magnetic particles. The technique has been demonstrated with a model system of liposomes carrying the FLAG epitope. The SQUID microscope requires no more than $(5\pm2)\times10^4$ magnetic nanoparticles to register a reproducible signal.

Improvements to the SQUID microscope designed to increase its sensitivity are discussed. An experiment is proposed in which the microscope is used as a single molecule probe, detecting a single magnetic label attached to a biological macromolecule like DNA.

Contents

List of Figures

List of Tables

List of Symbols

α_r, α_t ..... rotational, and translational drag coefficients

A_{eff} ..... SQUID effective area

C_Φ ..... flux autocorrelation function

D_r, D_t ..... rotational, and translational diffusion coefficients

ΔV ..... modulation depth of SQUID

η ..... viscosity of water

$\bar{f}_p, \bar{f}_v$ ..... frequencies of precessional, and vibrational modes of bacteria

$\mathcal{G}^{(s)}, \mathcal{G}^{(r)}, \mathcal{G}^{(2D)}$ ..... geometrical factors for the noise spectrum, response function of a 3D sample, and response function of a 2D sample

θ, ϕ ..... polar, and azimuthal angle

I_c ..... critical current

k_B ..... Boltzmann's constant

$L(\xi)$ ..... Langevin function

ℓ_{eff} ..... SQUID effective size; $(A_{eff})^{1/2}$

m ..... magnetic dipole moment

μ_o ..... permitivity of free space

ν ..... exponent in falloff of spectrum

$P(\{q\}, t|\{q_o\}, 0)$ ..... conditional probability density for the set of dynamical variables $\{q\}$

ρ_b ..... bacterial density

ρ_m, σ_m ..... magnetic dipole density, magnetic dipole surface density

S_Φ ..... flux noise power spectrum

τ_o ..... Brownian relaxation time

$\tau_{B,\|}, \tau_{B,\perp}$ ..... relaxation times for components parallel, and perpendular to a field

τ_m ..... relaxation time for motile bacteria

τ_N ..... Néel relaxation time

T_c ..... critical temperature of a superconductor

ϕ_p, ϕ_v ..... amplitude of precessional, and vibrational modes of bacteria

Φ, Φ_o ..... magnetic flux, magnetic flux quantum

Φ_s ..... Néel relaxation signal amplitude

Ω ..... $\{\theta, \phi\}$; solid angle

$W_1(\{q\}, t)$ ..... probability distribution for the set of dynamical variables $\{q\}$

$W_2(\{q\}, t; \{q_o\}, 0)$ ..... joint probability distribution for the set of dynamical variables $\{q\}$

W_{st} ..... stationary or equilibrium probability distribution

ξ ..... ratio of magnetic alignment energy to thermal energy mB/k_BT

z_o ..... minimum SQUID-to-sample separation

Acknowledgements

I am deeply indebted to my advisor, Professor John Clarke, for his support and generosity over these last 6 years, and for the invaluable research experience I have gained in his group. I gratefully acknowledge the Department of Energy's Lawrence Berkeley National Laboratory for their financial support.

I feel very fortunate to have worked with my fellow Clarke group members, whose intelligence and good humor have made these years at Berkeley both stimulating and fun. I am deeply grateful to Tom Lee, who, in my first year of research, taught me everything I wanted to know but was afraid to ask about SQUIDs and the SQUID microscope, which he had designed and built. Helene Grossman and I spent many hours working together on the bacteria and the magnetic immunoassay experiments, taking data and maintaining the SQUID microscope. I leave SQUID microscopy in her able hands. Robert McDermott fabricated the SQUIDs used in the magnetic immunoassay experiment. His fabrication skills are only surpassed by his singing abilities. I thank all of the graduate students, postdocs, and guests that have been in the Clarke group during these past 6 years. I valued their friendship and comradery, and enjoyed our many discussions together (scientific or otherwise) with the occasional pint of beer.

This work would not have been possible without the hard work of many collaborators. I am very grateful to Mike Adamkiewicz and Wanda Rivera in Prof. Bob Buchanan's research group in the Dept. of Plant and Microbial Biology for their help with magnetotactic bacteria. Prof. Dennis Bazylinski from Iowa State University kindly provided us with starting cultures and a growth protocol. Yan Poon, in Prof. Ray Stevens' research group in the Dept. of Chemistry, and Prof. Mark Alper at the Material Sciences Division at Lawrence Berkeley National Laboratory were indispensable in the magnetic immunoassay experiments. I would also like to thank Prof. Richard Frankel, Prof. Howard Berg, Richard Bruehl, Prof. Carolyn Bertozzi, and Mark DiIorio for helpful discussions. I must also acknowledge the many excellent facilities here at Berkeley: the National Center for Electron Microscopy (NCEM), the Berkeley Microfabrication Laboratory, the Physics Department Machine Shop and Electronic Shop, and the Triple Rock Microbrewery.

Lastly, I would like to thank my parents for their endless love and support, and for giving me a place to eat and do laundry when I didn't feel like cooking for myself or going to the laundromat.

Chapter 1

Introduction

Many materials, when cooled below a critical temperature T_c, undergo a phase transition to the superconducting state, exhibiting such properties as infinite dc conductivity and perfect diamagnetism. Numerous solid-state devices based on superconducting materials and their properties have been developed. Superconducting QUantum Interference Devices (SQUIDs) can detect extraordinarily small changes in magnetic flux. Such devices can be applied to any sample that can generate a magnetic flux.

However, the need to cool superconducting devices to cryogenic temperatures has considerably limited their use outside of low-temperature physics. SQUID applications in which a sample is maintained at room temperature and atmospheric pressure require the SQUID to be thermally isolated from the sample. At the same time, the separation between the two must often be minimized to maximize the flux coupled into the SQUID. Prior to 1986, the low transition temperatures of all known superconductors ($T_c \leq 23K$), requiring the use of liquid helium (4K) as cryogen, made this a formidable task. The discovery of cuprate superconductors (called high-T_c materials) in that year with a transition temperature above the boiling point of nitrogen (77K) has made the thermal isolation of a SQUID from a room-temperature sample much more manageable.

We have constructed a "SQUID microscope" in which a high-T_c SQUID can be placed within $15\mu m$ of a sample at room temperature and atmospheric pressure. This extraordinarily small separation offers unprecedented sensitivity to magnetic fields produced by nearby specimens maintained at room temperature. This technical advance has made possible the investigation of live biological samples with a SQUID microscope. In this thesis I will describe an experiment on magnetotactic bacteria, a microorganism possessing

a permanent magnetic dipole moment, using the SQUID microscope [1]. As an extension of this work, techniques to magnetically label biological substances have been studied. I will describe the development of a sensitive magnetic immunoassay—a detection technique for specific biological targets—based on the SQUID microscope [2].

This thesis is broken up into two parts, each dedicated to the two experiments described above. These introductory words and Chapters 2 and 3 make up a preamble meant to introduce the reader to the experiments and the various apparatus used in this work. Chapter 2 is a rather short discussion on the principles of operation, practical implementations, and design of high-T_c dc SQUIDs. For a more complete overview, refer to the excellent review article by Koelle *et al.* [3]. Chapter 3 discusses the high-T_c SQUID microscope in some detail, in particular, the design and fabrication of the vacuum window assembly and of the SQUIDs dedicated to the microscope. The article by Lee *et al.* [4] nicely complements this chapter.

Part I begins with Chapter 4, a comprehensive overview of magnetotactic bacteria: a historical perspective and a review of the experiments and current understanding. There is a detailed section at the end of the chapter on the cultivation and harvesting protocol for the bacteria which should appeal only to students interested in reproducing these experiments. Chapter 5 presents the experimental results of the magnetotactic bacteria study. Many, though not all, of these results have been published [1]. Part II is dedicated to the second experiment. Chapter 6 is an introduction to magnetic labeling and immunoassays. Again, a lengthy discussion on the sample preparation protocol is included, and may not be interesting to the casual reader. Chapter 7 presents the results from the SQUID microscope magnetic immunoassay experiment. Most of these results also have been published [2]. Chapter 8 summarizes the main results of the two experiments and suggests possible future directions for research in this area.

Three Appendices document the extensive theoretical work done in modeling the experimental results. Apart from Section C.2 of Appendix C, which appears in [1], none of these calculations have been published. Again, this section may be too dense and detailed for casual readers. Appendix A addresses the issue of magnetic coupling between samples of various geometries and the SQUID in a SQUID microscope. Appendices B and C model the dynamical behavior—and its effect on the SQUID—of dead and live magnetotactic bacteria, respectively.

Chapter 2

Superconducting Quantum Interference Devices

2.1 Introduction

The unique properties of superconductors have led to the development of a wide array of superconducting devices used in a variety of applications. Among those, Superconducting QUantum Interference Devices (SQUIDs) are the most sensitive detectors of magnetic flux. They can be applied to any quantity which can be converted to a flux; magnetic field, magnetic susceptibility, current, voltage, etc. [5]. For instance, as detectors of magnetic field, SQUIDs are often inductively coupled to a superconducting pickup loop in order to increase their area, and thus improve their field sensitivity. In this way, SQUIDs have been fabricated with a magnetic field noise as low as $\sim 1fT/\sqrt{Hz}$, sufficient to detect the magnetic fields produced by the human brain. To give a sense of scale to this extraordinary sensitivity, consider that a field of $1fT$ is over ten orders of magnitude smaller than the Earth's magnetic field.

SQUIDs have been applied to a dizzying variety of fields: low-temperature physics, nuclear magnetic resonance, neurobiology, geophysics, material science, cosmology, and most recently, quantum computing, just to name a few. The discovery of high-transition temperature (HTS) superconductors in 1986 led to a flurry of research activity in the field. Chief amongst those research efforts was the development of Superconducting QUantum Interference Devices made out of high-T_c materials. Nowadays, high-T_c SQUIDs made

of thin films of the material $YBa_2Cu_3O_{7-\delta}$ (YBCO) are routinely fabricated in our own laboratory. Their higher critical temperature is a double-edged sword, however; they can be operated in liquid nitrogen, greatly simplifying cryogenic considerations, but they are intrinsically more noisy than their low-T_c counterparts.

In the remainder of this chapter, I will describe the characteristics and operating principles of Superconducting QUantum Interference Devices and discuss the high-T_c devices used specifically in this thesis. Generally speaking, SQUIDs come in two classes: dc [6], which are biased with a constant current, and rf [7], which are operated with a radiofrequency flux bias. Despite subtle differences in operation, both act as sensitive detectors of magnetic flux. For the purposes of this thesis, however, I will only discuss the dc SQUID, which is the type used in our experiments.

2.2 The dc SQUID

2.2.1 Principle of operation

A schematic of the dc SQUID is shown in Fig. 2.1(a). The device consists of a superconducting loop of inductance L interrupted by two parallel Josephson junctions. These junctions are thin insulating barriers in which superconductivity is locally suppressed (typically, these consist of an insulating material, a normal metal, or a grain boundary). The macroscopic quantum coherence of the superconducting state is, however, sufficiently long-range that superconducting electron pairs may tunnel across the junctions.

The behavior of the SQUID relies on two important properties of superconductors: the Josephson effect and flux quantization. If a Josephson junction is biased with a current I less than a certain threshhold I_c, called the critical current, no voltage appears across the barrier and the junction is said to be in the superconducting state. For I greater than I_c, a voltage develops and the junction is in the resistive state. Flux quantization describes the property that requires the magnetic flux Φ through a loop of solid superconductor to be quantized in units of $\Phi_o \equiv h/2e \approx 2 \times 10^{-15}\, T \cdot m^2$.

In a dc SQUID, the flux Φ may take on any value since the superconducting loop is interrupted by two Josephson junctions, but the critical current of the two parallel junctions oscillates as a function of Φ with a period of Φ_o. As shown in Fig. 2.1(b), the I-V characteristics of the dc SQUID resemble that of a single Josephson junction. There is a

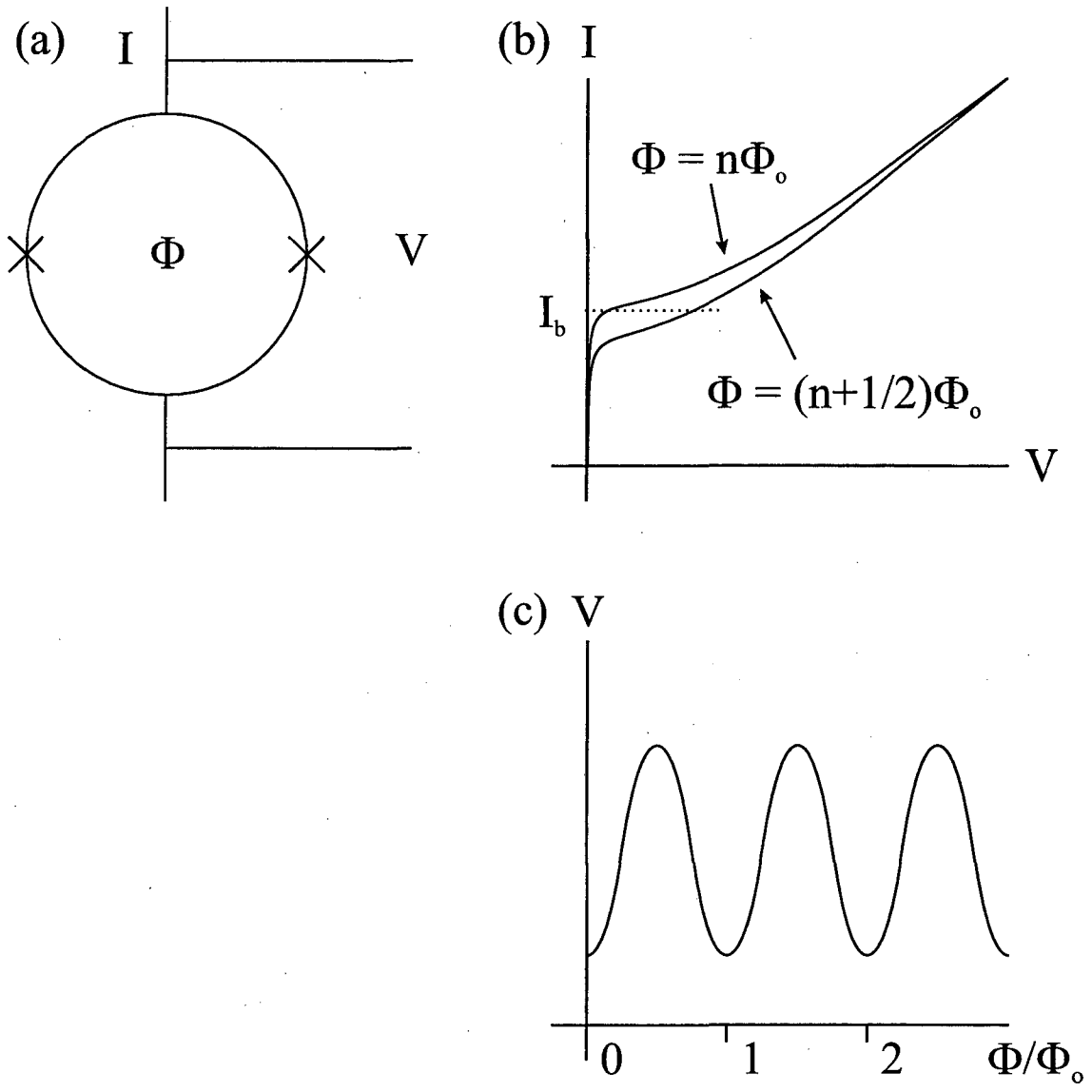

Figure 2.1: The dc SQUID. The schematic (a) shows a superconducting loop interrupted by two parallel Josephson junctions. The I-V characteristics (b) are modulated by the flux in the loop. By biasing the SQUID at an appropriate current I_b, the voltage (c) is an oscillating function of flux Φ with period Φ_o.

crossover at current I_c from the superconducting state to the resistive state (which has a resistance R_n), but the crossover is modulated by the flux. The upper branch of the I-V curve in Fig. 2.1(b), in which the critical current is maximum, occurs for $\Phi = n\Phi_o$; the lower branch, where the critical current is minimum, occurs for $\Phi = (n + 1/2)\Phi_o$. Thus, when the SQUID is biased with a current $I_b \gtrsim I_c^{max}$, the voltage generated across the loop is a periodic function of Φ with a peak-to-peak amplitude ΔV [see Fig. 2.1(c)], called the V-Φ curve. Thus, it is convenient to think of the SQUID as a flux-to-voltage transducer.

It is in general possible to detect a change in flux much smaller than $1\Phi_o$. If the SQUID is biased at a point in the V-Φ curve with the maximum slope, denoted by V_Φ, a small change in flux $\delta\Phi \ll \Phi_o$ produces a voltage $\delta V = V_\Phi \delta\Phi$. The flux-to-voltage transfer coefficient V_Φ is approximately given by R_n/L, as a general rule of thumb[1]. Note that for a sinusoidal V-Φ curve, $V_\Phi = \pi\Delta V/\Phi_o$. A well-designed SQUID may have a flux-to-voltage transfer coefficient $V_\Phi = 100\mu V/\Phi_o$ so that a $10\mu\Phi_o$ flux change would produce a $1nV$ voltage, which can be detected with standard electronics.

2.2.2 The flux-locked loop and flux modulation

As described above, the dc SQUID would not be a practical device since its voltage response to flux is not linear but oscillatory. A signal flux can only be measured within an integer number of Φ_o, effectively limiting the dynamic range to $\Phi \lesssim \Phi_o/2$. As a result, it is standard practice to operate the SQUID in a feedback loop, in which the signal flux is cancelled out by a feedback coil inductively coupled to the device. The current needed to cancel the flux is read out, and is proportional to the signal flux. In this way, the dynamic range of the SQUID can be extended to quantities much larger than $1\Phi_o$. This read-out scheme is called the "flux-locked loop".

The voltage across the SQUID is amplified in several stages before being read out. It is important to ensure that the gain stages do not contribute significantly to the noise of the system. While this is not a problem at high frequencies, 1/f noise in amplifiers is sufficiently large at low frequencies that it can dominate over the intrinsic SQUID noise. Thus, it is common to operate the SQUID in a lock-in mode, at some suitable frequency where the amplifier noise is negligible. Practically, this is done by modulating the flux read out by the SQUID at some frequency f_m (usually via the same coil used for feedback),

[1]This rule works well for low-T_c SQUIDs. The higher operating temperature of high-T_c SQUIDs introduces noise which reduces the transfer coefficient V_Φ [5].

and demodulating the voltage response after amplification with a mixer. In this way, the range of frequencies in which the SQUID can be read out can be extended down to dc. Unfortunately, this modulation scheme also limits the bandwidth of the system; the largest signal frequency is at most $f_m/2$ [3].[2]

A schematic of the flux-locked loop used in this thesis is shown in Fig. 2.2. The voltage is amplified by a transformer followed by a gain stage. The oscillator applies a small ($\Phi_{ac} \lesssim \Phi_o/2$) ac flux to the SQUID at a frequency of $f_m = 100$kHz via the modulation/feedback coil. If the SQUID is operated at a minimum or a maximum of the V-Φ curve, its voltage response to the ac flux is at twice the modulation frequency, $2f_m$ [see Fig. 2.3(a)]. The output at the mixer in this case is zero. Away from this minimum, the modulated voltage response contains some component at frequency f_m, and the mixer response is nonzero [Fig. 2.3(b)].

When the feedback switch is closed, the SQUID is locked at the nearest stable point, a minimum in the V-Φ curve. Any signal flux away from this point is converted into a voltage from the mixer, which is low-pass filtered by an integrator and fed back through a resistance R_f to the modulation/feedback coil to null out the response. The voltage across R_f, the so-called "feedback resistor", is read out, and is proportional to the signal flux. Note that the SQUID never detects the absolute flux, only the difference in flux from the time the flux-locked loop is closed.

2.2.3 SQUID noise

There are several sources of intrinsic noise in SQUIDs. Nyquist noise currents across the Josephson junction resistances produce a white voltage noise across the SQUID and a white current noise around the SQUID loop [3]. Each noise source translates into a white flux noise via the flux-to-voltage transfer function V_Φ and the SQUID inductance L, respectively. A typical high-T_c SQUID has an intrinsic white flux noise of order $10\mu\Phi_o/\sqrt{Hz}$.

At low frequencies, fluctuations in the critical currents I_c of the Josephson junctions produce $1/f$ flux noise in the SQUID. The fluctuations across the two junctions may be symmetric (or in-phase) or antisymmetric (out-of-phase), and couple differently to the SQUID. Fortunately, readout schemes can eliminate both sources of noise. Fluctuations

[2] In some applications where the signals occur at high frequencies (for instance, NMR), a large bandwidth is important whereas low-frequency noise is immaterial. The SQUID is operated in a so-called "direct read-out" scheme, with no modulation.

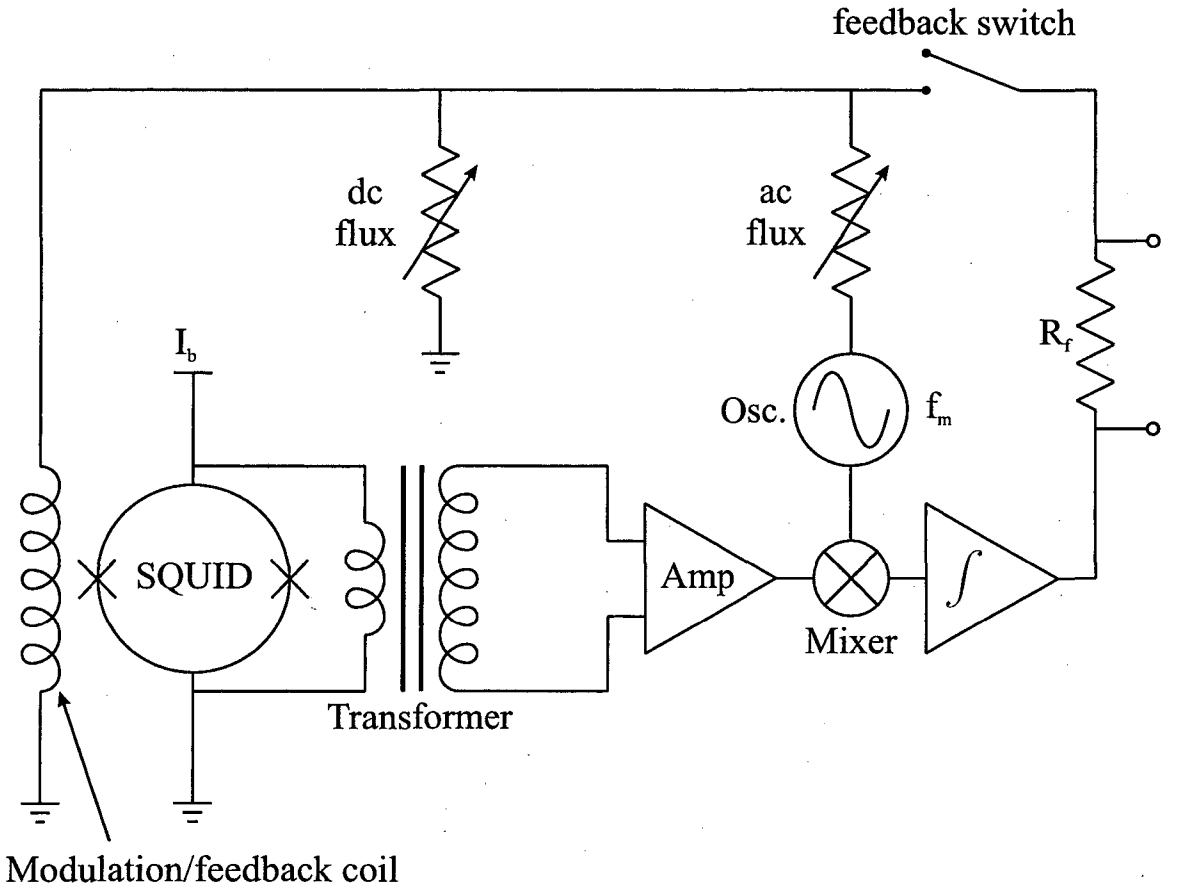

Figure 2.2: The flux-locked loop. The oscillator generates a 100kHz ac flux through the SQUID via the modulation coil. The resulting 100kHz voltage response from the SQUID is amplified by a transformer and a variable-gain solid-state amplifier, demodulated by the mixer, and low-pass filtered by the integrator. When the feedback switch is closed, the feedback coil applies a dc (quasistatic) flux to cancel out the signal flux from the sample. The feedback current is read out by measuring the voltage across the resistor R_f.

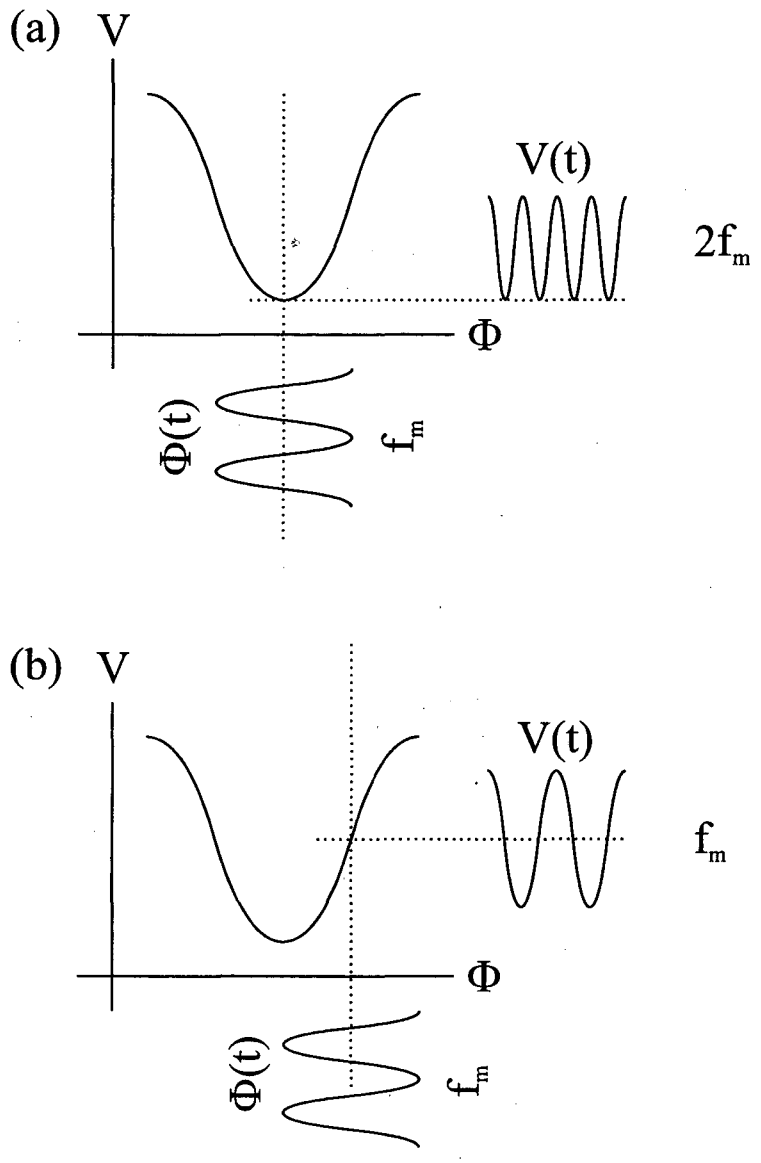

Figure 2.3: Flux modulation. If the SQUID is operated at a minimum in the V-Φ curve (a), its response to a small ac flux at a frequency f_m is at twice that frequency, $2f_m$, and the mixer outputs zero voltage. On the other hand, if the operating point is away from the minimum (b), there is a component at f_m, and the mixer outputs a voltage.

that are in phase at the two junctions give rise to a fluctuating voltage across the SQUID. The flux modulation scheme described above eliminates this type of noise provided the fluctuations occur at a frequency $\ll f_m$. This is because the net effect of the fluctuations is to shift the V-Φ curve in Fig. 2.3 vertically, leaving the voltage response at f_m unaffected. Fluctuations that are out-of-phase give rise to a net fluctuating flux $\delta\Phi$ around the SQUID loop. Here the V-Φ curve is shifted horizontally, and cannot be eliminated by the standard modulation scheme described above.

In a scheme called bias reversal, the bias current I_b is periodically reversed at a frequency commensurate with f_m (typically 100kHz/32 = 3.125kHz), reversing the polarity of the V-Φ curve and the sign of the fluctuating flux $\delta\Phi$. Simultaneously with the bias current reversal, a flux $\Phi_o/2$ is applied so that the sign of the flux-to-voltage transfer coefficient V_Φ at the working point remains the same. In this way, the voltage response averages out the flux fluctuations, provided they occur at frequencies much smaller than the bias reversal frequency. Figure 2.4 displays a measured SQUID flux noise spectrum. At high frequencies, the noise is white; $1/f$ noise below 50Hz contributes significantly in the top trace. In the bottom trace, bias reversal is implemented, reducing the $1/f$ noise below the white noise level over the measured frequency range.

Another intrinsic source of noise is the motion of flux in the superconducting film. Defects in the film act as trapping sites for flux vortices; thermally activated hopping from one site to another can lead to telegraph noise, which has a Lorentzian noise spectrum. A distribution of vortices with different hopping rates can often generate $1/f$ noise. This type of noise is often the result of operating the SQUID in a large external field (for instance, the geomagnetic field). Thus, it is common to operate SQUIDs in magnetically shielded environments to circumvent this problem, although significant work is being done to use SQUIDs unshielded.

2.3 SQUID design

The dc SQUIDs used in this thesis are fabricated from a thin film of the high-transition temperature superconductor $YBa_2Cu_3O_{7-\delta}$ (YBCO). A 160nm-thick film of this material is laser-ablated onto a (100) strontium titanate ($SrTiO_3$, or STO) bicrystal substrate [8]. STO provides a good lattice match to YBCO, allowing epitaxial growth. The bicrystal consists of two crystals with their crystallographic axes tilted with respect to each

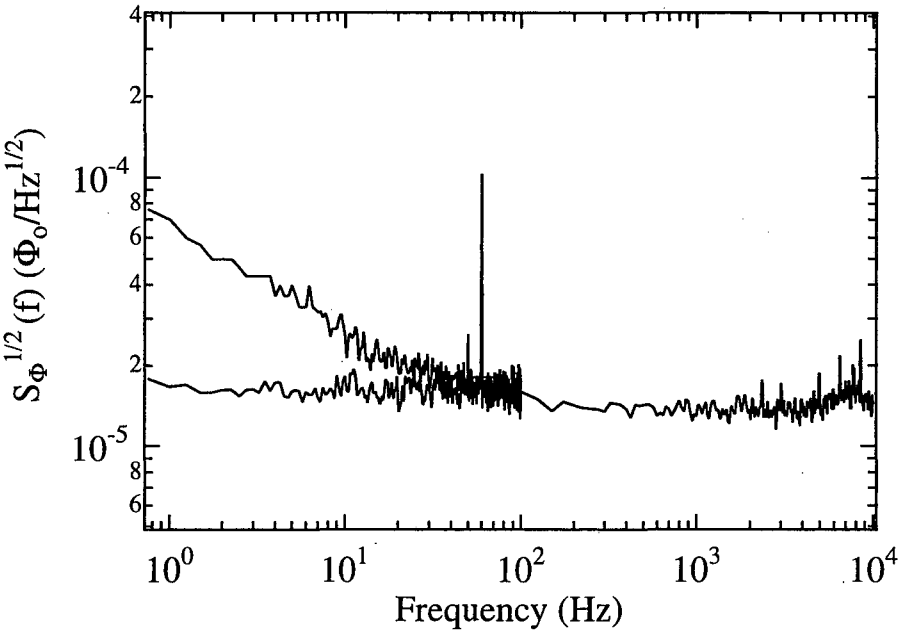

Figure 2.4: Typical SQUID noise spectrum, operated in a flux-locked loop at a modulation frequency of 100kHz. At high frequencies (1kHz) the noise is white; $S_\Phi^{1/2}$(1kHz) $= 14\mu\Phi_o/\sqrt{Hz}$. At low frequencies (1Hz) $1/f$ noise due to antisymmetric critical current fluctuations dominates; $S_\Phi^{1/2}$(1Hz)$= 70\mu\Phi_o/\sqrt{Hz}$ (top trace). Using a bias reversal scheme, this noise contribution can be reduced to the white noise level (bottom trace). Due to the flux modulation scheme, the bandwidth is limited to about 10kHz. The peak in the spectrum is the ubiquitous 60Hz line noise. (The SQUID is "slit A-C" in Fig. 2.5 and Table 2.1.)

other (usually by 24° or 30°) fused together. The grain boundary between the two crystals makes a weak link in the superconducting film. Josephson junctions are formed by patterning 1-2μm-wide microbridges into the YBCO across the grain boundary of the bicrystal. The patterning is achieved by conventional photolithography and Ar-ion milling.

Figures 2.5(a)-(c) and Table 2.1 display the designs and characteristics of the three "washer"-type SQUIDs used in this thesis. The dotted line shows the location of the grain boundary; the Josephson junctions are located where the dotted line crosses the microbridges in the superconducting film. Note that the washer in Fig. 2.5(b) crosses the grain boundary, but does not act like a Josephson junction since its critical current is much larger than that of the microbridges. The effective area A_{eff} in Table 2.1 is the ratio of the flux measured in response to a uniform applied field. It is a measure of the sensing area of the SQUID. For the hole L2-type SQUID, this has a simple geometric interpretation: the measured effective area corresponds to a square loop of side $40\mu m$, exactly passing though the middle of the washer film. For the two slit SQUIDs, a geometrical interpretation is more difficult. Generally, A_{eff} is approximately equal to the geometric mean of the washer and slit areas. In Appendix A, where I model the SQUID response to various magnetic sources, I treat the SQUID as a square loop of side $\ell_{eff} = (A_{eff})^{1/2}$.

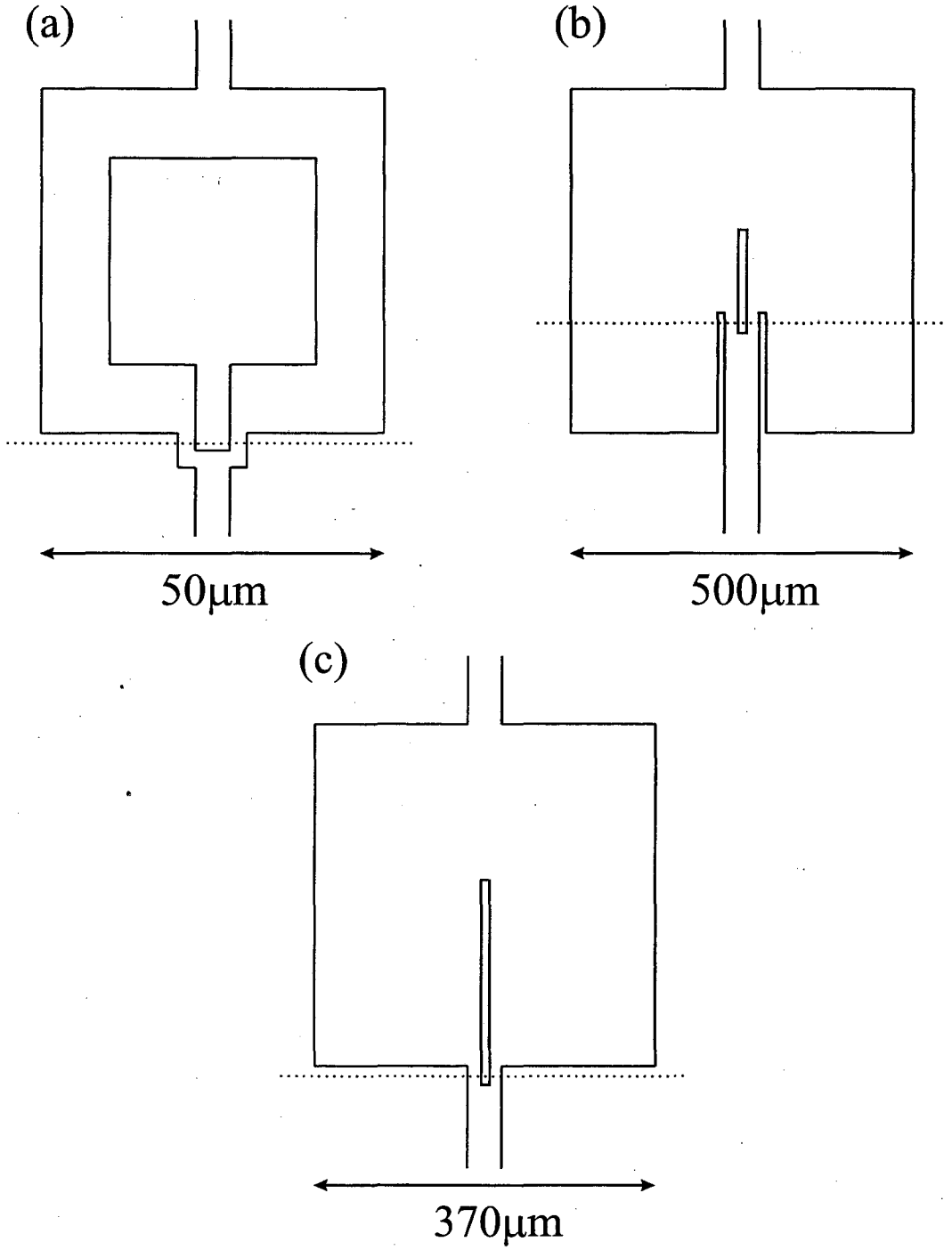

Figure 2.5: Designs of SQUIDs used in this thesis. SQUID type (a) "hole L2" with an outer dimension of $50\mu m$ and a $30\mu m$ hole, (b) "slit A-C" with an outer dimension of $500\mu m$ and a slit of length $100\mu m$ and width $4\mu m$, and (c) "slit A-A" with an outer dimension of $370\mu m$ and a slit of length $180\mu m$ and width $4\mu m$.

SQUID type	A_{eff} (mm^2)	A_{eff}^{-1} $(\mu T/\Phi_o)$	ℓ_{eff} (μm)	L (pH)	R_n (Ω)	I_c (μA)	ΔV (μV)	$S_\Phi^{1/2}$(1kHz) $(\mu\Phi_o/\sqrt{Hz})$
hole L2	0.0016	1.30	40	57	1.2	110	9	33
slit A-C	0.0129	0.155	114	40	1.8	100	11	25
slit A-A	0.0163	0.123	128	60	4.0	24	22	14

Table 2.1: Representative parameters of SQUIDs used in this thesis. A_{eff} is the measured effective sensing area, which can be expressed as a conversion factor A_{eff}^{-1} between field and flux; $\ell_{eff} \equiv (A_{eff})^{1/2}$. L is the calculated SQUID inductance, R_n the measured normal resistance, I_c the measured critical current, and ΔV the peak-to-peak voltage modulation. $S_\Phi^{1/2}$ is the SQUID flux noise level at 1kHz.

Chapter 3

High-T_c SQUID Microscope for Room Temperature Samples

3.1 Introduction

The extreme sensitivity of Superconducting QUantum Interference Devices to weak magnetic fields has led to a variety of applications. Soon after their invention, scientists realized that they could be used to make magnetic images of samples. As early as 1964, Zimmerman and Mercereau [9] used a SQUID to image individual flux vortices in a superconducting wire. In early measurements, images were one-dimensional scans; systems subsequently developed in the late 80's [10, 11] could raster-scan samples in two dimensions. The so-called scanning SQUID microscope (SSM) has since become a powerful tool, used in a variety of fields to make magnetic images.

SQUID microscopes can be classified according to the temperature of the sensor and that of the sample. Generally speaking, these devices come in two classes, "cold sample" microscopes, where the sample is at the same temperature as the SQUID, and "warm sample" microscopes, where the sample is at room temperature. Furthermore, they can be high-T_c or low-T_c microscopes depending on the type of SQUID. Cold sample microscopes have generally been applied to the study of superconducting materials; for example, in measurements of vortex structure and dynamics [10], and of the pairing symmetry of the superconducting state in high-T_c materials [11]. Warm sample microscopes are predominantly used for non-destructive evaluation (NDE); for instance, in imaging of currents in

printed or integrated circuits [12], of the remanent magnetization of magnetic materials, or of Johnson noise in metals [13]. They are also increasingly used for biomagnetism, in imaging currents in biological tissue such as the heart and nerve cells [14].

SSM's compete with other magnetic imaging techniques. Many are similar in concept but use different magnetic sensors to detect the sample magnetic field. Scanning microscopes may use Hall bars, magnetoresistive elements, induction loops, or magnetic cantilevers (as in magnetic force microscopy) as sensors. Other techniques, such as magneto-optical imaging, scanning electron microscopy with polarization (SEMPA), electron holography, and decoration techniques, are fundamentally different in approach. Each method has its advantages and disadvantages. A complete discussion of each technique is outside the scope of this thesis; we suggest the reader refer to Kirtley and Wikswo [15] for an excellent overview. Generally speaking, scanning SQUID microscopes have a higher magnetic field sensitivity but a worse spatial resolution—by which I mean the smallest distance between two magnetic sources that can be resolved.

A figure of merit for SSM's is the minimum sensor-to-sample separation z_o. The spatial resolution of a scanning SQUID microscope is limited by the larger of two dimensions: the separation z_o, and the outer dimension of the SQUID. More importantly, the fields from the sources that are scanned are often sharply dependent on this parameter (for instance, a dipole source generates a field that falls off as $1/z_o^3$). As a result, it is advantageous to keep z_o to a minimum. In cold sample microscopes, the SQUID can be brought into physical contact with the sample, allowing separations as small as a few micrometers to be achieved. In order to image samples maintained at room temperature and atmospheric pressure, warm sample microscopes must thermally isolate the SQUID from the sample, leading to larger separations.

The main requirement of the warm sample microscope is to maintain the SQUID below its critical temperature while keeping it as close as possible to a sample at room temperature. The general approach is to place the SQUID inside a vacuum enclosure on the end of a "cold finger" (made of a good thermal conductor like sapphire or copper) thermally anchored to a reservoir which maintains it at the desired temperature. The reservoir may be a container filled with cryogen (liquid helium or nitrogen) or a cryo-cooler. In this way, the cold finger can be placed close to a room temperature sample but thermally isolated from it. This is generally much easier to implement in microscopes equipped with high-T_c SQUIDs rather than low T_c SQUIDs, due to their higher operating temperature. High-T_c SQUID

microscopes can usually achieve smaller separations than their low-T_c counterparts[1]. An important milestone in the development of these devices was the construction by Black *et al.* [16] of a high-T_c SQUID microscope with a minimum $40\mu m$ SQUID-to-sample distance. In the next section I will describe in detail a high-T_c warm-sample SQUID microscope [4, 17, 18] which achieves a separation as small as $15\mu m$.

3.2 Design and performance

3.2.1 Dewar

The layout of the SQUID microscope dewar is shown in detail in Fig. 3.1(a) & (b). The vacuum enclosure P is made of a G-10 fiberglass cylinder and circular top and bottom plates which are sealed together with viton o-rings. The enclosure can be connected to a vacuum pump and evacuated through the pump-out valve Q. The liquid nitrogen reservoir J, made of brass, is connected to the top plate of the vacuum enclosure by three fiberglass support screws O. Two stainless steel nitrogen fill tubes N (one inlet, one outlet) are hard-soldered to the brass can at one end and epoxied (Stycast 2850FT, Emerson & Cuming, Inc.) to the fiberglass top plate at the other. The brass can can hold up to $1L$ of liquid N_2. A 30Ω cartridge heater M and a platinum thermometer are attached to the bottom of the can in order to heat it and monitor its temperature. A charcoal panel L which absorbs residual gas is also attached to the bottom side of the reservoir. An OHFC copper rod K runs through the center of the brass can and provides a good thermal link between the liquid nitrogen and the copper base I, to which is clamped the sapphire cold finger H. The cold finger consists of two sapphire rods connected end to end with another copper clamp. Silver foil is placed between the two copper clamps and the sapphire rods to ensure good thermal contact at the interfaces.

The microscope is sealed at the top by a removable vacuum window assembly A. Figure 3.1(c) shows a detailed view. The assembly consists of a vacuum window c, which will be described in the following section, epoxied to a quartz tube d of length $15mm$, OD $15mm$, and ID $13mm$, which is glued to an acrylic ring e. The assembly is screwed on top of a fiberglass basepiece B, through the acrylic ring, and is sealed on its outer circumference

[1]The predominant heat load on the SQUID in the microscope is from blackbody radiation at room temperature. While the loads for low- and high-T_c SQUIDs are approximately equal, the boil-off rate for liquid helium is much more significant than for liquid nitrogen. Generally, this requires placing a radiation shield between the low-T_c SQUID and the sample, increasing the separation.

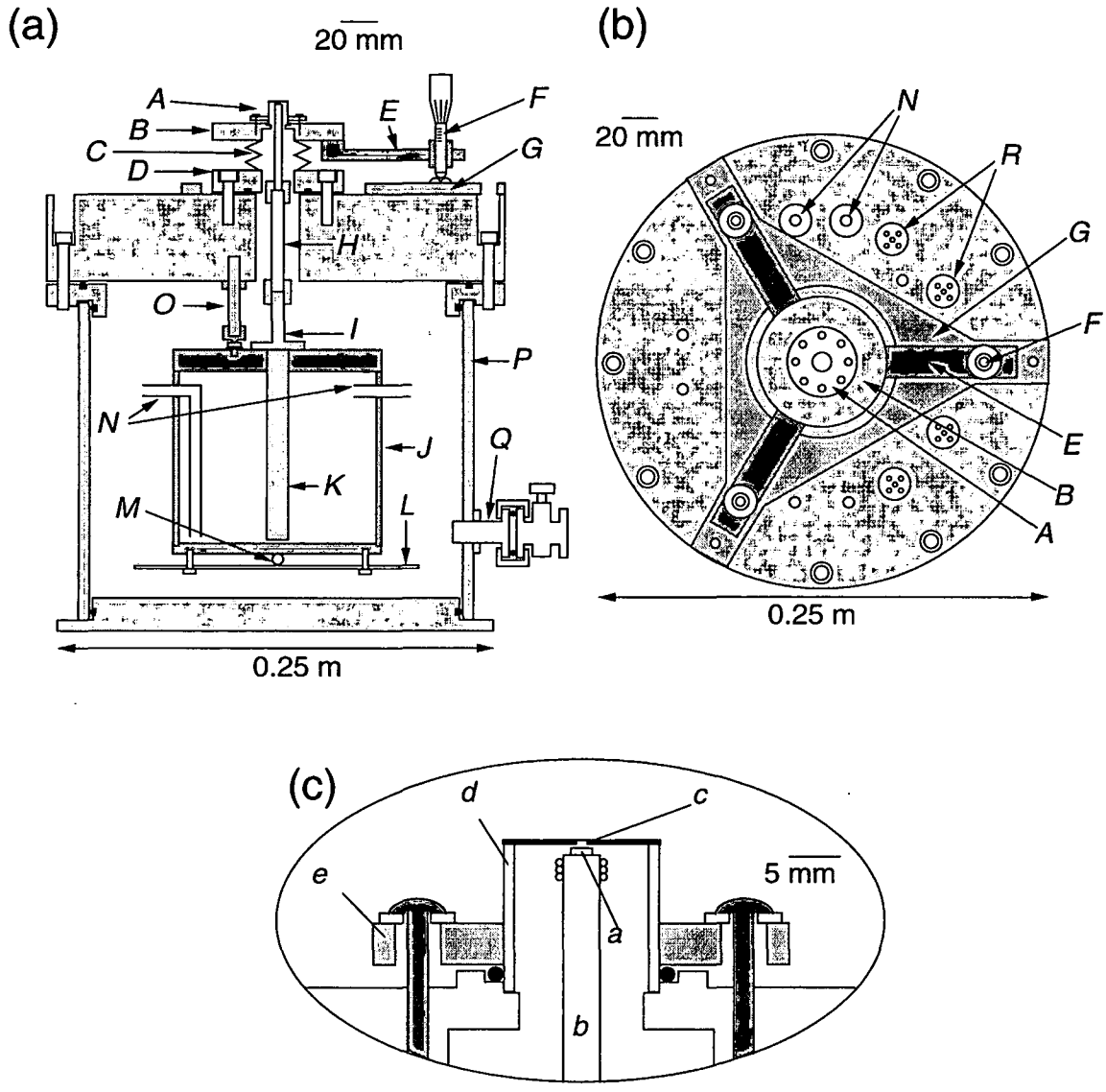

Figure 3.1: The SQUID microscope; (a) section, (b) top view, and (c) blow-up of window assembly. *A* Vacuum window assembly, *B* upper fiberglass disk, *C* brass bellows, *D* lower fiberglass disk, *E* brass arm, *F* positioning micrometer, *G* phenolic baseplate, *H* sapphire cold finger, *I* copper base, *J* liquid nitrogen can, *K* OFHC copper rod, *L* charcoal panel, *M* cartridge heater, *N* nitrogen fill tubes, *O* fiberglass support rod, *P* vacuum enclosure, *Q* pump-out valve. Detailed view of window assembly (c): *a* SQUID chip, *b* cold finger, *c* vacuum window, *d* quartz tube, *e* acrylic ring.

by an o-ring. In order to allow the vacuum window to be moved vertically and laterally without breaking vacuum, the fiberglass basepiece is epoxied to a flexible brass bellows C which is glued to a second fiberglass disk D at the bottom. This piece is mated to the top plate of the vacuum enclosure, and sealed to it with an o-ring. Long brass arms E connect the upper fiberglass disk to three micrometers F (Newport Corp.) which fit onto a kinetic mount on a triangular phenolic basepiece G. The kinetic mount can be moved laterally, moving the upper fiberglass disk and the vacuum window assembly with respect to the sapphire rod. In this way, the vacuum window can be aligned to a SQUID. The micrometers can move the vacuum window up and down or tilt it with respect to the cold finger.

3.2.2 Magnetic noise considerations

Because of the extraordinary sensitivity of Superconducting QUantum Interference Devices, special care must be taken to minimize environmental sources of magnetic noise. The large static field from the earth (and other environmental sources, such as steel beams in the floor, or gas cylinders) can cause flux vortices to trap in the superconducting film and generate noise as they move around. Line noise at 60Hz and its harmonics can contribute magnetic noise as large as $10nT/\sqrt{Hz}$, about three orders of magnitude larger than the intrinsic noise of the SQUIDs in the microscope (see Table 2.1). Radiofrequency (rf) noise from computer monitors and other electronic equipment is known to reduce the flux-to-voltage transfer function ΔV of a SQUID. As a result, we operate the SQUID microscope inside a cylindrical μ-metal shield[2] (Amuneal Manufacturing Corp.). The shield consists of three layers of $1mm$-thick μ-metal, and completely encloses the SQUID microscope; a removable lid allows access through the top of the enclosure. Static fields are reduced by a factor of 13,000, 60Hz fields by 52,000. We did not observe any adverse effects from rf fields on the SQUID [17].

It is also necessary to minimize magnetic noise sources from the SQUID microscope itself. Where possible, the microscope was designed avoiding magnetic materials and metals (which generate Nyquist noise currents). The stainless steel nitrogen fill tubes N and positioning micrometers F are permanently magnetic, and the machined G-10 fiberglass, copper, and brass may contain low levels of magnetic impurities. However, we found no

[2] μ-metal is an alloy with a very high permeability μ, causing field lines to permeate through it, shielding the cavity contained by the shield (for example, see Jackson [19]).

evidence that these generated noise in excess of the intrinsic noise of the SQUID. Tom Lee estimated the Nyquist noise contributions from selected metallic components—the brass bellows C, the brass arms E, the copper clamp I, the brass can J, and the μ-metal shield—and found that they generate noise over an order of magnitude smaller than the intrinsic SQUID noise [17]. By far, the greatest contributors were the brass arms, generating about $60fT/\sqrt{Hz}$ field noise. However, while the noise contributions from magnetic materials and metals in the SQUID microscope seem negligible, there is good evidence that their response to an applied magnetic field pulse can be detected by the SQUID. As will be discussed in Section 7.2.3, relaxation of magnetic domains in magnetic materials and of eddy currents in metals in response to a field pulse can generate a decaying flux that can be observed.

3.2.3 Thermal load on dewar

The vacuum dewar is customarily pumped out to a pressure of $P \approx 10^{-5}\,Torr$ with a diffusion pump. Special care must be taken to ensure that no vacuum leaks are present in the microscope; for example, all machined fiberglass surfaces were covered with a layer of epoxy (Stycast 1266, Emerson & Cuming, Inc.) to eliminate leaks. At pressures below $1mTorr$, the mean free path of the residual gas is much larger than any distance which separates room temperature from liquid nitrogen temperature inside the dewar. One consequence is that the heat load from residual gas depends only on the temperature difference, not on the separation between the two. Furthermore, those heat leaks are negligibly small. There is a contribution from conduction along the support rods O and nitrogen fill tubes N estimated at $0.4W$.

By far, the biggest heat load on the microscope is from blackbody radiation. Using the Stefan-Boltzmann law

$$Q_\ell = \epsilon\sigma A(T_o^4 - T_i^4). \tag{3.1}$$

we can estimate the heat loads on various parts of the dewar. ϵ is the emissivity of the material under consideration, σ the Stefan-Boltzmann constant, A the surface area, and $T_o = 300K$ the outer temperature, $T_i = 77K$ the inner temperature. The brass can, with $\epsilon \approx 1$ and a large surface area, has the largest heat load, $\sim 20W$, corresponding to a liquid N_2 boil-off of $0.4L/hr$, which is unreasonably large[3]. By comparison, the sapphire cold

[3]The latent heat of liquid N_2 is $160J/mL$.

finger has an emissivity of 0.2, a smaller area, and a load of only $0.2W$. By wrapping layers of aluminized mylar insulation around the various dewar components, one reduces the respective heat loads by a factor of

$$\eta = \frac{1}{1 + n/\epsilon_s}, \tag{3.2}$$

where n is the number of layers and $\epsilon_s = 0.044$ is the emissivity of the aluminized mylar. As a result, we wrap the brass can J, fill tubes N, support rods O, copper clamp I and sapphire cold finger H with 10-15 layers of aluminized mylar. In this way, the total blackbody radiation load should be reduced to $\sim 0.1W$. We measure a liquid nitrogen hold time of 29 hours, which corresponds to a heat load of $1.5W$, significantly larger than the estimated value of $0.5W$. The shielding factor η from the aluminized mylar insulation is probably overestimated.

3.2.4 Vacuum window

In the above section, we argued that the major thermal load on the SQUID in the microscope is from blackbody radiation, not conduction, so that the load is independent of the SQUID-to-sample separation z_o. Thus, what limits z_o is not temperature considerations but how close the SQUID can be placed to the vacuum window and the thickness of the window itself.

In the initial configuration of the microscope, a $75\mu m$-thick sapphire disk was used as a vacuum window. There, the minimum separation z_o was predominantly limited by the window thickness ($z_o \approx 140\mu m$) [4]. Subsequently, Tom Lee developed a vacuum window made out of a thin membrane of silicon nitride (Si_xN_y) [17, 18]. SiN has a large elastic modulus, allowing a membrane as thin as $3\mu m$ to withstand a 1 atmosphere pressure differential. This window technology allows a much smaller separation z_o; as a result, all subsequent experiments with the microscope have used SiN windows. Among its many convenient properties, SiN is optically transparent (allowing visual access to the SQUID for alignment) and electrically insulating. It is also easily micromachined to desired specifications. Vacuum windows are constructed using conventional photolithographic and microfabrication techniques discussed below and illustrated in Fig. 3.2(a)-(d).

A $3\mu m$-thick layer of SiN is deposited onto both sides of a $500\mu m$-thick 4" silicon wafer by low-pressure chemical vapor deposition (LPCVD) [Fig. 3.2(a)]. A $1.184mm \times 1.184mm$ window is photolithographically defined on one side of the Si wafer [Fig. 3.2(b)],

so that the exposed SiN can be removed by SF_6 plasma etching [Fig. 3.2(c)]. The entire wafer is then placed in a concentrated KOH bath. Potassium hydroxide selectively etches Si, but not SiN. Consequently, the KOH etches anisotropically at an angle of 54.7° through the Si in the defined window until it reaches the SiN on the other side. The final result is a free-standing, $440\mu m \times 440\mu m$ square, $3\mu m$-thick SiN membrane surrounded by a Si pyramidal "well" providing structural support [Fig. 3.2(d)].

An entire 4" Si wafer may accommodate 24 windows defined with a wafer stepper. The wafer is diced into $15.5mm \times 15.5mm$ square Si pieces each containing a "well", and each is glued (Stycast 1266, Emerson & Cuming, Inc.) to a cylindrical quartz tube [d in Fig. 3.1(c)]. The squares may be glued to the tube "well side up" or "well side down" depending on the experiment and SQUID. In the former, the well can be used as a liquid sample cell; in the later, the well is on the vacuum side so that samples can be scanned flush with the window. The Si/SiN/quartz tube assembly fits on the end of the microscope head piece, sealed on the outer perimeter by an o-ring. The assembly is removable.

3.2.5 SQUID configuration

With the $3\mu m$ SiN vacuum window described above, we have achieved SQUID-to-sample separations as small as $15\mu m$ [18]. Clearly, the minimum separation is limited by the vacuum gap between the top surface of the SQUID and the bottom surface of the window, not by the thickness of the window. This gap is in large part determined by the angular misalignment between the plane of the SQUID and that of the window. For instance, a height differential of $15\mu m$ across the SiN window corresponds only a to tilt of 2°. There are two approaches to this problem, one to devise ways of measuring and reducing the angular misalignment, and the other to minimize the SQUID chip dimensions so that a given tilt translates into a smaller height differential.

Alignment of the SQUID chip and the window planes is achieved in several steps. First, the top surface of the cold finger is aligned to the top fiberglass basepiece on which the window/quartz tube assembly is mounted. As described in [17], a glass slide is placed on the end of the cold finger and its tilt with respect to the basepiece determined by measuring the vertical distances between both ends of the slide and the basepiece. Using the three positioning micrometers, the two surfaces can be aligned to within 1°. Unfortunately, the SQUID chip, once mounted, may not be perfectly level with the surface of the cold

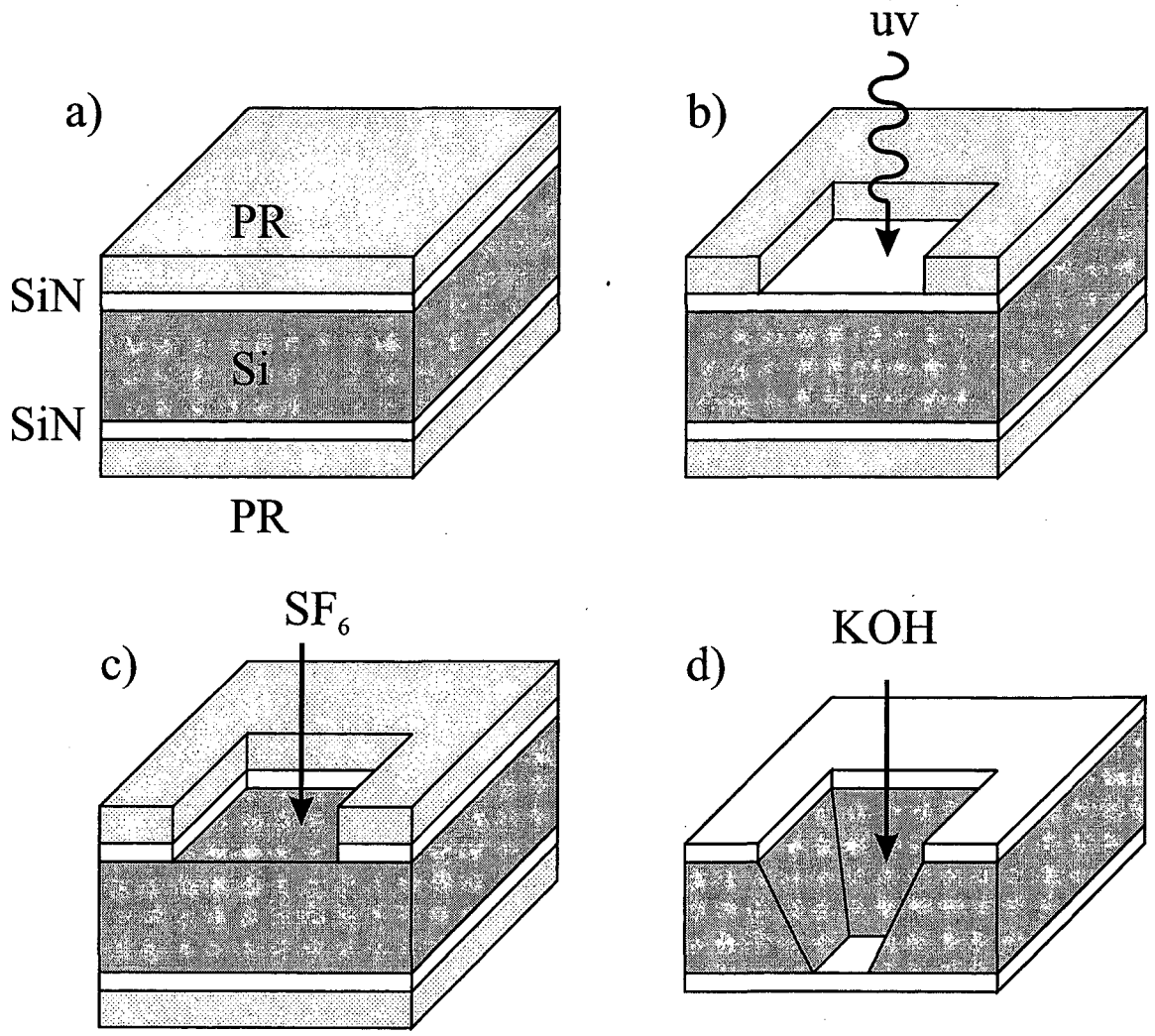

Figure 3.2: Microfabrication of silicon nitride vacuum windows (section, not to scale). (a) SiN is deposited on both sides of a Si wafer by LPCVD. Photoresist (PR) is spun on both sides, and (b) photolithographically patterned to make windows. The exposed SiN is plasma-etched (c) with SF_6. The exposed Si is etched in a bath of concentrated KOH (d), leaving a "well" with an unsupported SiN window at the bottom.

finger. Often, it is necessary to do a second alignment by measuring vertical distances between the SQUID and the SiN window at four points on the chip (only three are needed to define the plane, the fourth is for redundancy). A 10X microscope objective is used to measure the distance between the two planes, with a precision of $\pm 5\mu m$. Again, the angular misalignment can be reduced to $\lesssim 1°$.

To minimize the height differential due to misalignment, we try to keep the SQUID chip dimensions down to 1-3mm wherever possible. If the silicon well of the microscope faces outside, we can achieve SQUID-to-window separations as small as 30-35μm for those dimensions. For smaller separations, smaller SQUID chips are needed. In particular, if the microscope is operated well side down, then the SQUID chip must be smaller than the $440\mu m \times 440\mu m$ window area. Dicing chips to this size is technically difficult. It appears that cutting through the 500μm-thick STO substrate with a dicing saw puts stress on the grain boundary, damaging the Josephson junctions, leading to a degradation in SQUID properties[4]. A gentler cutting procedure was devised by Tom Lee in which cuts are made progressively to a final depth of 150μm [see Fig. 3.3(a) & (b)]. Then, the substrate is polished from the back side to a final thickness of 150μm, releasing individual SQUID chips of the desired size [Fig. 3.3(c)]. For the polishing, the substrate is flipped over and wax-mounted onto a polishing block. Initially, we used a motorized polishing machine with diamond grit polishing fluid. Subsequently, I polished by hand on a dry surface with carbide and diamond grit paper, progressively going down in grit size. I placed 150μm-thick Si spacers on the polishing block to ensure that the polishing is parallel to the surface of the substrate.

Once a SQUID has been diced to the desired size, it can be mounted onto the cold finger and leads can be attached to its contact pads. Clearly, it is undesirable to have leads making contact to the SQUID on the top surface of the chip, since they would take up space and increase the vacuum gap further. Instead, we extend the silver contact pads of the SQUID over the edge of the chip and attach the leads to the edges. This is done by evaporating 200nm-thick strips of silver at 45° to the surface [Fig. 3.3(e)]. The strips are defined by a shadow mask, usually made of mylar or aluminum foil sheet cut by hand with a razor blade to the required dimensions. To ensure electrical continuity over the edge of chip, I often bevel or "dull" an edge by polishing it with fine diamond grit paper at a 45°

[4]For larger SQUID chips, this is not a problem since the cuts are much further away from the junction area.

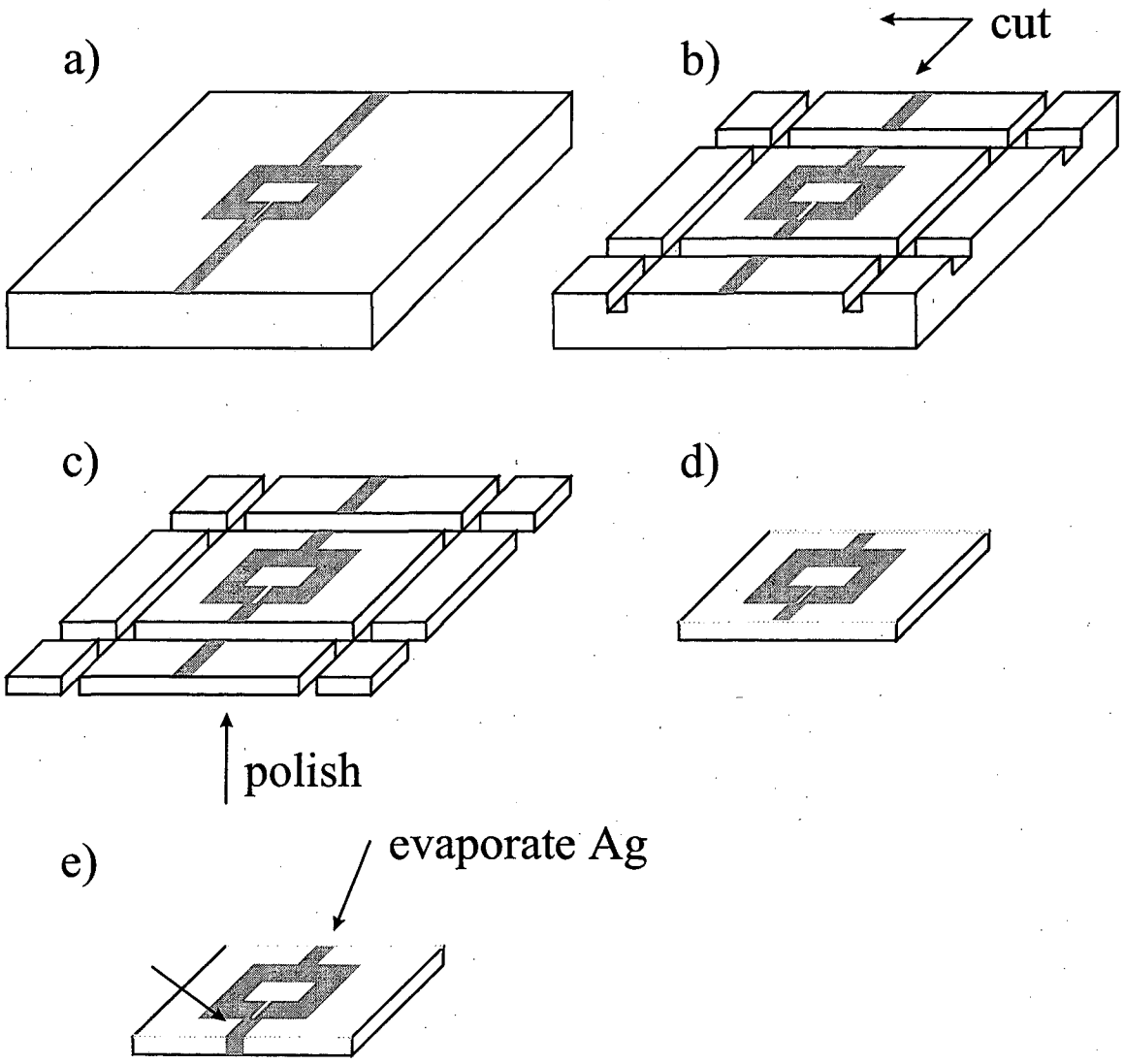

Figure 3.3: Preparation of small-area SQUID chip (section, not to scale). A $500\mu m$-thick substrate with a SQUID (a), is cut with a diamond grit blade to a depth of $150\mu m$ (b). The back side is polished down to that thickness (c). The edges of the resulting SQUID chip (d) are beveled, and silver contact pad extensions are evaporated at 45° over the edges (e).

angle [Fig. 3.3(d)]. The leads make electrical contact to these extended pads with silver paste (Cat. No. 4929N, Dupont).

With the SQUID and SiN window prepared in the manner described above, it is possible to achieve separations as small as $15\mu m$ for small SQUID chips ($\sim 400 \times 400\mu m$) and 30-35μm for larger chips ($\sim 2 \times 3mm$). The separation can be measured in a variety of ways. If the microscope is run in scanning mode, a wire through which a known current is passed can be scanned over the SQUID in a direction perpendicular to the current. The flux can be modeled and the scan fitted to determine z_o. The quality of the fit depends on the model; SQUIDs with large washers tend to distort the wire field in ways that are not easily quantifiable. However, where the fit is good, z_o is determined very accurately, within $\pm 2\mu m$. If the microscope is not run in scanning mode, other methods have to be used. We evaporated two $5\mu m$-thick aluminum wires on the SiN membrane, through which we can pass a known current. The wires are not scanned, but we have two flux measurements for the two unknowns: the separation z_o and a lateral offset. Again, this method is subject to error due to distortion effects by the washer. Furthermore, tilt in the SQUID chip introduces a third unknown which can affect the determination of z_o. The simplest and most reliable method is not magnetic but optical. As described above, a 10X objective can be used to measure the SQUID-to-window distance, by moving the focal plane of the objective vertically until the SQUID chip or window comes into focus. The distance can be measured in this way within $\pm 5\mu m$. A stronger objective would perhaps yield a smaller error.

3.3 Optimal coupling conditions

3.3.1 Point dipole source

So far in our discussion we have focused on minimizing the SQUID-to-sample separation, arguing that the sample field increases with decreasing distance. For example, the field from a dipole source falls off as $1/z^3$, where z is the separation. However, the dimensions of the SQUID are also important. As we will see, it is necessary to optimize the SQUID parameters to maximize the sensitivity of the microscope.

We can illustrate this point by treating the SQUID as a circular loop of radius a. It is straightforward to calculate the flux through this loop from a point dipole of moment

m, a distance z away, centered on the loop axis [see Fig. 3.4(a)]:

$$\Phi = \frac{\mu_o m}{2} \frac{a^2}{(a^2 + z^2)^{3/2}}. \tag{3.3}$$

The flux monotonically increases as z is decreased, until it saturates for $z \lesssim a$. For distances much greater than the loop size, the flux approaches the expected $1/z^3$ dependence [see Fig. 3.4(b)]. Generally, it is always advantageous to place the loop as close as possible to the dipole. The flux's dependence on the loop radius a, however, is not monotonic. Rather, for a given separation z there is an optimal loop radius $a_{opt} = \sqrt{2}z$. Intuitively we may understand this as follows: as the loop size approaches zero, less flux is coupled [Fig. 3.4(c)]; as the loop size becomes infinite, as many field lines from the dipole go into the loop as out of the loop, canceling the flux [Fig. 3.4(d)]. Between these two limits, there is a region of optimal coupling.

This simple calculation, while ignoring the exact details (the geometry of the SQUID, the flux focusing of the superconducting washer), captures the essence of the coupling issue in the SQUID microscope. To a first approximation, the exact geometry of the SQUID does not matter. A good rule of thumb for optimal coupling between a SQUID of effective area A_{eff} a distance z away from a point dipole is

$$\ell_{eff} \equiv (A_{eff})^{1/2} \approx 2.5z. \tag{3.4}$$

Substituting this into Eq. (3.3), one finds the flux Φ from a dipole of moment m a distance z away at optimal coupling conditions to be

$$\Phi\,[m\Phi_o] \approx 1.2\,\frac{m\,[10^{-17}A{\cdot}m^2]}{z\,[\mu m]} \tag{3.5}$$

where the brackets indicate the units. The choice of units for the dipole moment m is not arbitrary; it corresponds to the moment of one single-domain, 35-nm diameter magnetite (Fe_3O_4) nanocrystal. As we will see in the next chapter, the magnetic inclusions called magnetosomes present inside magnetotactic bacteria have a dipole moment of $\sim 10^{-17}A \cdot m^2$.[5] Equation (3.5) is a good rule of thumb for converting from dipole moment to flux[6]. Thus, a SQUID with $A_{eff} \approx 40\mu m \times 40\mu m = 0.0016mm^2$ [such as the "hole L2"-type SQUID in Fig. 2.5(a)] and flux noise $10\mu\Phi_o/\sqrt{Hz}$ a distance $z \approx 15\mu m$ away (representing optimal

[5]Note on units: the Bohr magneton $\mu_B \approx 9 \times 10^{-24}A \cdot m^2$.

[6]Although Eq. (3.5) was derived for a dipole moment oriented normal to the SQUID, it remains a good rule of thumb for dipoles parallel to the SQUID, laterally displaced for optimal coupling.

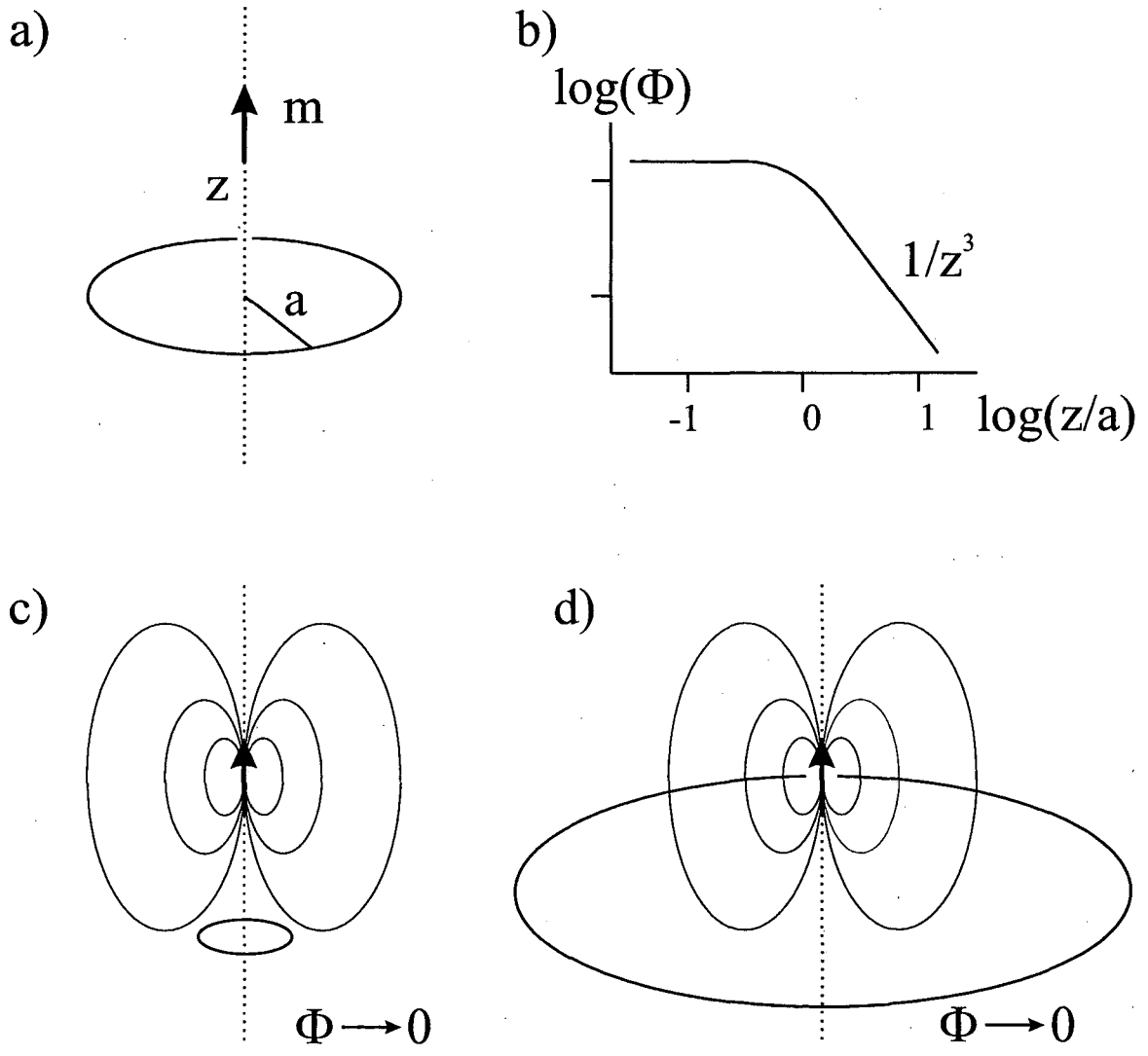

Figure 3.4: Coupling of a point dipole to a circular pickup loop. A dipole of moment m located a distance z from a circular loop of radius a (a) generates a flux (b, log-log plot) which falls as $1/z^3$ for $z \gg a$ and saturates for $z \lesssim a$. As $a \to 0$, the flux coupled goes to zero (c); as $a \to \infty$, the net flux goes to zero (d).

coupling) has a dipole moment noise of $8 \times 10^{-17} A \cdot m^2/\sqrt{Hz}$; in other words, such a SQUID can resolve the flux change due to a single 35-nm Fe_3O_4 nanoparticle with a signal-to-noise of 8 in a 1Hz bandwidth.

3.3.2 Extended sources

The situation is slightly more complicated for samples which have a nonzero size. Size effects come into play when the linear dimension of the sample is comparable to either $\ell_{eff} \equiv (A_{eff})^{1/2}$ or z. To illustrate this, consider a cube of side s and a uniform magnetic dipole density ρ_m. The net moment points normal to the SQUID and is centered about its axis as in Fig. 3.4(a).

Plotted in Fig. 3.5 is a three-dimensional graph of the flux as a function of the separation z and sample size s for a given, fixed SQUID dimension ℓ_{eff}. The first thing to notice is that the flux begins to saturate when $z \lesssim s$. Indeed, as the sample becomes infinitely big, the flux becomes independent of z since the field generated becomes spatially invariant. Another way to look at this is that the SQUID only detects the flux from a certain volume of space, determined by both z and ℓ_{eff}. If the sample is much larger than this volume, it does not couple efficiently to the SQUID, since a part of it goes undetected. Therefore, as before there is an optimal SQUID size which optimizes the flux. However, the condition here is that the effective loop size of the SQUID $\ell_{eff} \approx s$, provided that $z \lesssim s$.

The lesson to take away is that the SQUID geometry must be optimized for each particular sample. It is not a simple question of increasing the pickup area of the SQUID to improve its field sensitivity. The reason for this is that this type of argument breaks down in the near field limit where the field from the sample is not uniform across the pickup area of the SQUID. The crossover between far field and near field occurs where $z \lesssim \ell_{eff}$, precisely where the SQUID microscope is operated. These issues are discussed in more detail in Appendix A.

3.4 SQUID "microscope"?

Nowhere in the experiments that I will describe in the remainder of this thesis did we use the SQUID microscope's magnetic imaging capabilities. The microscope described can be equipped with a 2D scanning stage, to raster-scan samples in x and y over the SQUID. Details on its design and images obtained with it are found in the references

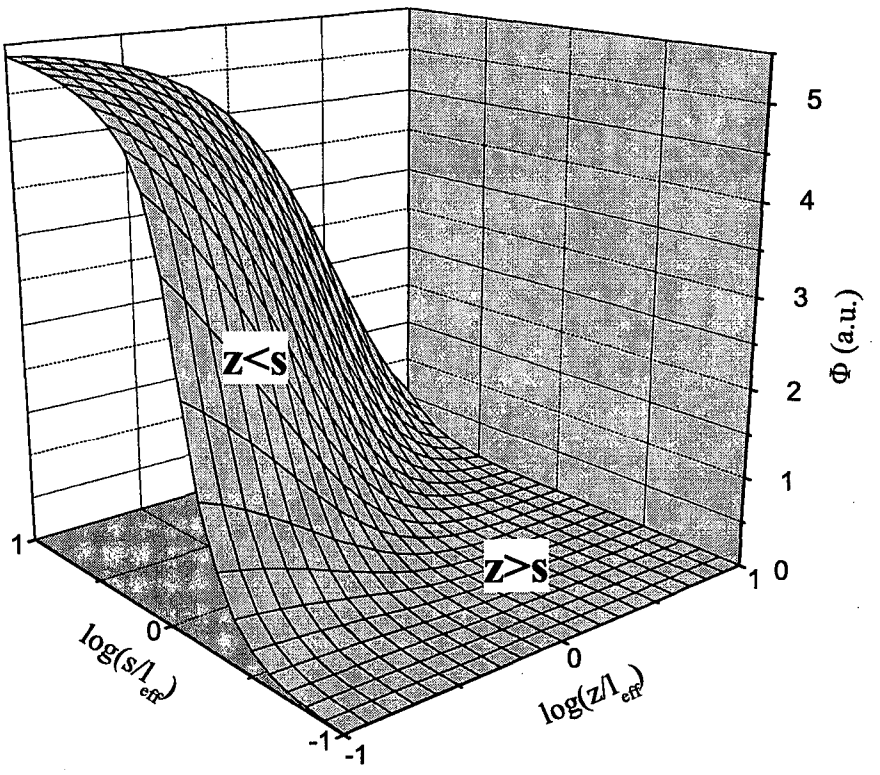

Figure 3.5: Flux due to a cube of side s with a uniform dipole moment density ρ_m as a function of separation z to the SQUID, and size s. The SQUID dimension ℓ_{eff} is fixed. The x and y axes are $\log(s/\ell_{eff})$ and $\log(z/\ell_{eff})$, respectively. The flux units are arbitrary.

[4, 17, 18]. I will describe, in Part I of this thesis, a study of magnetic microorganisms called magnetotactic bacteria with the SQUID microscope, and in Part II, the development of a magnetic immunoassay with the device. In both experiments, the samples remained stationary with respect to the SQUID. Rather than use the imaging capabilities of the microscope, we exploited its ability to position the extraordinarily sensitive SQUID very close to our biological samples. In this respect, this device was not precisely used as a "microscope". Several colleagues have objected to the use of the word. However, I will continue to use it for lack of a better expression, and, moreover, to remind the reader that the device can be used in such a fashion.

Part I

Superconducting QUantum Interference Device Detection of Magnetotactic Bacteria

Chapter 4

Magnetotactic Bacteria

4.1 Introduction

In the early 70's, while collecting samples from the surface sediments of the salt marshes of Cape Cod, Massachusetts, Richard Blakemore observed a type of bacterium that appeared to respond to magnetic fields. As described in his 1975 letter to *Science* [20], these microorganisms migrated along the geomagnetic field lines in a northward direction. This behavior, which took on the name "magnetotaxis," was observed only when the cells were motile (swimming). These "magnetotactic" cells propelled themselves using a bundle of flagella (whip-like tails) at one end of their body, which they aligned to point along the field. Examining the physiology of the bacteria, Blakemore discovered chains of iron-rich crystals within each cell, each crystal enveloped by its own membrane vesicle (see Fig. 4.1). Outside the cell, the chains tended to form clumps, leading him to suggest that they were permanently magnetic, imparting a magnetic moment to the cells. As a result, Blakemore argued, these iron-rich inclusions, or "magnetosomes" as they are now called, could align to the geomagnetic field like a compass needle and point the motile cells northward, leading to magnetotaxis. In survival tests, it was discovered that the magnetotactic bacteria were microaerophiles. Since the geomagnetic North points predominantly downward (in New England, where the discovery was made, the Earth's field is inclined by 70° with respect to the horizontal), Blakemore suggested that magnetotaxis might aid the cells find favorable microaerobic conditions at the water-sediment interface at the bottom of the marshes.

Since that initial discovery, a wide variety of magnetotactic bacteria (or MTB's) have been discovered in all parts of the world. They have been found in various regions of

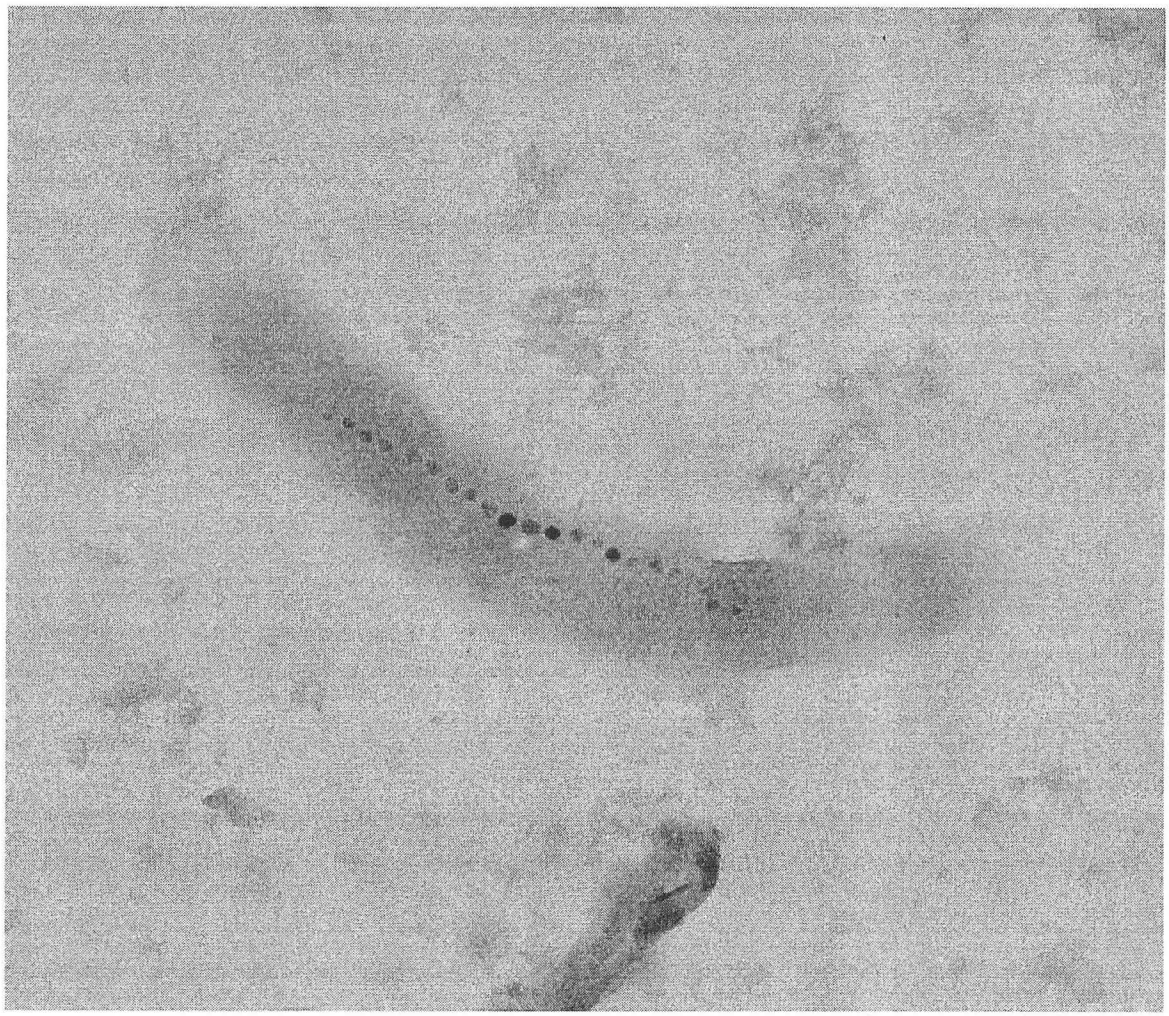

Figure 4.1: Transmission electron micrograph of the magnetotactic bacterium *Magnetospirillum magnetotacticum*. A chain of magnetite nanoparticles (magnetosomes), which gives the cell its magnetic moment, is clearly visible inside the bacteria.

the northern hemisphere, where, as in Blakemore's original discovery, the majority migrate towards the geomagnetic North; in the Southern hemisphere, where they are mostly "south-seeking" [21]; and along the equator, where equal populations of north- and south-seeking cells exist [22]. To date, magnetotactic bacteria have been found in a variety of habitats ranging from aquatic sediments to terrestrial soils to stratified water columns [23]. Despite these various habitats, however, they have always been found to inhabit microaerobic zones.

Blakemore's original magnetic bacteria were roughly spherical in shape with a diameter of $\sim 1 \mu m$ [20]. However, magnetotactic bacteria can come in a dizzying variety of shapes and sizes: coccoid (spherical), bacillus (rod-like), vibrio (curved), spirillum (spiral, see Fig. 4.1) and ovoid-shaped [23]. Their sizes range from less than a micron for the cocci, to several microns for the spirilla [24]; recently, a large, multicellular magnetotactic prokaryote containing 20 or so coccoid cells was observed [25].

This great diversity in morphology implies that magnetotaxis does not belong to a specific phylogenetic family of bacteria, but is an acquired trait dispersed among a large group [26]. Indeed, genetic studies have shown that there appears to be no real taxonomic significance to the term "magnetotactic." Most MTB's belong to the *Proteobacteria* phylum in the domain *Bacteria*; however, the nearest phylogenetic neighbors to MTB's are often non-magnetic bacteria [23]. Despite this morphologic and phylogenetic diversity, magnetotactic bacteria all have several features in common: 1) they are motile, 2) they are Gram-negative[1], 3) they are almost always microaerophilic, and 4) they contain magnetosomes [26].

4.2 Magnetotaxis

4.2.1 Description

Many bacteria—the most famous example being *E. coli*—exhibit what is called "run-and-tumble" motility, in which a cell swims for some distance, stops and reorients itself, then continues to swim in a new direction [27]. It has been suggested that such motility was developed because it is an efficient way of foraging large areas and ultimately helps the species to survive [28]. Similarly, magnetotactic bacteria seem to have developed

[1]The purple Gram stain is used to differentiate bacteria based on their outer membrane. Gram-positive bacteria have a single, thick cell wall that absorbs and retains the stain. Gram-negative bacteria have a two-layer cell membrane that remains colorless.

magnetotaxis to increase their chances of survival. As suggested earlier, magnetotaxis appears to be linked to the microaerophilic response of magnetotactic bacteria. Currently, magnetotaxis is understood as an efficient means of finding a favorable microaerobic zone—the so-called oxic-anoxic transition zone, or OATZ—where cells thrive [26].

During magnetotaxis, cells swim parallel or antiparallel to the magnetic field lines. In each hemisphere, the dipole moment is aligned with respect to the flagella in such a way that the cell always swims downward [see Fig. 4.2(a) for the Northern hemisphere, and 4.2(b) for the Southern hemisphere] until it reaches the OATZ. At the equator, where North- and South-seeking bacteria exist in equal numbers, cells presumably swim horizontally, maintaining their position in the OATZ [24, 29]. It is interesting that nature has worked out a way of aligning the magnetosome chain with the cell's flagella—and the direction of motility. Presumably, cells with the wrong polarity would not reach the OATZ and would selectively die out.

4.2.2 Alignment in the geomagnetic field

The overwhelming consensus among scientists is that the alignment of the bacteria to the geomagnetic field is not actively controlled by the cell. In the simplest model [30], magnetotactic bacteria are treated as self-propelled dipole moments. The geomagnetic field applies a torque on the magnetosome chain (and the cell, to which it is rigidly attached) which vanishes when the dipole moment lies parallel to the field. The alignment of the cell to the field is characterized by the deviation angle θ between the moment $\mathbf{m}$ and the field $\mathbf{B}$. In this simple model, the potential energy of the bacteria in the field is $E = -\mathbf{m}\cdot\mathbf{B} = -mB\cos\theta$. At thermal equilibrium, the probability density for the angle of deviation θ, $p(\theta)$, is proportional to the Boltzmann factor $e^{-E/k_BT} = e^{mB\cos\theta/k_BT}$.

A measure of the alignment of the bacteria to the geomagnetic field is the average cosine of the angle of deviation $\langle\cos\theta\rangle$, which is calculated from the probability density $p(\theta)$

$$\begin{aligned}\langle\cos\theta\rangle &= \frac{\int d\Omega\cos\theta\, e^{\xi\cos\theta}}{\int d\Omega\, e^{\xi\cos\theta}} = \frac{\partial}{\partial\xi}\ln\int_0^{2\pi}d\phi\int_0^{\pi}\sin\theta d\theta\, e^{\xi\cos\theta} \\ &= \coth\xi - \frac{1}{\xi} \equiv L(\xi), \end{aligned} \tag{4.1}$$

where Ω is the solid angle and $\xi \equiv mB/k_BT$ is the ratio of the magnetic alignment energy to the thermal energy. $L(\xi)$ is the standard Langevin function from the theory of

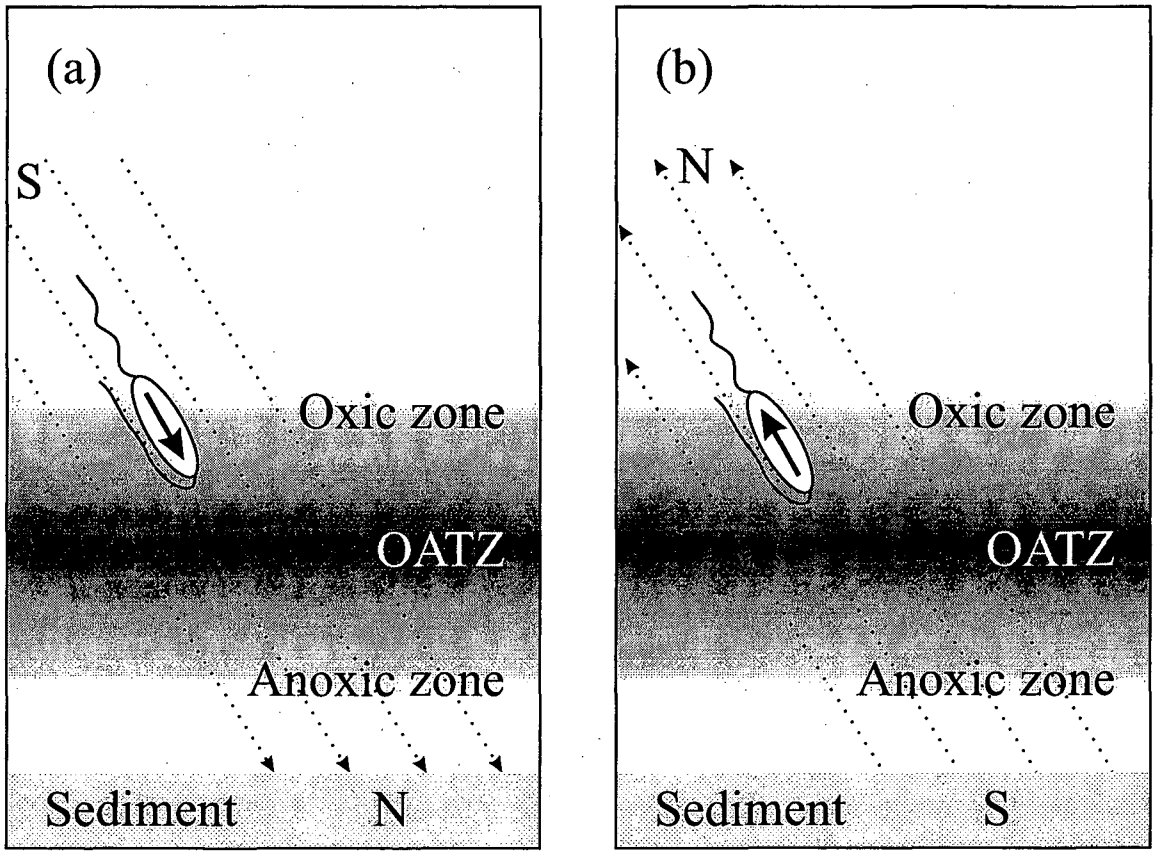

Figure 4.2: Magnetotaxis in the Northern (a) and Southern (b) hemispheres. The cells are aligned with respect to the geomagnetic field and swim downwards toward the oxic-anoxic transition zone (OATZ) where optimal microaerobic conditions exist. Once at the OATZ, they maintain their position by reversing direction whenever conditions are not optimal.

magnetization. The standard deviation of $\cos\theta$ is another useful parameter:

$$\sigma \equiv \langle\cos^2\theta\rangle - \langle\cos\theta\rangle^2 = 1 + \frac{1}{\xi^2} - \coth^2\xi = \frac{dL(\xi)}{d\xi}. \tag{4.2}$$

For small magnetic fields (such that $\xi \ll 1$), $\langle\cos\theta\rangle \approx \xi/3$ and $\sigma \approx 1/3 - \xi^2/15$, and for large fields ($\xi \gg 1$), $\langle\cos\theta\rangle \approx 1$ and $\sigma \approx 1/\xi^2$. The geomagnetic field has a magnitude of $\sim 50\mu T$; at room temperature, $\xi = 1$ corresponds to a dipole moment equal to $8 \times 10^{-17} A \cdot m^2$. As we will see shortly, the moments of healthy magnetotactic bacteria are up to ten times as large as this. For such values of ξ, a cell is almost perfectly aligned to the geomagnetic field, with very small deviations.

As a verification of this model, Kalmijn [30] analyzed the migration rates of individual magnetotactic bacteria as a function of the ambient magnetic field applied in one direction by a Helmholtz coil[2]. The average migration rate is the swimming speed of the cell times the average cosine of the deviation angle $\langle\cos\theta\rangle$, assuming the dipole moment is colinear with the direction of propulsion of the cell. The measured migration rates and their standard deviations for individual bacteria at different applied fields were fitted fairly well by Eq. (4.1) and (4.2), respectively. While this strongly suggests that the alignment of the bacteria to the field is a passive process, it does not completely rule out the remote possibility that the bacteria can actively control their swimming direction. To date, however, no direct evidence of such a mechanism has been found.

4.2.3 Aerotaxis

Clearly, the mechanism described above cannot alone explain magnetotaxis; otherwise, cells swimming along the geomagnetic field would continue past the oxic-anoxic transition zone into the toxic, anoxic zone. Magnetotactic bacteria possess a sensory system to detect oxygen concentrations in their environment. It is believed that this active aerotactic response will cause a cell to either stop or reverse direction if its environment is not optimal. Unlike *E. coli*, magnetotactic cells do not change direction by tumbling. The magnetic spirillum MS-1 (to be discussed below) has a flagellum at each end of its body, and uses one or the other to swim forward or backward. The magnetic vibrio MV-1 and the coccoid MC-1 have only one flagellum and reverse its direction of rotation to swim backward [26]. Because they can swim either along or against the field, species like the

[2] A Helmholtz pair consists of two identical coaxial coils separated a distance equal to their radius. This configuration gives the best field uniformity for two coils.

spirillum are called *bipolar*; the coccoid and the vibrio, which swim predominantly toward one pole, on the other hand, are called *polar*.

Studies by Frankel *et al.* [31, 32] have shed light on this mechanism. Cells in suspension were placed inside a long, rectangular capillary with both ends open to air. Diffusion of air into the capillary created an oxygen concentration gradient along the length of the capillary, highest at the ends and lowest in the middle. When a magnetic field was applied along the capillary axis, the cells migrated to regions of optimal oxygen concentration, forming microaerophilic, aerotactic bands in the capillary. The formation of bands indicates that an aerotactic response mechanism caused the cells to reverse direction when the oxygen concentration $[O_2]$ is not optimal.

Interestingly, bipolar cells such as *Magnetotacticum magnetospirillum* strain MS-1 formed two bands, one at each end of the capillary, while polar cells such as the magnetic cocci MC-1 formed a single band at one end, as determined by the direction of the field. Suspensions of bipolar bacteria contain an equal mixture of cells swimming parallel and antiparallel to the field. These findings suggest that the sensory mechanism for aerotaxis in bipolar cells is one which detects temporal changes in $[O_2]$. The change in $[O_2]$ with time determines the swimming direction. Since the oxygen gradient is the same at both ends of the capillary and the cells can swim along or against the field, two bands are formed. The behavior of polar bacteria, on the other hand, is not consistent with a temporal sensory mechanism. The aerotactic response here seems to be better described by a two-state system, where both the oxygen gradient and the orientation of the magnetic field determine the swimming direction [31, 32].

Thus, magnetotaxis is partly a passive process (in the alignment of the cells to the field) and an active one (in maintaining their position in the OATZ by reversing direction). However, it may appear that the bacteria's aerotactic response would be enough to maintain it in the OATZ, in which case it would be unnecessary for the cell to be magnetic. Clearly, the great expense in energy required in generating magnetosomes must have led to a significant evolutionary advantage or it would have never been developed. The advantage of magnetotaxis comes from the fact that the alignment of the cell to the geomagnetic field is so strong that thermal fluctuations do not significantly affect it ($\xi = mB/k_BT \gg 1$). In essence, the cell is confined to move in one dimension. Reducing the dimensionality of the cell's motility is presumably a means of increasing its efficiency in finding an optimal position in a gradient. Thus, a microaerophilic cell would find the OATZ much more

efficiently by a mechanism like magnetotaxis rather than by some other mechanism like run-and-tumble motility.

4.3 Magnetosomes and biosynthesis

The distinguishing feature of magnetotactic bacteria is the ability to take up large amounts of iron from the environment and biomineralizing single ferrimagnetic crystals. Magnetosomes are a marvel of biomineralization. They are nearly perfect, single crystals of magnetite (Fe_3O_4), or in some species, greigite (Fe_3S_4), with a remarkably narrow size distribution [26, 32, 33]. Among the many species of magnetotactic bacteria, magnetosomes range in size from 35-120nm and have various crystal morphologies. Below 35nm, magnetite nanocrystals become superparamagnetic and have no remanent magnetization. Above 120nm, crystals become multiple-domain; dipolar interactions between domains tend to reduce the dipole moment of the particle [32]. Thus, the magnetosomes are synthesized specifically to maximize their moment. Within a single cell, magnetosomes are arranged in a chain (in some species, multiple chains) with each dipole moment aligned magnetically end to end so as to impart the cell a net moment equal to the sum of the individual moments. The chain is rigidly fixed inside the cell, so that the entire cell rotates in response to a magnetic field.

Using the value for the magnetization of bulk magnetite ($M_s = 4.8 \times 10^5 A/m$), we expect the dipole moment of each magnetosome to be of order 10^{-17} to $10^{-16} A \cdot m^2$; for a whole chain, 10^{-16} to $10^{-15} A \cdot m^2$. Various techniques, including light scattering [34], birefringence [35], and magnetic force microscopy [36], have been used to measure dipole moments ranging between 2-5$\times 10^{-16} A \cdot m^2$. Direct optical observation of individual motile cells have also yielded that parameter. The measurement by Kalmijn [30] of the migration rate as a function magnetic field yielded values of 6.2 and 7.3$\times 10^{-16} A \cdot m^2$ for two individual cells. In another measurement, motile cells swimming along a magnetic field were caused to make a U-turn by reversing the field; the diameter of the turn and the time it took to make the turn were used to calculate the dipole moment. Esquivel *et al.* [37] used this method to characterize a wide variety of magnetic microorganisms. Of course, values vary depending on the species of magnetotactic bacteria and growth conditions. Measured dipole moments generally fall in the range 2-10$\times 10^{-16} A \cdot m^2$, corresponding to an alignment to the geomagnetic field of 60% to 90% as determined by the Langevin function.

Each magnetic nanocrystal is enveloped by a trilaminate lipid vesicle [38]. The vesicle membrane does not appear to be contiguous with the cytoplasmic membrane, but clearly, some structure must exist to anchor the vesicles within the cell and maintain the position of the magnetosome chain. In studies of iron-starved cells [38], empty or partially filled vesicles have been observed, indicating that they exist prior to magnetosome synthesis, and are filled individually during mineralization. It appears that one function of the vesicle is to limit the size of the nanocrystal synthesized within it. A more important function is to isolate the reaction center for magnetosome synthesis from the cell environment. Compartmentalization enables the processes of mineral formation to be regulated by biochemical pathways [33].

The biochemistry of magnetosome biosynthesis is not completely understood. Studies of the species *Magnetotacticum magnetospirillum* by high-resolution electron microscopy and Fe-57 Mößbauer spectroscopy have led to the following proposed biochemical pathway [33, 39]. Fe(III) is taken up by the cell and presumably reduced to (the more soluble) Fe(II) as it passes through the cell membrane. In the cytoplasm, it is reoxidized to form a low-density hydrous oxide, which is transported across the magnetosome vesicle membrane and dehydrated to form a high-density hydrous oxide (ferrihydrite, $Fe_2O_3 \cdot nH_2O$). Finally, magnetite is produced by reducing one third of the Fe(III) ions and by further dehydration of the oxide.[3]

The various enzymes which catalyze magnetite synthesis are largely unknown. Several studies have reported novel cytochromes[4] present in magnetic cells and absent in non-magnetic cells [33]. Magnetosome membranes also appear to contain several unique proteins not found in the cytoplasmic or outer membranes. Of these, at least one major protein (mol. weight 22-24kDa) is present in all of the strains studied. The functions of the magnetosome membrane proteins have not yet been determined, but it is very likely that they are involved in the accumulation and mineralization of iron [33].

It is interesting to note that cells do not grow magnetosomes under aerobic conditions [24]. It has been shown that the number of magnetosome is reduced and the cell's ability to take in iron from the environment is reduced under aerobic conditions. It is likely that oxygen inhibits at least one step in the magnetosome synthesis pathway [33].

[3]Magnetite has a structural formula $Fe^{3+}[Fe^{2+},Fe^{3+}]O_4$. Two thirds of the iron ions are in the Fe(III) oxidation state, one third in the Fe(II) state.

[4]Cytochromes are electron transport proteins which contain iron groups that alternate between their Fe(II) and Fe(III) oxidation states.

4.4 The SQUID microscope and magnetotactic bacteria

4.4.1 Magnetospirillum magnetotacticum

In the remainder of Part I, I will describe and discuss measurements carried out on magnetotactic bacteria using the SQUID microscope. It was necessary to cultivate our own bacteria in order to carry out these experiments systematically. For this purpose we obtained a culture of the magnetotactic bacterium *Magnetospirillum magnetotacticum*[5] strain MS-1. Professor Dennis Bazylinski at Iowa State University kindly provided us with starting cultures for our experiments. Since our laboratory lacked the equipment necessary to cultivate bacteria, we collaborated with Professor Bob Buchanan in the Plant and Microbial Biology Department, who let us use his laboratory in Koshland Hall on campus. Mike Adamkiewicz, a technician in Prof. Buchanan's group was brought in to assist us and proved invaluable. In the early stages of the collaboration we were also helped by Wanda Rivera, an undergraduate research assistant.

The cultivation of magnetotactic bacteria has posed a formidable challenge for microbiologists. While their isolation from the wild is relatively easy due to their abundance and the fact that they can be accumulated magnetically, creating conditions conducive to growth in the lab has proven difficult [23, 24]. *Magnetospirillum magnetotacticum* strain MS-1 was the first to be isolated and grown in axenic culture [24]. In recent years, only a handful of other magnetotactic bacteria have been successfully cultured [23].

Even though the magnetic spirillum MS-1 is not as common in nature as the coccoid [23], it has been extensively studied because it was the first to be isolated and cultured. The name spirillum refers to its corkscrew shape (see Fig. 4.1). As mentioned before, this bacterium is flagellated at both ends of its body and hence is known as bipolar; it can swim along or against magnetic field lines, depending on which flagellum is active. As seen in Fig. 4.1, the bacterium contains a single chain of 20 or so magnetosomes. They are composed of magnetite (Fe_3O_4) and roughly $35nm$ in size. Measured dipole moments have ranged from $2\text{-}5\times10^{-16} A \cdot m^2$ [34, 35, 40].

[5] In the older literature, this bacterium is classified as *Aquaspirillum magnetotacticum*.

4.4.2 Cultivation and harvesting protocol

Professor Dennis Bazylinski provided us with a protocol for growing *Magnetospirillum magnetotacticum* in a microaerobic environment. The liquid growth medium (see Table 4.1) consists of a range of vitamins (see Wolfe's vitamin solution [41], Table 4.2) and trace amounts of minerals (see the modified Wolfe's mineral solution [41], Table 4.3). The growth medium contains the oxygen indicator resazurin; as oxygen concentration is decreased it turns the solution purple, then pink, then clear. Thus, by monitoring the color of the medium, we can determine if optimal microaerobic growth conditions have been attained. The source of iron in the production of magnetosomes is provided by the 0.01 M ferric quinate solution. The ingredients are added in the order listed and the pH of the medium is adjusted to 6.75 with 1 N NaOH.

To maintain microaerobic conditions, the growth medium and bacteria must be placed in sealed glass vials. Following Bazylinski's instructions, we obtained $125mL$ Wheaton serum bottles (Fisher, catalog number 06-406K), anaerobic rubber stoppers (Bellco Glass, cat. no. 2048-11800) to plug the bottles, and $20mm$ aluminum crimp seals (Fisher, cat. no. 06-406-14B) to seal the bottles. This provides an adequate seal; in most cases the medium does not change color over time, indicating that no air is leaking into the bottles.

After the medium is prepared, $55mL$ of it is dispensed into each glass bottle, leaving a significant head space. The medium is deoxygenated in two steps: first, nitrogen gas is bubbled into the solution for 30 minutes, then, the head space is purged with nitrogen gas for another 30 minutes. We obtained a cylinder of compressed N_2 gas and connected it to a manifold of valves, through which we could gas as many as 25 bottles. Out of every valve we connected a length of plastic tubing, at the end of which we attached an 18-gauge syringe needle. In the first step the end of each syringe needle is fitted with teflon tubing, and fed through the neck of each bottle into the liquid [see Fig. 4.3(a)]. The pressure of the gas cylinder is adjusted so that the N_2 lightly bubbles out of the teflon tubing. To prevent oxygen from the air from entering the bottle through the neck, a rubber stopper is pushed in from the top tightly against the side of the needle and tubing [see Fig. 4.3(a)]. As the medium is reduced it turns purple then pink.

After a half hour or so, the teflon tubing is removed carefully, making sure the rubber stopper does not fall off. Each stopper is then pushed in completely and crimped with an aluminum seal using a crimp tool (Fisher, cat. no. 10-319-490). Removing the teflon

Ingredient	Amount
Wolfe's Vitamin Solution	$10.0mL$
Wolfe's Mineral Solution	$5.0mL$
KH_2PO_4	$0.68g$
Sodium succinate*$6H_2O$	$0.848g$
Sodium tartrate*$2H_2O$	$0.575g$
Sodium acetate*$3H_2O$	$0.083g$
0.1% Resazurin (aqueous)	$0.45mL$
$NaNO_3$	$0.17g$
Ascorbic acid	$0.035g$
0.01M Ferric quinate solution[a]	$2.0mL$
Distilled, deionized water	$1L$

[a]Dissolve $0.19g$ of quinic acid into $100mL$ distilled, deionized water. Add $0.27g$ of $FeCl_3$*$6H_2O$, and stir to dissolve

Table 4.1: Recipe for $1L$ of growth medium for *Magnetospirillum magnetotacticum*. See recipes for Wolfe's vitamin and mineral solutions below.

Ingredient	Amount
Biotin	$2mg$
Folic acid	$2mg$
Pyridoxine hydrochloride	$10mg$
Thiamine hydrochloride	$5mg$
Riboflavin	$5mg$
Niacin	$5mg$
D,L Ca^{2+} pantothenate	$5mg$
Vitamin B_{12} (crystalline)	$0.1mg$
Para-amino benzoic acid (PABA)	$5mg$
Lipoic (thioctic) acid	$5mg$
Distilled, deionized water	$1L$

Table 4.2: Recipe for $1L$ of Wolfe's vitamin solution [41]. The solution is filter sterilized—not autoclaved—and is stored at 4°C in the dark.

Ingredient	Amount
Nitrolotriacetic acid (NTA)[a]	$1.5g$
$MgSO_4*7H_2O$	$3.0g$
$MnSO_4*H_2O$	$0.5g$
NaCl	$1.0g$
$FeSO_4*7H_2O$	$0.1g$
$CoCl_2*6H_2O$ or $CoSO_4*7H_2O$	$0.1g$
$CaCl_2*2H_2O$	$0.1g$
$ZnSO_4*7H_2O$	$0.1g$
$CuSO_4*5H_2O$ (0.5 μM)	$0.025g$
$AlK(SO_4)_2*12H_2O$	$0.01g$
H_3BO_3	$0.01g$
$Na_2MoO_4*2H_2O$	$0.4g$
$NiCl_2*6H_2O$	$0.01g$
Distilled, deionized water	$1L$

[a] Add NTA to $500mL$ of distilled, deionized water and adjust pH to 6.5 with saturated KOH. Note: NTA is a carcinogen.

Table 4.3: Recipe for $1L$ of modified Wolfe's mineral solution [41]. The solution is sterilized by autoclaving, and is stored at 4°C in the dark.

tubing from the syringe needles, we insert the needles into the stoppers and flow N_2 into the head spaces [see Fig. 4.3(b)]. An outlet needle is also needed so no positive pressure develops inside the sealed bottles. At the end of this step, the needles are removed and the bottles are sterilized by autoclaving at 121°C and 15 psi for 15 min. Upon cooling, the medium is colorless or very slightly pink, indicating that it has been completely deoxygenated. At this point, the bottles may be stored at room temperature in the dark.

Before inoculating a bottle with cells, we add $5mL$ of sterile air to it. In this way, the final concentration of oxygen is 1%, optimal for production of magnetite. We devised a way of collecting sterile air by using an empty Wheaton glass vial sealed at the top with a stopper and an aluminum crimp. We inserted a thick-gauge needle through the stopper, and fitted the end of the needle with a length of rubber tubing which was filled with cotton fiber. Every time new medium is prepared for inoculation, this bottle is autoclaved. To collect the air, we simply stick a syringe through the stopper of the sterile air bottle and withdraw $5mL$. The cotton-filled tube filters out any microorganisms from the outside, so that the air inside the bottle is always sterile. After injecting the air into the medium, it is shaken to dissolve the oxygen, and turns very pink within an hour. At this point, conditions are optimal and the bottle is ready for inoculation.

Typically, the medium is inoculated with $5mL$ of bacteria from a previous culture, and the bottles are incubated at 27°C. On average it takes 2-3 days of incubation for the cultures to reach stationary phase (where the cell population ceases to grow exponentially), at which point the cell count is typically on the order of 10^8 cells/mL. Figure 4.4 shows two representative growth curves. The standard method for determining cell concentrations is by measuring optical absorbance at a particular wavelength. Attempts to use this technique were unsuccessful, we suspect because the cell densities were too low for an accurate measurement, and because of the color of the growth medium. Instead we chose to use a Petroff-Hausser bacteria counting chamber (Hausser Scientific, cat. no. 3900), which consists of a glass cell of known depth (20 μm) marked with a square grating pattern (each square is $50\mu m \times 50\mu m$). By placing the chamber under a phase contrast microscope, it is possible to count bacteria in the square grating pattern and determine cell density. To facilitate counting, we often immobilize the bacteria in the counting chamber by adding a drop of formalin or iodine. Cells are harvested at the end of the logarithmic growth phase (where the cell population increases exponentially) before the stationary phase to ensure that there is a large number of live cells. We typically check the culture under an optical

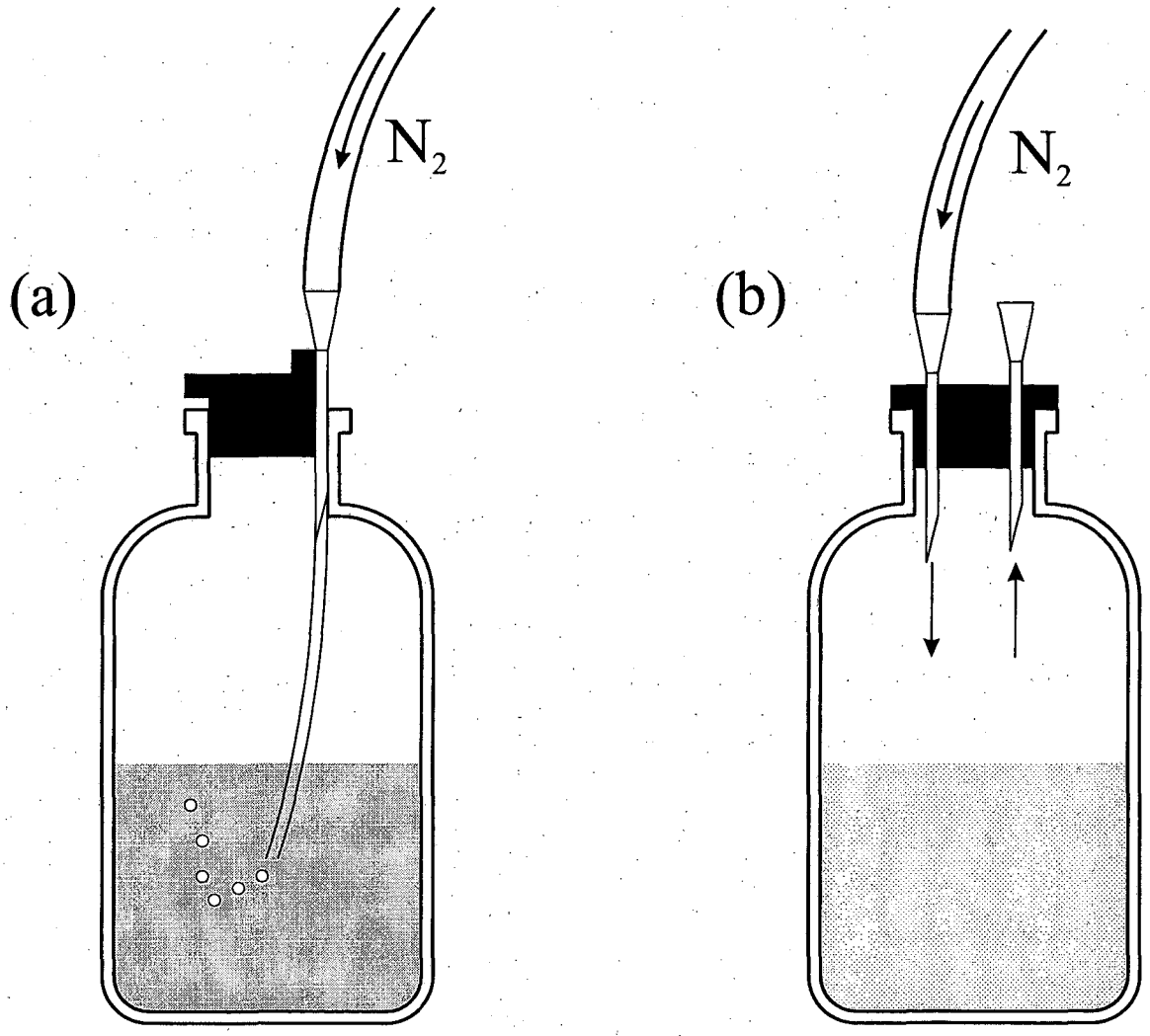

Figure 4.3: Protocol for microaerobic growth medium. (a) The medium is deoxygenated by bubbling N_2 through a teflon tube immersed in the solution. A rubber stopper pressed against the tube prevents oxygen from the air from entering. (b) The headspace of the medium bottle is purged with N_2 flowed into an inlet syringe needle and out of an outlet needle pressed through the stopper.

microscope and make sure that a large fraction of the bacteria are motile (swimming) before harvesting them for a measurement.

After a set of measurements is completed, it is possible to save the cultures by storing the bottles in the dark at 4°C. In this way the cultures are dormant but may be reanimated at a later time and used to inoculate new medium. Usually we find that cultures inoculated in this way take longer to reach stationary phase, but subsequent "generations" go back to the normal growth rates. We have also attempted to freeze-dry cultures, but we were unable to revive them subsequently.

4.4.3 Experimental configuration

As indicated above, special measures are taken to grow the bacteria in a microaerobic medium. In the course of a measurement with the SQUID microscope, it is equally important to maintain the cultures in a friendly environment. Early in our studies of magnetotactic bacteria, we had difficulty maintaining healthy cultures on the microscope. Presumably, lethal levels of oxygen were diffusing into the medium, killing the bacteria. After investigating several different sample cell configurations, we settled on a design which successfully addresses this issue. The problem of oxygen contamination is resolved in two ways: first, the sample chamber is made air-tight and is flushed with a microaerobic gas mixture, and second, large volumes ($\sim 1mL$) of bacteria samples are used.

The sample chamber for the bacteria is integrated with the Si/SiN vacuum window of the SQUID microscope, with the silicon well facing outside. As shown in Fig. 4.5, the chamber consists of a quartz tube (OD $15mm$, length $15mm$) glued on top of the vacuum window and sealed at the top with a rubber stopper (the same kind used in the growth medium bottles). Initially, we used Crystalbond 509 adhesive wax to attach the tube to the window, fearing that uncured chemicals in two-part epoxies could leach out into the sample, affecting the bacteria. Later, noticing that the wax slowly dissolved upon repeated cleaning of the chamber, we switched to Stycast 1266 (clear) epoxy, which has stronger mechanical properties and does not dissolve as easily. The epoxy does not seem to affect the health of the bacteria. The rubber stopper provides the air-tight seal needed to maintain optimal conditions for the bacteria.

Prior to a measurement, we clean the cell with a detergent like RBS soap (more recently we have used sodium dodecyl sulfate (SDS), a protein denaturant), sterilize it with

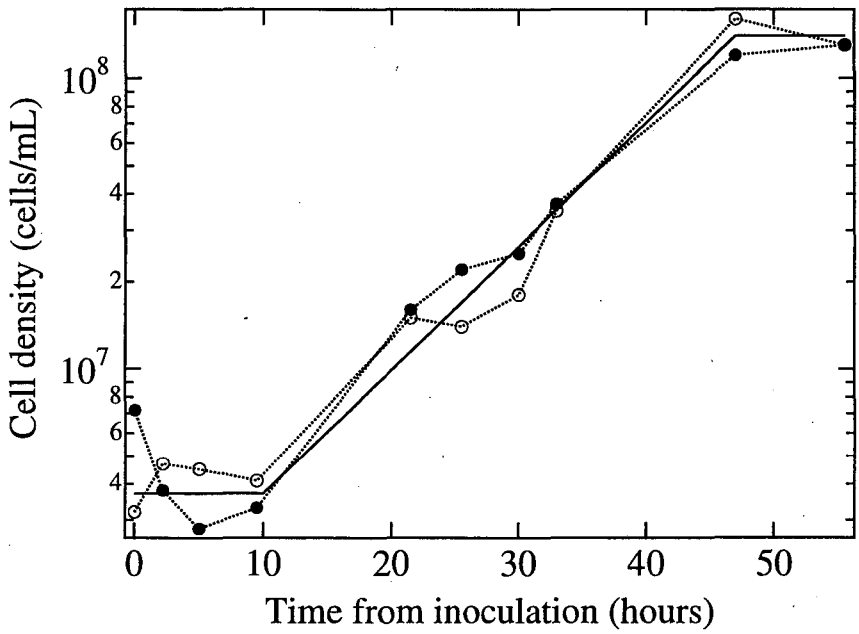

Figure 4.4: Representative growth curves for *Magnetospirillum magnetotacticum*. Typically, a culture will go through a lag phase (in which the population is relatively constant), a log phase (in which it increases exponentially), and a stationary phase (in which it ceases to grow exponentially and begins to die). We harvest bacteria at the end of the log phase, where density and motility is highest.

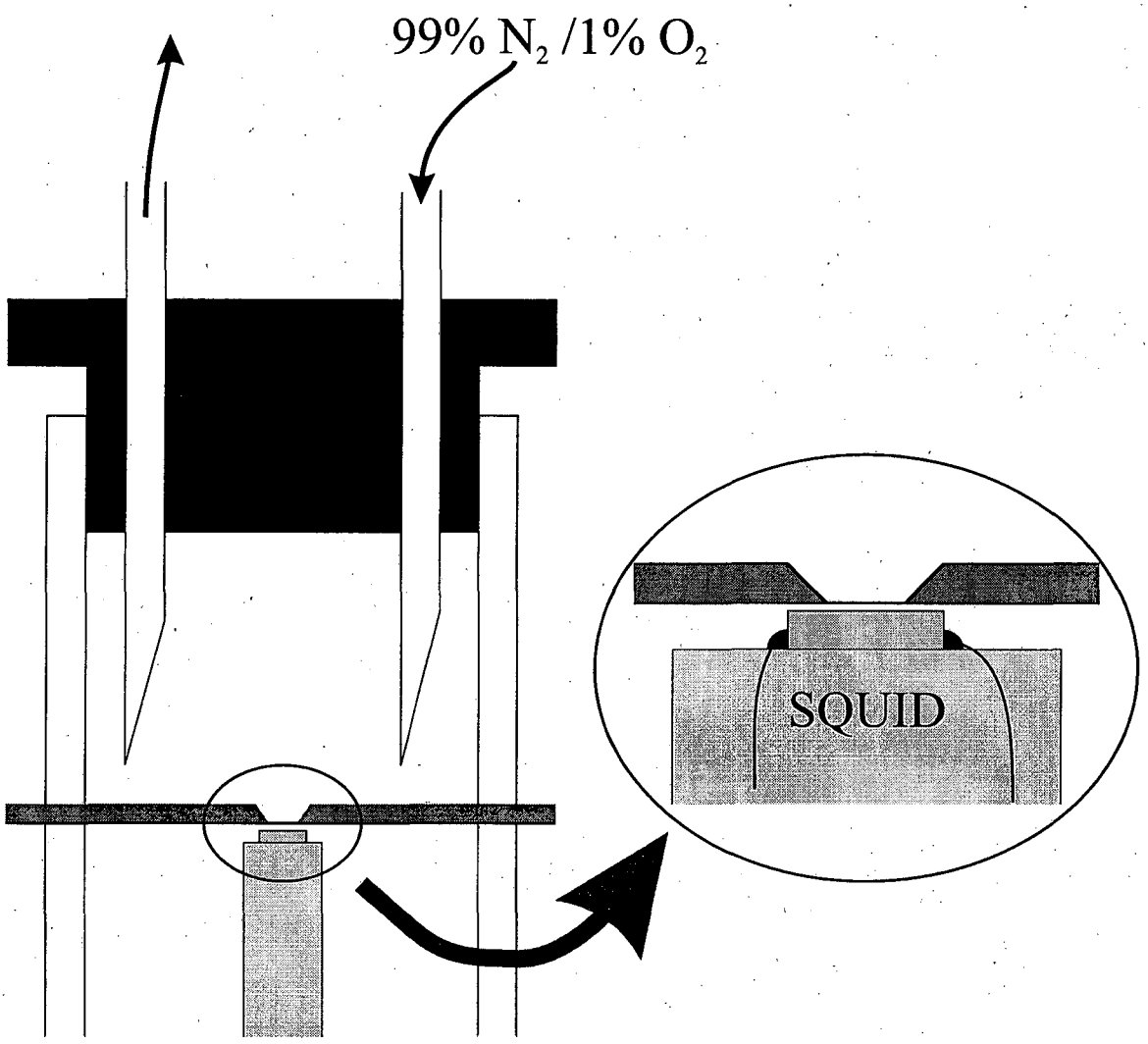

Figure 4.5: Sample chamber. A quartz tube is glued to the vacuum window of the SQUID microscope and sealed at the top with a rubber stopper. An inlet and outlet needle can be pressed through the stopper to purge the chamber with gas prior to a measurement.

ethanol, and dry it with compressed N_2 gas. The sample chamber is then purged with a gas mixture composed of 1% O_2 and 99% N_2, reproducing the microaerobic conditions inside the growth bottles. A compressed gas cylinder flows this mixture through the chamber via an inlet and an outlet syringe needle that are pressed through the rubber stopper (see Fig. 4.5). The pressure from the cylinder is adjusted so that a small flow is established; if the pressure is too large, the stopper may pop off the quartz tube. The gas from the cylinder is sterilized before reaching the chamber by passing through a column stuffed with cotton fiber. The mixture is flowed through the chamber continuously for 15 minutes, after which the sample is added. With a syringe, we typically extract $1mL$ of bacteria in growth solution from a bottle, and inject it through the stopper into the sample chamber. The syringe is then removed, followed by the two gas needles.

Although the chamber is sealed by a rubber stopper, there may still be oxygen leaks. By using such a large sample volume, we minimize the surface area-to-volume ratio, diminishing the effects of any oxygen leaks on the culture. In this way, we can maintain healthy cultures on the microscope for several hours. This sample cell design and the protocol described above allow us to carry out a variety of measurements on live magnetotactic bacteria with the SQUID microscope. In the next chapter, these experiments are described in detail.

Chapter 5

SQUID Measurements of Magnetotactic Bacteria

5.1 Introduction

It is apparent from the previous chapters that the SQUID microscope should be capable of detecting the motion of live magnetotactic bacteria. The clear advantage of the warm-sample microscope is its ability to maintain a healthy biological sample during a measurement. While the spatial resolution of the device is clearly insufficient to image individual cells, at least its magnetic dipole sensitivity should allow detection of the dipole moment of a single bacterium (see Section 3.3.1). It was this tantalizing possibility coupled to a long-standing interest in biology which initially motivated the building of our SQUID microscope [18]. However, the prospect of detecting the dipole moment of a magnetotactic bacterium in itself is not so interesting; by performing time-resolved measurements on live cells we are able to gather information on their dynamics as well. The extraordinary measurement bandwidth of the SQUID (from several mHz to 10kHz) allows us to probe a wide range of frequencies, some not easily accessible by standard optical techniques.

In this chapter I will describe several measurements of *Magnetospirillum magnetotacticum* with the SQUID microscope. As described in the previous chapter, special care is taken to reproduce the conditions found in the wild in the sample cell of the microscope. One crucial difference, however, is that the μ-metal surrounding the microscope reduces the ambient magnetic field in the sample cell to a negligibly small value. For all practical

purposes, the bacteria are in a zero-field environment[1], and do not undergo magnetotaxis. However, it is possible to apply a known magnetic field using a set of coils integrated with the microscope. In this way, we can monitor the bacteria's magnetotactic response in a very controllable fashion.

In the experiments described below, a suspension of bacteria is placed in the sample cell of the microscope. Each MTB, with its permanent dipole moment, generates a time-varying flux in the SQUID as it translates and rotates. As we will see, there are situations where the SQUID produces a time trace of the flux due to a single magnetotactic bacterium. However, the flux generated by an ensemble of bacteria, because each cell is oriented differently and couples differently to the SQUID, in general averages to zero. There are two ways of getting around this problem. The first is to measure fluctuations in the flux—or flux noise—instead of the flux itself. The power spectrum of the flux noise, or the flux noise spectral density, $S_\Phi(f)$, is a measure of the fluctuations at a given frequency. The other method is to break the symmetry which makes the average flux zero by applying a magnetic field to align the bacteria. One can measure the time-varying flux—the flux response function, $\langle\Phi(t)\rangle$—when a field is turned on or off.

This chapter is broken down into several sections: one devoted to ensembles of nonmotile bacteria (Section 5.2), another to ensembles of motile bacteria (Section 5.3). In each I present measurements of the flux noise $S_\Phi(f)$ or the response function $\langle\Phi(t)\rangle$ in the presence or absence of a magnetic field. Finally, in Section 5.4, I present observations of single magnetotactic bacteria with the SQUID microscope.

5.2 Nonmotile bacteria

5.2.1 Noise in zero magnetic field

The upper curve in Fig. 5.1(a) is the power spectrum of the magnetic flux noise, $S_\Phi(f)$, generated by an ensemble of nonmotile[2] *Magnetospirillum magnetotacticum* in zero magnetic field. The data is well described by a Lorentzian, a function of the form

$$S_\Phi(f) \propto \frac{1}{1+(2\pi f\tau_o)^2} \tag{5.1}$$

[1]Inside the shield, the geomagnetic field is reduced from $50\mu T$ to about $5nT$. The DC field produced by the modulation coil of the SQUID was at most $3\mu T$ inside the sample cell, and the 100kHz AC field was kept under $0.4\mu T$ [18].

[2]Typically, several drops of iodine are added to a culture to render it nonmotile.

which is flat below the knee frequency $1/2\pi\tau_o$, and falls off as $1/f^2$ above. The white noise of the SQUID (type slit A-C) was $25\mu\Phi_o/\sqrt{Hz}$, far below the noise produced by the bacteria. To understand why nonmotile bacteria generate a Lorentzian noise spectrum we must look into their dynamics.

Nonmotile cells undergo translational and rotational Brownian motion. The diffusion constant for both translations and rotations is of the form k_BT/α, where α is the viscous drag coefficient [27, 42] and depends on the exact geometry of the microorganism and whether the motion is translational or rotational. The time scales associated with the translational and rotational diffusion of a bacterium are radically different. As an illustration, suppose our bacteria are spheres of radius r. The translational and rotational diffusion constants, D_t and D_r, are [27]

$$D_t = \frac{k_BT}{6\pi\eta r}, \qquad D_r = \frac{k_BT}{8\pi\eta r^3} \tag{5.2}$$

where $\eta = 10^{-3} Pa \cdot s$ is the viscosity of water. For a spherical cell of radius $1\mu m$ at room temperature, $D_t = 0.21\mu m^2/s$ and $D_r = 0.16 s^{-1}$. A bacterium of that size diffuses a distance $d = \sqrt{2D_t t}$ [42] comparable to the spatial resolution of the SQUID microscope—in our case, about $40\mu m$ for the smallest SQUID used (type hole L2)—in about an hour. On the other hand, the bacterium rotates by an appreciable angle $\theta = \sqrt{2D_r t}$ [27], say 90°, in less than 10s. Since the SQUID cannot resolve translations much smaller than its spatial resolution and translational Brownian motion occurs over such a long time scale, we can safely make the assumption that the *position* of each bacterium is fixed over the measurement time scale, and that *translational* diffusion does not contribute to the measured noise. On the other hand, the *orientation* of each cell does change significantly over a shorter time, so that *rotational* diffusion is predominantly responsible for the measured flux noise.

The flux noise spectral density $S_\Phi(f)$ is defined as the Fourier transform of the autocorrelation function $C_\Phi(t)$

$$S_\Phi(f) \equiv \mathcal{F}\{C_\Phi(t)\} = \int_{-\infty}^{\infty} dt\, e^{2\pi i f t} \langle \Delta\Phi(t)\Delta\Phi(0)\rangle \tag{5.3}$$

where $\Delta\Phi = \Phi - \langle\Phi\rangle$. Note that in the absence of an aligning magnetic field $\langle\Phi\rangle = 0$, so that $C_\Phi(t) = \langle\Phi(t)\Phi(0)\rangle$. Writing $\Phi(t)$ is an abbreviation signifying $\Phi(\mathbf{r}(t), \theta(t), \phi(t))$ since the flux depends on the positions $\mathbf{r}(t)$ and orientations $\theta(t)$, $\phi(t)$ of the bacteria. Appendix A shows that the flux from one bacterium can be written as

$$\Phi(t) = \Phi_z(\mathbf{r})\cos\theta(t) + \Phi_x(\mathbf{r})\sin\theta(t)\cos\phi(t) + \Phi_y(\mathbf{r})\sin\theta(t)\sin\phi(t) \tag{5.4}$$

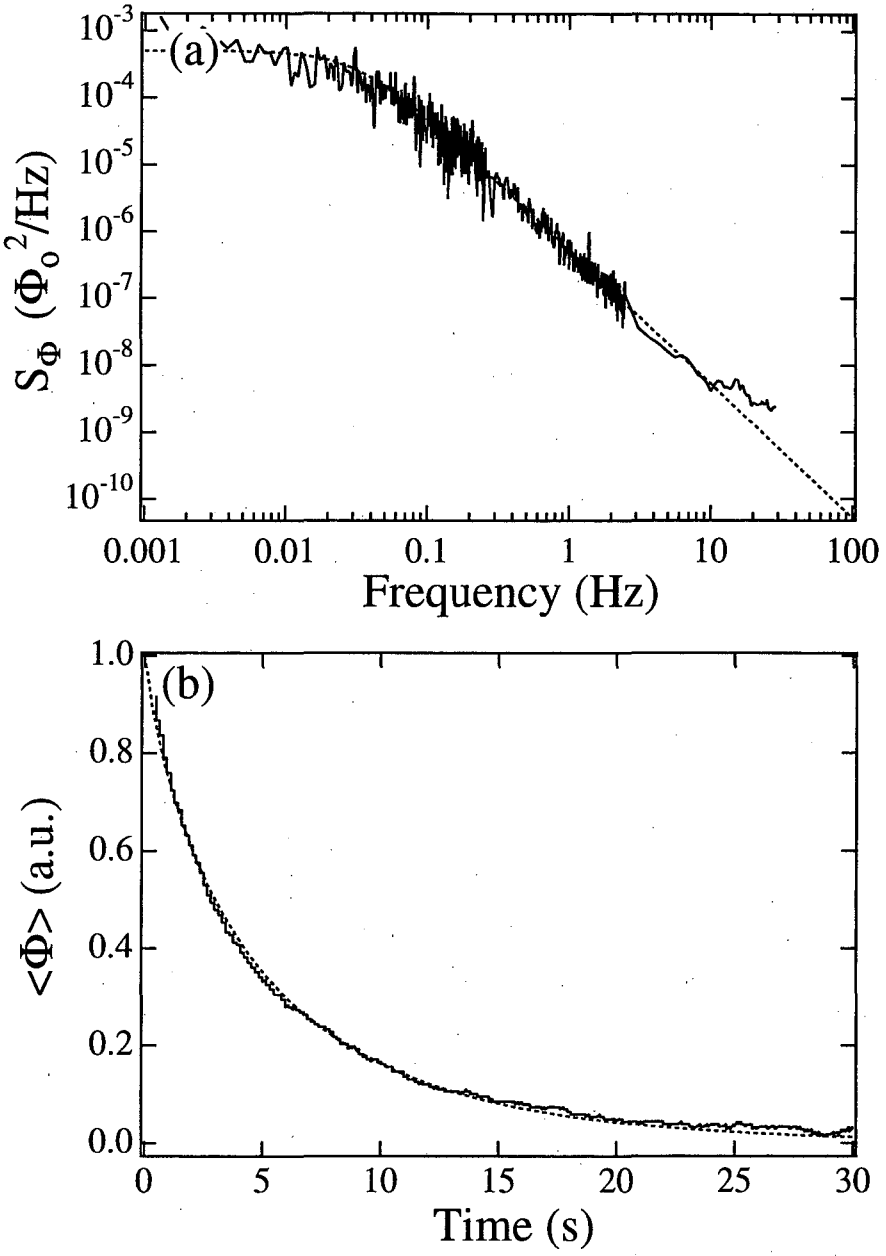

Figure 5.1: Nonmotile bacteria. (a) Power spectrum of the flux noise produced by the Brownian rotation of the bacteria in zero magnetic field (upper spectrum). (b) Time-varying response of the bacteria to a magnetic field pulse. At t=0, a uniform $96\mu T$ field is turned off and the magnetic flux produced by the bacteria decays as their orientations randomize. The curve is fit to an exponential to obtain τ_o.

The parameters Φ_i, $i = x, y, z$ describe the coupling of the three vectorial components of the cell's dipole moment to the SQUID for a given position $\mathbf{r}$. Note that I have implicitly removed the time dependence of the position variable $\mathbf{r}$, since I am ignoring translational diffusion. From Eq. (5.4), the flux autocorrelation function is

$$\begin{aligned} C_\Phi(t) &= \mathcal{G}_z^{(s)} \langle \cos\theta(t) \cos\theta(0) \rangle + \mathcal{G}_x^{(s)} \langle \sin\theta(t) \cos\phi(t) \sin\theta(0) \cos\phi(0) \rangle \\ &+ \mathcal{G}_y^{(s)} \langle \sin\theta(t) \sin\phi(t) \sin\theta(0) \sin\phi(0) \rangle \end{aligned} \tag{5.5}$$

where $\mathcal{G}_i^{(s)} \equiv \int d^3\mathbf{r}\, \rho_b\, \Phi_i^2(\mathbf{r})$, $i = x, y, z$, averages over all possible positions given the bacterial density ρ_b (see Appendix A). Appendix B demonstrates why all the cross-terms obtained in squaring Eq. (5.4) average to zero.

The usefulness of Eq. (5.5) is that it expresses the flux autocorrelation function in terms of autocorrelation functions of the orientation angles θ and ϕ, which can be calculated analytically. This calculation, which involves the Fokker-Planck equation, is outlined in Appendix B. Not surprisingly, considering the symmetry of the problem, all three angular autocorrelation functions are equal to each other

$$\begin{aligned} \langle \cos\theta(t) \cos\theta(0) \rangle &= \langle \sin\theta(t) \cos\phi(t) \sin\theta(0) \cos\phi(0) \rangle \\ &= \langle \sin\theta(t) \sin\phi(t) \sin\theta(0) \sin\phi(0) \rangle = \frac{1}{3} e^{-2D_r|t|} \end{aligned} \tag{5.6}$$

Taking the Fourier transform to determine the spectral density $S_\Phi(f)$, we obtain a Lorentzian

$$S_\Phi(f) = \frac{\mathcal{G}^{(s)}}{3} \frac{2\tau_o}{1 + (2\pi f \tau_o)^2} \tag{5.7}$$

where $\mathcal{G}^{(s)} = \mathcal{G}_z^{(s)} + \mathcal{G}_x^{(s)} + \mathcal{G}_y^{(s)}$. τ_o is the characteristic time scale of the Brownian rotation, and is given by $1/2D_r = \alpha_r / 2k_B T$.

Thus, the knee frequency in the data determines the rotational drag coefficient α_r, which is determined by the size and geometry of the bacteria. A better hydrodynamic model than a sphere for *Magnetotacticum magnetospirillum* is a rigid cylinder of length L and diameter d. Tirado *et al.* [43] give the following expression for the drag coefficient of such an object:

$$\alpha_r = \frac{\pi \eta L^3}{3} \left[\ln\left(\frac{L}{d}\right) - \gamma \right]^{-1} \tag{5.8}$$

where $\gamma \approx 0.662 - 0.92\ d/L$ is a numerical correction for the ends of the cylinder. α_r depends strongly on the length L and weakly on the diameter d.

To model for a real ensemble of bacteria, we have to account for a distribution of sizes, which lead to a distribution of characteristic times τ_o. It is well known that such a distribution can modify an exponential $\exp(-t/\tau_o)$ (for example, in an autocorrelation function) to a so-called "stretched exponential" $\exp(-(t/\tau)^\nu)$, with $\nu \leq 1$ [44]. The Fourier transform is Lorentzian-like, but falls off as $1/f^{1+\nu}$.

The spectrum of Fig. 5.1(a) is better fit by a function which falls off as $1/f^{1.9}$, not $1/f^2$. Thus, we fit the data to a distribution of Lorentzians with an average characteristic time $\bar{\tau}_o = 4.9s \pm 0.3s$. The average rotational drag coefficient is $\bar{\alpha}_r = (3.9 \pm 0.3) \times 10^{-20} N \cdot m$. The fitting parameters are the average length $\bar{L}$ and the half-width at half-maximum (HWHM) of the distribution ΔL. Assuming $\eta = 10^{-3} Pa \cdot s$ and $d = 0.7\mu m$, we find $\bar{L} = 3.5 \pm 0.1\mu m$ and $\Delta L = 0.7\mu m$, values that are consistent with our optical measurements and those by other groups [35, 37, 40, 45, 46].

5.2.2 Relaxation in zero magnetic field

As discussed in the introduction, one can measure the response of the bacteria to an external field. Figure 5.1(b) shows the decrease in the flux produced by an ensemble of nonmotile bacteria when a $96\mu T$ field is turned off at t=0. Initially the cells are aligned with the external field, giving the sample a net dipole moment which is detected by the SQUID. When the field is removed, the orientations of the bacteria randomize, leading to an average zero flux.

The magnetic field was applied to the sample with a set of four coaxial coils. I designed a set of coils configured to produce a highly uniform field B in the sample cell to minimize forces $\nabla(\mathbf{m} \cdot \mathbf{B})$ on the bacteria due to field gradients ∇B. The geometry of the sample cell did not allow for a Helmholtz pair configuration. Instead, I arranged two pairs of coils on the same axis, the inner pair to generate most of the field, the outer pair to improve uniformity. With this configuration, the uniformity $\Delta B/B$ was better than 0.1% across the entire sample. In addition, the field was applied parallel to the plane of the SQUID (along the $\hat{y}$-axis, as defined in Fig. A.1) to within 0.1° so that only about 0.1% of the field or less was sensed by the SQUID. Applying the field normal to the SQUID would have generated an inordinate amount of noise in it, making the measurement impractical. To align the field accurately parallel to the SQUID, the coil stage was equipped with a set of three aligning screws which rested on the top fiberglass basepiece to which the window/quartz

tube assembly was mounted. Finally, for a sample magnetized in-plane, the flux in the center is zero by symmetry. As a result, the SQUID was laterally displaced by approximately half the size of the sample cell ($\sim 220\mu m$) for optimal coupling.

Once the field is turned off, the bacteria randomize in a characteristic time again determined by the rotational diffusion constant D_r. As explained in Appendix B, the response of the bacteria to a magnetic field pulse is of the form

$$\langle \Phi(t) \rangle = \mathcal{G}_y^{(r)} L(\xi) e^{-t/\tau_o} \tag{5.9}$$

with $\tau_o = 1/2D_r = \alpha_r/2k_BT$ as in Eq. (5.7). $L(\xi)$ is the Langevin function defined in Eq. (4.1), $\xi \equiv mB/k_BT$. The curve in Fig. 5.1(b) is fitted to such an exponential. Since the field pulse generates a transient (which lasts $< 100ms$) that is detected by the SQUID, data for times $< 0.5s$ were ignored in the fit. Again, we account for the distribution of sizes by fitting to data to a stretched exponential $\exp(-(t/\tau)^{0.9})$. We find $\bar{\tau}_o = 4.7s \pm 0.3s$ and hence $\bar{\alpha}_r = (3.8 \pm 0.1) \times 10^{-20} N \cdot m$, in excellent agreement with the values from the noise measurements. The time-domain response of the bacteria to a magnetic field pulse is an alternate method of obtaining α_r.

5.2.3 Noise in a magnetic field

Application of a static magnetic field $B = 100\mu T$ to the sample used in Fig. 5.1(a) produces the lower curve in Fig. 5.2(a). The upper curve is the same data as in Fig. 5.1(a) and is included for comparison. The noise is again Lorentzian-like. Compared to the zero-field data, the spectrum below the knee is significantly reduced. By aligning the bacteria, the field reduces fluctuations of their orientation due to Brownian rotation. The knee frequency is larger so that the $1/f^2$ regions of the two spectra coincide. Presumably, the short-time (or high-frequency) dynamics of the bacteria are unaffected by the aligning field.

We can use the noise spectrum in the field to calculate the average dipole moment m of the bacteria. As shown in Appendix B, there is no simple analytical solution to the problem; rather, I have presented two approximate solutions in the limit of small field ($\xi \ll 1$) and large field ($\xi \gg 1$). For $B = 100\mu T$ we will assume that $\xi \gg 1$ and use the large field solution to fit the spectrum. Since the symmetry is broken by the magnetic field, the solution consists of *two* Lorentzians with different knee frequencies, corresponding to

components parallel and perpendicular to the field,

$$S_\Phi(f) = \frac{\mathcal{G}_{||}^{(s)}}{\xi^2}\frac{2\tau_{B,||}}{1+(2\pi f\tau_{B,||})^2} + \frac{\mathcal{G}_{\perp}^{(s)}}{\xi}\frac{2\tau_{B,\perp}}{1+(2\pi f\tau_{B,\perp})^2} \tag{5.10}$$

The subscripts $||$ and $\perp$ designate parallel and perpendicular to the field, respectively. Thus, since the applied field lies along the $\hat{y}$-axis, $\mathcal{G}_{||}^{(s)} = \mathcal{G}_y^{(s)}$ and $\mathcal{G}_{\perp}^{(s)} = \mathcal{G}_z^{(s)} + \mathcal{G}_x^{(s)}$. Finally, $\tau_{B,||} = \tau_o/\xi = \alpha_r/2mB$ and $\tau_{B,\perp} = 2\tau_o/\xi = \alpha_r/mB$ in the high field limit.

The spectrum in Fig. 5.2(a) is fitted to Eq. (5.10). The geometrical factors $\mathcal{G}_{x,y,z}^{(s)}$ retain their values from the fit to the zero-field spectrum. The only fitting parameter is ξ. From the fit, $\xi = 7.5$ (validating the use of the high-field solution), corresponding to an average dipole moment of $\bar{m} = (3.0 \pm 0.3) \times 10^{-16} A \cdot m^2$.

5.2.4 Relaxation in a magnetic field

We can also determine m by measuring the response of the bacteria to a magnetic field turned on at t=0. Here, the SQUID measures the resultant increase in the net dipole produced by the ensemble as the bacteria align to the external field. The stronger the field, the shorter the time to align. Figure 5.2(b) shows a series of decay curves obtained at different values of magnetic field; the inset shows the inverse of the decay time $1/\tau_{B,||}$ vs. the field B.

As explained in Appendix B, the time dependence of the signal can be approximated by an exponential, with a lifetime $\tau_{B,||}$

$$\langle\Phi(t)\rangle = \mathcal{G}_y^{(r)} L(\xi)\left(1 - e^{-t/\tau_{B,||}}\right) \tag{5.11}$$

For $\xi \gg 1$, $\tau_{B,||} = \tau_o/\xi = \alpha_r/2mB$. Using the value of $\bar{\alpha}_r$ determined above from the time-domain measurements, we find $\bar{m} = (3.0 \pm 0.3) \times 10^{-16} A \cdot m^2$, in good agreement with the value determined from the power spectrum of the noise.

5.2.5 Remaining issues

The previous sections focused exclusively on the dynamical aspects of the data—the knee frequency of the spectra and the decay constants of the response functions. The geometrical factors $\mathcal{G}_{x,y,z}^{(s)}$ (for the spectra) and $\mathcal{G}_y^{(r)}$ (for the response functions) also lead to some insight. Both depend on parameters which are all known or measured: the dipole

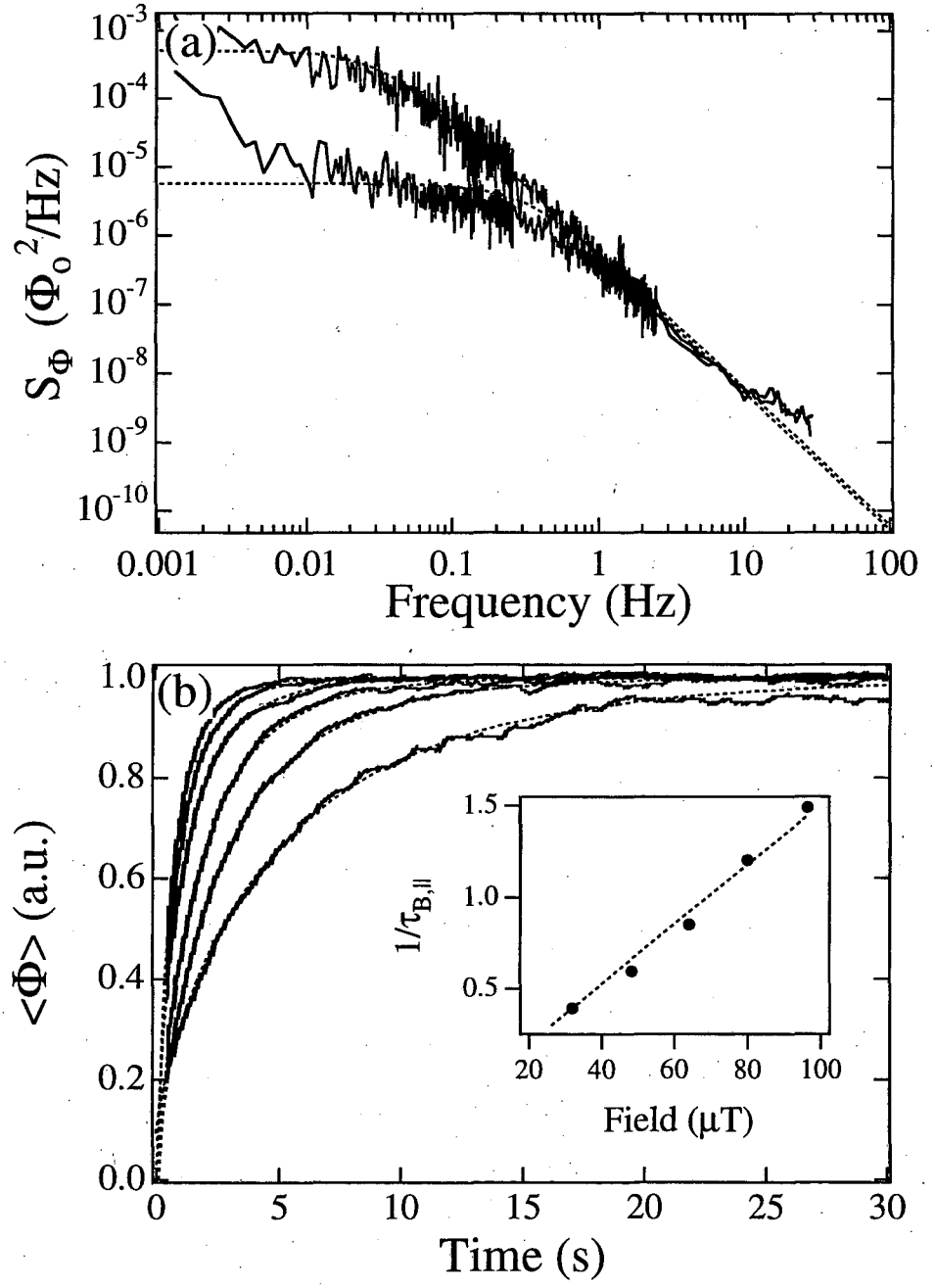

Figure 5.2: Nonmotile bacteria in a magnetic field. (a) Power spectrum of the flux noise from bacteria in a $100\mu T$ field (lower curve). For comparison, the noise in zero magnetic field (upper curve, from Fig. 5.1)(a) is included. (b) Time-varying responses to magnetic fields of various magnitudes turned on at t=0. The bacteria orient along the field, leading to an increasing flux through the SQUID. Fields are $16\mu T$ (lowest curve), $32\mu T$, $48\mu T$, $64\mu T$, $80\mu T$, and $96\mu T$ (uppermost curve). The inset shows the inverse decay times as a function of field.

moment m, the cell density ρ_b (measured using a Petroff-Hausser cell counter), the SQUID-sample separation z_o, and the effective size of the SQUID ℓ_{eff} [see Eqs. (A.9) & (A.10)].

As discussed in Appendix A, the geometrical factors are largely independent of the sample size. This is because the SQUID detects the flux from a volume of space that is smaller than that of the sample. The SQUID used in the measurements described above was a slit A-C type, with $A_{eff} = 0.0129mm^2$ ($\ell_{eff} = 114\mu m$), and the separation between it and the sample was $z_o \approx 50\mu m$. From those parameters, I calculate that 90% of the flux comes from a volume $0.7mm^3$ above the SQUID (95% comes from $6mm^3$). Thus, for a typical cell density $\rho_b = 10^8$cells/mL, the SQUID sampled about 10^5 cells at any particular moment.

In our initial measurements, Tom and I fit the spectra of nonmotile cells to Eq. (5.7) using ρ_b as a fitting parameter. We were surprised to find that the values of ρ_b determined from the fit were over an order of magnitude greater than what we had measured with the Petroff-Hausser counter. However, we soon realized that this was due to settling of the cells to the bottom of the SiN sample well. It is well known that the density of a cell is slightly larger than that of water, so that a nonmotile bacterium will settle out of suspension. The buoyant and drag forces balance so that the mean sedimentation rate $v_d = (\rho_s - \rho)Vg/\alpha_t$ [27], where ρ_s is the cell density or specific gravity, $\rho = 1gm/cm^3$ is that of water, V is the cell volume, $g = 9.8m/s^2$, and α_t is the translational viscous drag coefficient. For a typical cell, $\rho_s \approx 1.05gm/cm^3$, and from our model of the bacteria as cylinders of length $L = 3.5\mu m$ and diameter $d = 0.7\mu m$, $V \approx 1.3\mu m^3$. I estimate $v_d \approx 200\mu m/hr$. Since we often left bacteria in the sample cell for several hours (sometimes overnight) before taking measurements, a significant amount of sedimentation occurred, making the actual cell density near the SQUID much larger than expected.

Later, Helene and I noticed, while making relaxation measurements, that as the bacteria settled over time, the measured relaxation times were getting longer. Figures 5.3(a) & (b) show the increase in the amplitude of the signal and the increase in relaxation time as a function of time. One possible explanation for this behavior is that heavier, larger cells settle to the SiN window faster, biasing the measured relaxation times towards longer times. Another explanation is that as the cell density increases due to settling, magnetic interactions between cells become more important. For a typical cell density $\rho_b = 10^8$ cells/mL, the average distance between cells is $a = (3/4\pi\rho_b)^{1/3} = 13\mu m$. Thus, the average magnetic interaction energy is $\mu_o m^2/4\pi a^3 = \mu_o m^2 \rho_b/3 = 10^{-3} k_B T$, which is negligibly

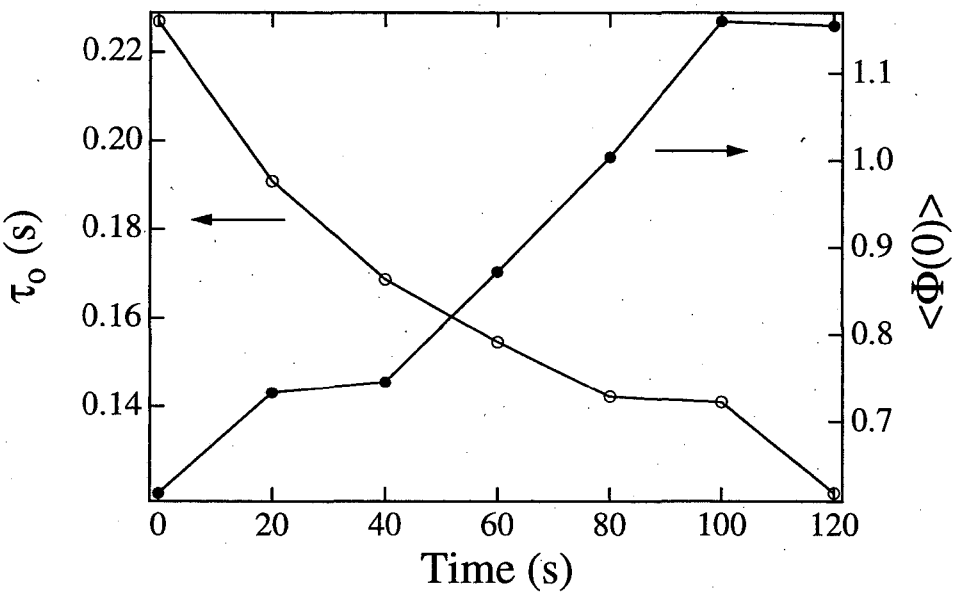

Figure 5.3: Settling of bacteria vs. time. The measured relaxation time decreases as the cells settle (left axis), while the flux increases (right axis).

small. For densities more than an order of magnitude larger, magnetic interactions may become important. It is conceivable that relaxation times would get longer as a result, since a cell would tend to align to the effective field from surrounding bacteria.

Regardless, to prevent settling of the bacteria, the sample was agitated between averages by bubbling air into the cell suspension with a small plastic tube. In this way, we were able to minimize drifts in the relaxation times. The data in Figs. 5.1(a) & (b) and 5.2(a) & (b) were obtained in this manner. The fits to the spectra yield a value of $\mathcal{G}^{(s)} = 1.53 \times 10^{-4} \Phi_o^2$ corresponding to a density of $\rho_b = 1.8 \times 10^8$cells/mL, in fair agreement with a value of $\rho_b = (9.6 \pm 0.6) \times 10^7$cells/mL measured with a cell counter.

5.3 Motile bacteria

5.3.1 Low-frequency dynamics

Motile *M. magnetotacticum* exhibit very different dynamics, as illustrated in Fig. 5.4 for zero applied magnetic field. Compared with the spectrum in Fig. 5.1(a), there are three distinct differences: the knee frequency, $1/2\pi\tau_m$, is larger by a factor of 4, the power spectrum falls off as $1/f^\nu$ with $\nu \approx 2.4$ rather than $1/f^2$, and there are two peaks, at 63 Hz and 26 Hz. The differences in spectra are clearly due to the different dynamics of motile bacteria. If iodine is added to the sample to kill the bacteria, the spectra resort to the Lorentzian described in Section 5.2.

At low frequencies the data can be fitted quite well to a modified Lorentzian of the form:

$$S_\Phi(f) \propto \frac{1}{1 + (2\pi|f|\tau_m)^{2.4}} \tag{5.12}$$

with $\tau_m = 1.2s$. The change in knee frequency is unlikely to be due to a change in rotational diffusion time, since *M. magnetotacticum*, which are not run-and-tumble microorganisms like *E. coli*, cannot actively control their orientation. They are, however, motile, which means that we cannot ignore translations as we did for nonmotile cells. Swimming speeds of *M. magnetotacticum* as fast as $100\mu m/s$ (more than 20 times the cell's length per second!) have been measured [24]. At such speeds, the bacteria can cross the length of the SQUID in a time $\lesssim 1s$ several times faster than the rotational diffusion time. The fact that the cells' orientations diffuse as they swim also leads to translational diffusion, given by $D_t = v^2/6D_r$ [27]. For $v = 100\mu m/s$ and $D_r = 0.1s^{-1}$ as measured above, is $D_t = 1.6 \times 10^4 \mu m^2/s$, in

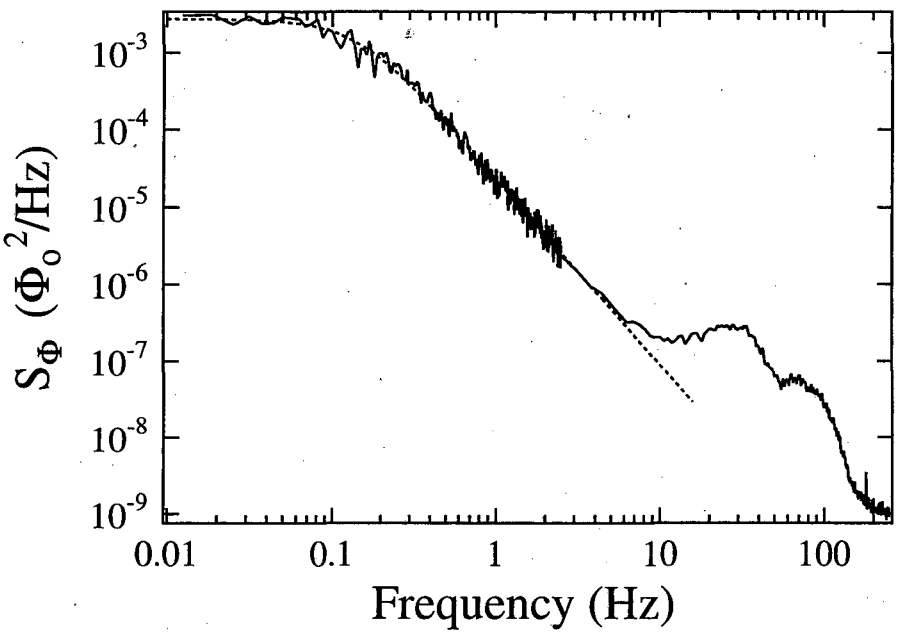

Figure 5.4: Motile bacteria. Power spectrum of the noise produced by the random motility of the bacteria in zero magnetic field (0.01-10Hz), and vibration (26Hz) and body roll (63Hz) of the cells due to flagellar rotation. The SQUID used in these measurements was a hole L2 type (see Table 2.1), 25μm below the vacuum window.

sharp contrast to that determined for nonmotile cells. A bacterium can diffuse the length of the SQUID in a time $\lesssim 1s$.

A proof that the noise spectra at low frequencies are due to translational—not rotational—motion is shown in Fig. 5.5. The plot is a composite of data sets taken with two different SQUIDs, a hole L2 type and slit A-C type, with different geometries and effective areas (see Table 2.1). The knee frequencies are clearly different in the two sets of data. If the spectra had been produced by rotational motion, the knee frequencies would have been the same, independent of SQUID geometry.

In Appendix C, I demonstrate that the autocorrelation function for translational motion is approximately exponential. The decay time τ_m corresponds to the time to swim across a characteristic length ℓ_c related to the effective size of the SQUID ℓ_{eff} and the minimum separation z_o; in other words $\tau_m = \ell_c/v$. Helene performed computer simulations of the random motility of bacteria, and found very similar results. For small values of the separation z_o, ℓ_c is proportional to ℓ_{eff}.

As shown in Fig. 5.5, the data taken with the slit A-C SQUID appears to have two knees in it. The data was fitted with two modified Lorentzians of the form Eq. (5.12), with times $\tau_{m,1} = 4.9s$ and $\tau_{m,2} = 0.6s$. Again, the SQUID geometry may be responsible for these features. Up until now, I have treated all SQUIDs as square pickup loops of side $\ell_{eff} = (A_{eff})^{1/2}$. While this may work for a hole L2 type SQUID, it is conceivable that a slit A-C type SQUID may be more accurately modeled as a rectangular loop, with *two* characteristic lengths, leading to two knees. Since the area of the loop must equal the effective area of the SQUID, and expecting $\tau_m \propto \ell_{eff}$ for small z_o, one would naively expect the ratio of the characteristic times for the two data sets to equal the ratio of the effective areas of the two SQUIDs (assuming the cell velocities are the same between measurements). However, I calculate $\tau_{m,1}\tau_{m,2}/\tau_m^2 \approx 2$ and $A_{eff}^{(A-C)}/A_{eff}^{(L2)} \approx 8$. Further investigation is needed.

More problematic, however, is explaining the exponent $\nu = 2.4$ in the fall-off of the spectra. The model described so far generates a Lorentzian: $\nu = 2$. As explained above, a distribution in decay times in the autocorrelation function can only lead to exponents $\nu < 2$. Explaining a *steeper* fall-off is much more difficult. One intriguing possibility is that the random motility of the bacteria cannot be described by a standard random walk. One special class of random walk, the Lévy walk [47, 48], is characterized by long-range correlations. One consequence is that the root mean square of the displacement

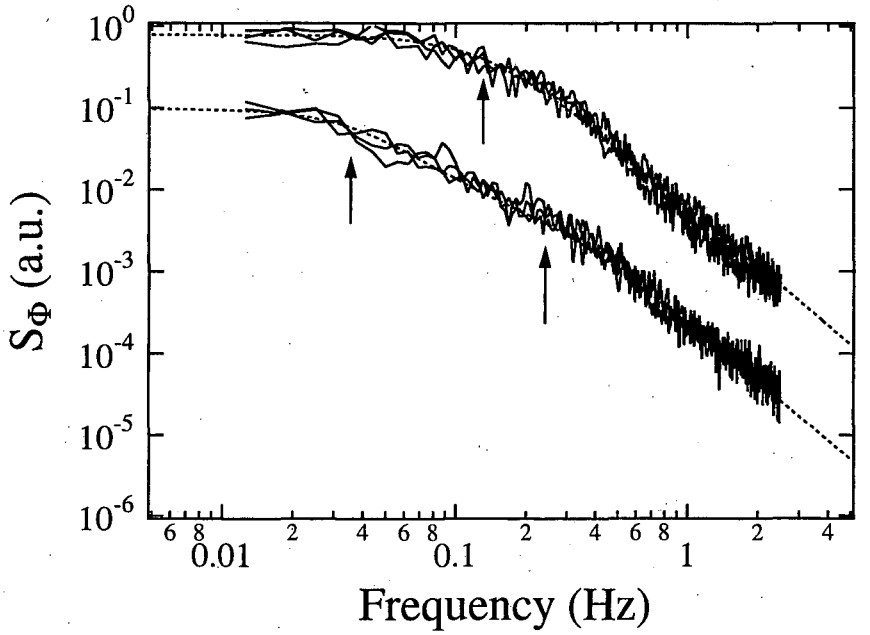

Figure 5.5: Low frequency part of the spectrum. The two curves are composite data sets taken with two different SQUIDs; a hole L2 SQUID, $25\mu m$ away in the top curve, and a slit A-C SQUID, $50\mu m$ away in the bottom curve. In the top curve, a single modified Lorentzian (shown in dotted line) with characteristic time $\tau_m = 1.2s$ (indicated by the arrow) fits the data. In the bottom curve, two modified Lorentzians with times $\tau_{m,1} = 4.9s$ and $\tau_{m,2} = 0.6s$ fit the data.

$x_{rms} \equiv \sqrt{\langle \Delta x^2 \rangle} \sim t^{\alpha}$, with $\alpha > 1/2$, a phenomenon called anomalous diffusion. Recent evidence indicates that this type of random walk may be prevalent in biological systems, particularly in foraging organisms [48]. In our experiment, anomalous diffusion $x_{rms} \sim t^{\alpha}$ would lead to an autocorrelation function of the form $\exp(-(|t|/\tau_m)^{2\alpha})$, which would lead to a power spectrum that falls off as $1/f^{2\alpha+1}$. Equating $\nu = 2\alpha + 1$, $\alpha > 1/2$ would indeed lead to $\nu > 2$. While this is an interesting hypothesis, there may be other, more plausible explanations, and clearly more experiments are needed to elucidate this matter.

5.3.2 High-frequency dynamics

The peaks at 26Hz and 63Hz in Fig. 5.4 have an interesting interpretation. Rotational and translational diffusion, and the random motility of the bacteria, as explained above, are clearly much too slow to explain these features. The only known dynamics of motile cells in that frequency range is the rotation of the flagellar motor, which can be as fast as 100Hz in *E. coli* [49]. In Fig. 5.6, a sample of bacteria is exposed to lethal levels of oxygen. There I show three spectra of the same sample at different times (curves *a* at t=0, *b* at 15min., and *c* at 75min., offset for clarity). Atmospheric levels of oxygen contaminate the medium, causing the microaerobic cells to slow over time. As a result, the peaks in Fig. 5.6 move to lower frequencies. Note that the two peaks move together—the ratios of the frequencies and the amplitudes remain constant—indicating that they must be coupled and that they must be produced by the same source, which must be connected to the swimming speed of the cells. The speed of a bacterium is proportional to the rotation rate of its flagellar motor [50].

Lowe *et al.* [50] observed similar peaks for *Streptococcus* optically by measuring the noise from a photocathode onto which images of the cells were projected. They attributed the two peaks to vibrations and rotations of the cell caused by its flagellum. If the length of a flagellum is not an integer number of wavelengths, an imbalance force perpendicular to the rotation axis causes the body to vibrate at the same frequency [27]. In addition, the rotating flagellum applies a torque to the body, which responds by counter-rotating. Because the cell body experiences a higher drag than the flagellum, this counter-rotation occurs at a lower frequency than the flagellar rotation. If the axes of the body and flagellum are not collinear, the cell precesses (or rolls) [50]. These two coupled modes are responsible for the peaks at 63 Hz and 26 Hz in the spectrum in Fig. 5.4.

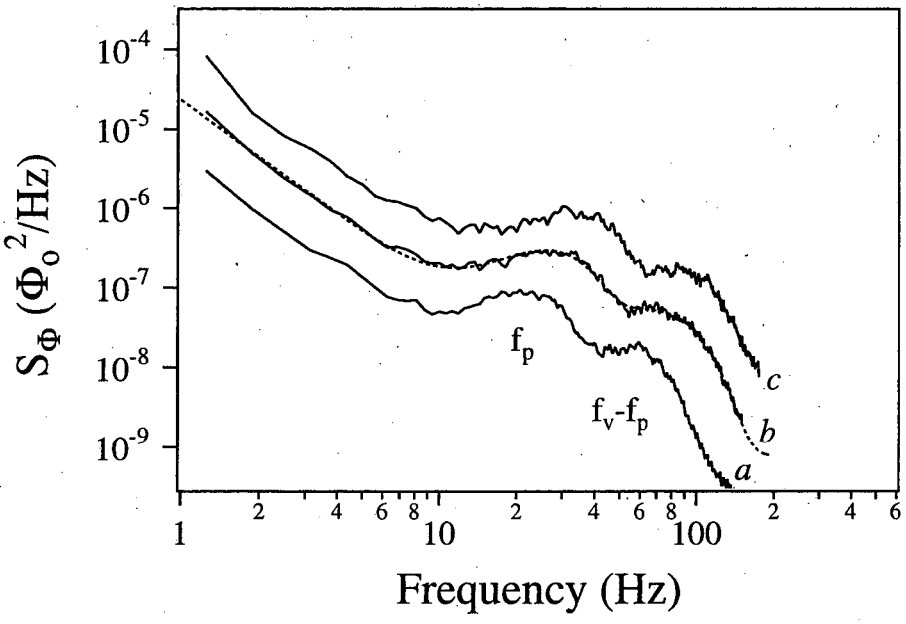

Figure 5.6: High frequency peaks. The presence of high levels of oxygen causes the ensemble to slow over time. The peaks shift to lower frequencies (curve *a* at t=0, *b* at 15min., and *c* at 75min., offset for clarity). However, the amplitudes and ratios of frequencies remain constant. The central curve is fitted (dotted line). Gaussian distributions of frequencies account for the widths of the peaks.

From the magnitudes of the peaks it is possible to estimate the amplitudes of these modes. As a simple model, we assume that the magnetic dipole moment rotates about vibrational and precessional axes with angular amplitudes ϕ_v and ϕ_p and frequencies f_v and $-f_p$, respectively (Fig. 5.7). Physically, f_v is the rotation rate of the flagellum in the frame of the bacterium; because of the counter-rotation of the body, one measures $f_v - f_p$ in the laboratory frame. Provided the angular amplitudes are small, the model reproduces the two peaks in the spectrum, with f_p=26 Hz and $f_v - f_p$=63 Hz. The widths of the peaks, due to variations in the population, are modeled by a Gaussian distribution of frequencies of width $\Delta_{v,p}$. The peak heights determine the angular amplitudes. A detailed calculation (see Appendix C) shows that it is not necessary to know the number or position of the bacteria contributing to each peak. Rather, ϕ_v and ϕ_p are determined entirely from the ratio of the spectral density at each peak at frequency $\bar{f}$ to that at low frequencies:

$$\phi^2 \approx 2\sqrt{2\pi\nu}\sin\frac{\pi}{\nu}\,\tau_m\Delta\cdot\frac{S_\Phi(\bar{f})}{S_\Phi(0)} \tag{5.13}$$

The fit of each peak to a Gaussian distribution is excellent (Fig. 5.6). The fitting parameters for curve b are: $\bar{f}_v = 89.2 \pm 9.6$ Hz, $\Delta_v = 29.5 \pm 7.9$ Hz, and $\phi_v = 5.5 \pm 0.7°$ for the vibration, $\bar{f}_p = 25.9 \pm 0.2$ Hz, $\Delta_p = 10.4 \pm 0.8$ Hz, and $\phi_p = 7.0 \pm 0.4°$ for the precession. Error bars are estimated from random errors in the least squares fitting routine and systematic fitting errors. At the highest frequencies (>150Hz), the signal is comparable to the SQUID noise, distorting the measured spectrum. As a result, we cut the data off at some suitable frequency; however, the choice for this cutoff can systematically affect the fit. We have taken account of this effect in the error bars. Table 5.1 summarizes the results from the analyses of the three curves in Fig. 5.6. As stated above, the ratio of the peak frequencies $\bar{f}_v/\bar{f}_p$ and the peak amplitudes ϕ_p and ϕ_v are constant to within the error bars.

5.3.3 Migration in a magnetic field

In the presence of a static, uniform magnetic field comparable to that of the Earth, the bacteria undergo magnetotaxis. In Fig. 5.8(a) we apply a $37\mu T$ field parallel to the SQUID plane at $t = 0$. The noise at all frequencies decreases as a function of time. Figure 5.8(b) plots the decay in the amplitude of the precessional peak (at $\sim$ 26Hz) against time; for large times the signal fits well to an exponential with characteristic time $\sim 200s$. The

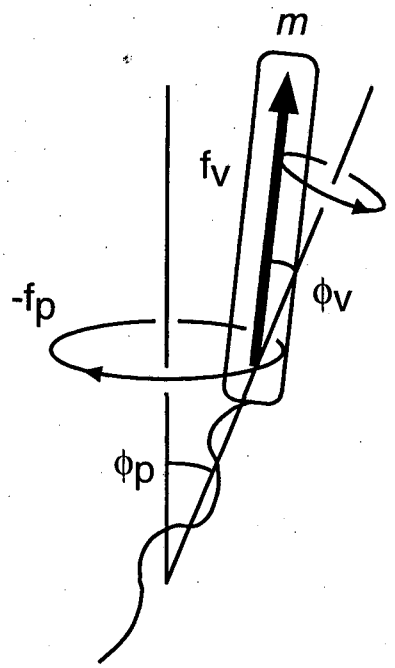

Figure 5.7: Model of precession and vibration of a magnetotactic cell. The vibration and body roll of a cell are modelled as rotations of the magnetic dipole moment m about two axes with angular amplitudes ϕ_v and ϕ_p and frequencies f_v and $-f_p$ (inset). Peaks in the spectrum appear at f_p and $f_v - f_p$.

process is reversible; when the applied field is turned off, the magnitude of the noise regains its original value. The observed decay occurs over much too long a time scale ($200s$) to be due to the alignment of the bacteria with the applied field (about $2s$, for a $37\mu T$ field). However, this time scale is consistent with the bacteria traversing the sample cell ($13mm$), given a swimming speed of $\sim 100\mu m/s$. Moreover, the noise at *all* frequencies is affected. Since the entire spectrum is proportional to the number N of bacteria detected by the SQUID, the signal indicates that the number of cells above the SQUID decreases with time.

Spormann and Wolfe [51] have observed that *M. magnetospirillum*, a bipolar magnetotactic bacteria, will tend to swim toward the north or south poles of a static magnetic field. This creates regions of high cell density near the poles, and low density in the center of the sample. We seem to observe similar behavior in our experiment. The cells in Fig. 5.8(a) are swimming away from the SQUID, which is in the center of the liquid sample cell, toward the edges. Thus, the cell density over the SQUID decreases over time. A simple model to describe this behavior is to assume that half the cells swim toward one pole at a drift velocity v_d while the other half swim toward the other pole at a velocity $-v_d$. Following the results of Kalmijn [30], one expects the drift velocity to be proportional to the Langevin function, $v_d = vL(\xi)$. The diffusion equation for this model is trivial to write down

$$\frac{\partial P_\pm}{\partial t} = D_t \frac{\partial^2 P_\pm}{\partial y^2} \pm v_d \frac{\partial P_\pm}{\partial y}, \tag{5.14}$$

the sign depending on whether the bacterium is north- or south-seeking. $P_\pm$ denotes the probability density for each type of bacterium. In this model, cells are not allowed to change swimming directions.

It is possible to solve this equation analytically. In an infinite sample, the Green's function for Eq. (5.14) is simply a Gaussian with a width $2D_t t$ and a peak moving at speed v_d. In a finite sample, boundary conditions must be implemented at the edges $-a/2$ and $a/2$, where $a = 13mm$ is the size of the sample cell. The solution is tedious and will not be included here (a solution to a similar problem is given in [52]). However, a lot of the behavior can be deduced from intuition. For an infinite sample, the continuity equation tells us that a constant flow of cells will not change the average density over the SQUID, so that one would not expect a decrease in signal. For a finite sample, this remains true roughly until bacteria at one end of the sample cell have migrated past the SQUID in the center, a time $\sim a/2v_d$. Past that point the cell density over the SQUID must decrease

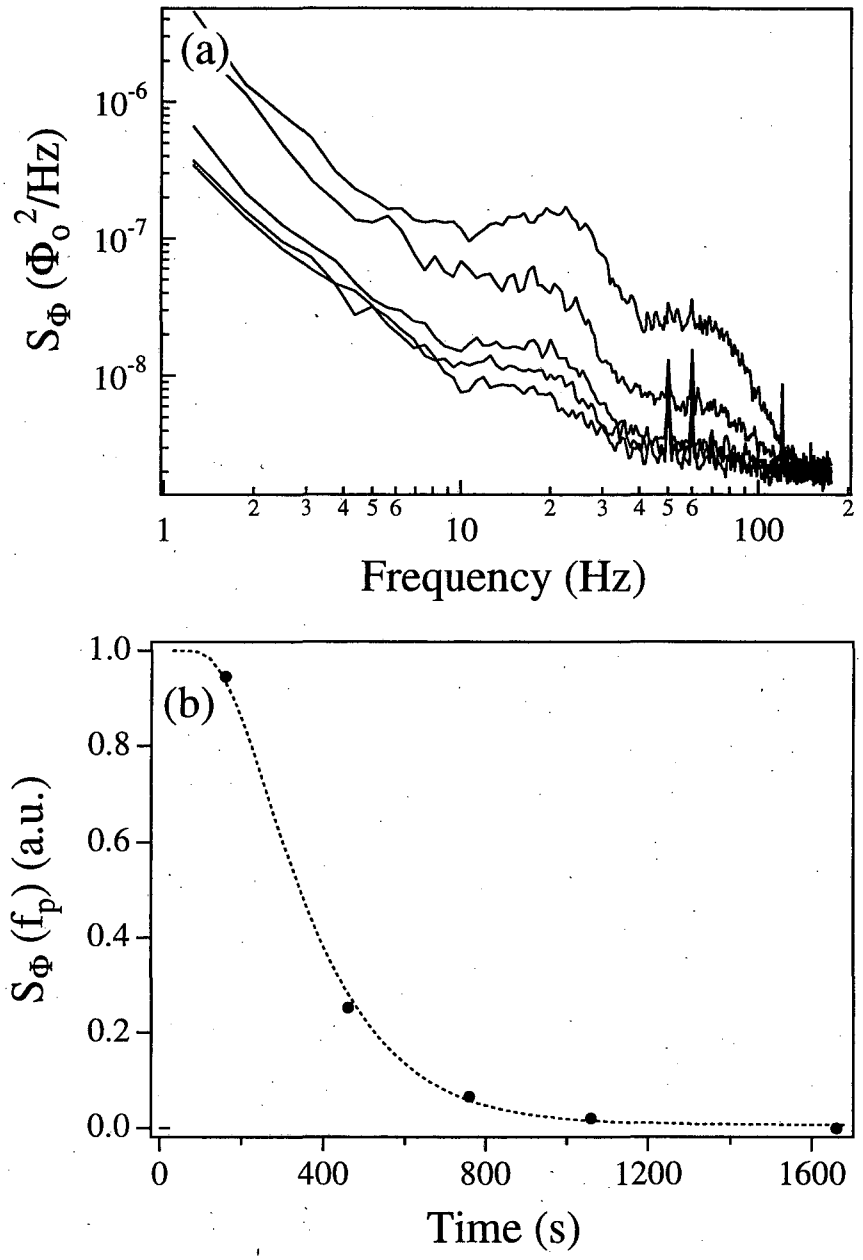

Figure 5.8: Motile bacteria in a uniform $37\mu T$ field. (a) The noise at all frequencies decreases as a function of time. The top spectrum is taken as the field is turned on at t=0; the subsequent curves are measured at t=5 min, 10 min, 15 min, and finally 25 min. The behavior is reversed if the field is turned off. The noise above $\sim$ 100 Hz is from the SQUID sensor. (b) The magnitude of the noise at the peak frequency f_p is plotted against time. For large times, the decay fits to an exponential with time constant $\tau \approx 200$ sec. The vibration and precession of the cells are not affected by the magnetic field.

until it reaches an equilibrium. The equilibrium density $P = P_+ + P_-$ is easily solved from Eq. (5.14), setting the right-hand side to zero:

$$P_{eq}(y) = \frac{v_d}{2D_t} \frac{\cosh(v_d y/D_t)}{\sinh(v_d a/2D_t)} \tag{5.15}$$

which reduces to $1/a$ as v_d goes to zero. P_{eq} is normalized such that $\int_{-a/2}^{a/2} dy P_{eq}(y) = 1$. At the SQUID, where $y = 0$, the density can be exponentially small if the applied field is large. In Fig. 5.8(b), I fitted the data to a solution of Eq. (5.14) with $v_d = 20\mu m/s$ and $D_t = 1.6 \times 10^4 \mu m^2/s$, both reasonable values. Note that the curve is flat for times below $\sim 100s$.

To test this model further, I attempted to measure the migration rates of the bacteria as a function of applied magnetic field. Unfortunately, at high magnetic fields the noise dropped precipitously in a time faster than that needed to obtain a spectrum so that I was unable to obtain enough data points for a proper fit. At low fields, the decrease in cell density over the SQUID was minimal [as can be seen in Eq. (5.15) for low v_d], and difficult to quantify accurately. Qualitatively, though, the field does appear to affect the migration rate.

Whereas the low-frequency (long-time) behavior is clearly affected in a magnetic field, the high-frequency dynamics are not. The presence of the magnetic field does not seem to affect the vibrational and rotational modes of the bacteria, or the flagellar rotation rate. Indeed, since the coupling torque of the flagellar motor, which is $3 \times 10^{-18} N \cdot m$ for *E. coli* but presumably similar for *M. magnetospirillum*, is much larger than the torque from the magnetic field, $10^{-20} N \cdot m$, this is not unexpected. The ratio of the amplitudes and frequencies of the peaks in Fig. 5.8(a) is the same as in zero magnetic field.

5.4 Observations of a single bacterium

Figures 5.9(a)-(d) display several time traces obtained from motile cells in a zero magnetic field. The SQUID-window separation was $15\mu m$ in these data, and the SQUID was a hole-L2 type (see Table 2.1). The upper trace in Fig. 5.9(a) is representative of most observations and consists of contributions from many bacteria. The lower trace in Fig. 5.9(a) and the traces in (b)-(d), which we obtain only on occasion, are dominated by a large, oscillatory signal. From the measured value of the dipole moment m and Eq. (3.5),

the amplitude of the signal is consistent with that of a single magnetotactic bacterium swimming a distance $\sim 18\mu m$ away from the SQUID.

The oscillations in Fig. 5.9(a)-(d) are most likely produced by a single bacterium swimming parallel to the silicon nitride vacuum window in a circular "orbit". It is known that near surfaces—such as glass slides or capillaries—a microorganism will tend to swim in circles parallel to the surface. Frymier *et al.* [53] have extensively studied such behavior in *E. coli* with a tracking optical microscope. Mike Adamkiewicz and I observed such orbits for *M. magnetotacticum* under an optical microscope. Figures 5.10(a)-(c) show slow-speed video stills of such events. The period of the orbits, as observed by video, are consistent with the oscillation frequency in Figs. 5.9.

In calculations of the hydrodynamic interactions between microorganisms and surfaces, Ramia *et al.* [54] have shown that a surface causes an asymmetry in the propulsive force of the cell, causing it to drift persistently in a direction perpendicular to its body [see Fig. 5.10(d)]. As a result the cell swims in a circular "orbit" parallel to the plane of the surface. The effect of the surface is only significant if the separation between it and the cell is smaller than the physical dimension of the cell. In their studies of *E. coli* orbits, Frymier *et al.* [53] estimated a separation $< 2\mu m$. The sense of rotation is determined by the direction of flagellar rotation (always counterclockwise, as viewed from behind the cell) and the location of the surface relative to the cell. If the surface is below, the cell drifts to its right and swims in a clockwise circle (as viewed from above); if the surface is above, the drift is to the left and the orbit is counterclockwise.

Bacteria are observed to maintain orbits for long times[3], $\sim$10-100s. In that time, however, we would expect the cell to diffuse away from the surface, ending its orbits prematurely. Some mechanism constraining the bacterium near the surface must exist. Frymier *et al.* [53] have proposed that an attractive interaction between bacteria and surfaces, due to a combination of electrostatic and van der Waals forces, may maintain the cell's position close to the surface for extended periods.

Thus, the oscillatory signals in Figs. 5.9(a)-(d) are entirely consistent with a single bacterium swimming in an orbit very close to the silicon nitride vacuum window of the microscope, directly above the SQUID. I suspect the rotation of the cell's dipole moment during the orbit is mainly responsible for the signals, although, if the orbit is large enough,

[3]Interestingly, this is not true for cells which run-and-tumble, like *E. coli*, which often leave the surface after tumbling [53]

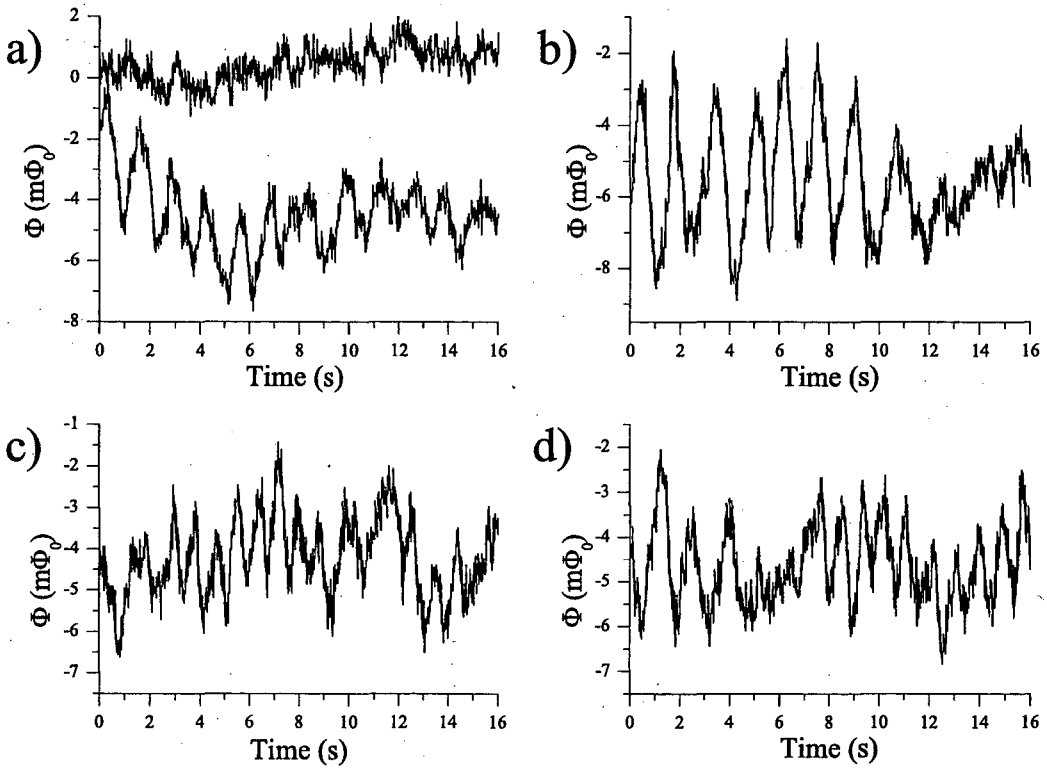

Figure 5.9: Single bacterium orbit. Typically, the field detected by the SQUID consists of small signals from many bacteria [upper curve in (a), offset for clarity]. Occasionally, a single bacterium swims in a circular orbit parallel to the silicon nitride membrane, causing large oscillations [lower curve in (a) and (b)-(d)]. We observe these events only when the surface of the membrane is clean and the SQUID is positioned very close ($\sim 15\mu m$) to it.

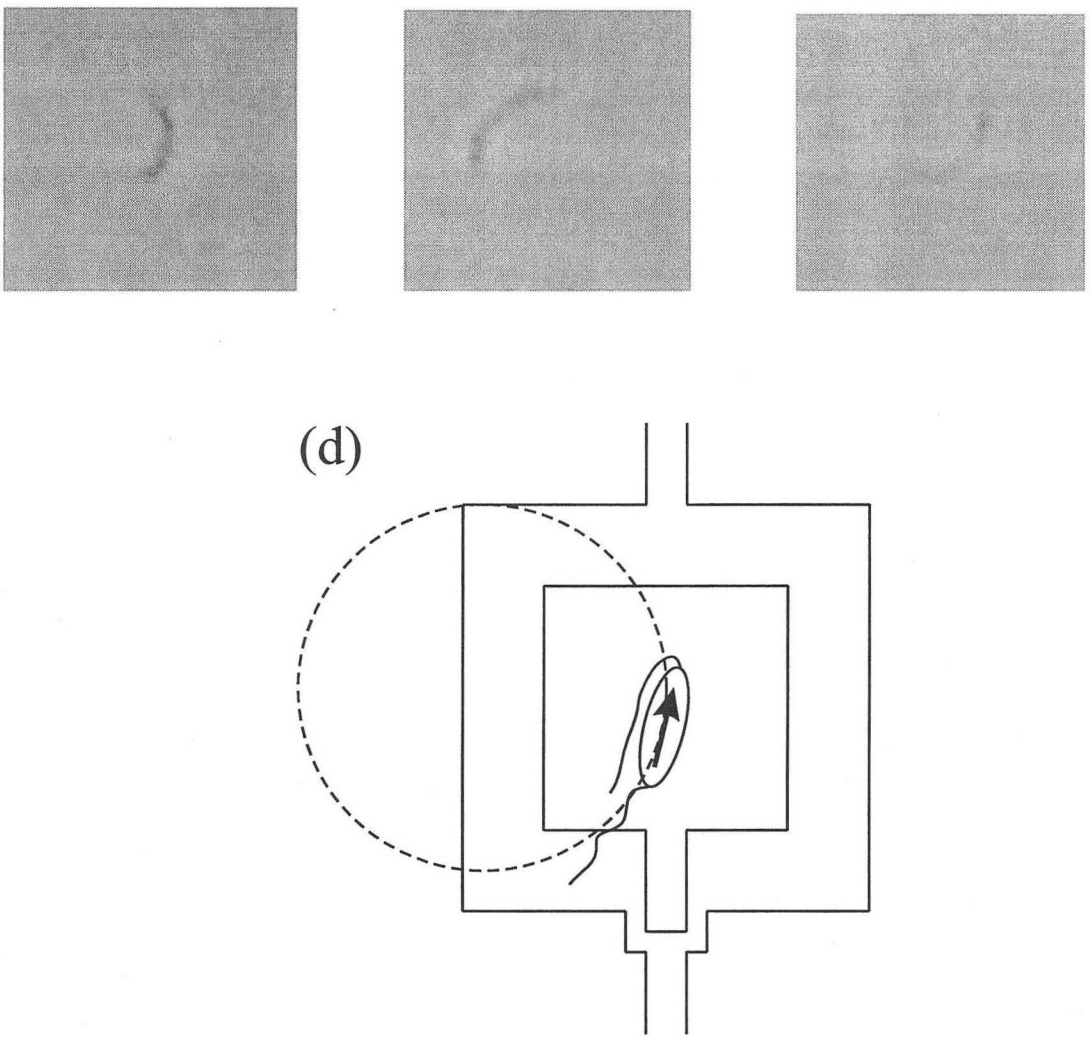

Figure 5.10: Slow-speed video stills (a)-(c) of bacterial orbits. The orbit diameters are comparable to the bacteria length. (d) Schematic of bacterial orbit with SQUID (not to scale).

its translation across the SQUID loop may also contribute. Ideally, we would have preferred to make optical observations of the bacteria in the sample well of the SQUID microscope concurrently with SQUID measurements. Unfortunately, the system configuration at the time did not allow us to do so. However, we have never observed these oscillations in the absence of bacteria, ruling out environmental noise as a cause. Furthermore, we have never seen oscillations with nonmotile bacteria. Interestingly, we noticed that after several experiments, cellular debris would accumulate on the SiN window and we would cease to observe oscillations [17]. Presumably, the debris disrupts the surface-cell interactions and renders orbits impossible.

These observations are an experimental verification of Eq. (3.5) discussed in Section 3.3.1 and a demonstration of the sensitivity of the SQUID microscope. The hole-L2 type SQUID ($\ell_{eff} = 40\mu m$), positioned $15\mu m$ away, can detect a single magnetotactic bacterium and the data indicate that there is ample signal to noise. The rms noise, which we estimate by integrating the SQUID noise over the bandwidth of the traces (62.5mHz to 25Hz), is roughly $120\mu\Phi_o$ corresponding to $1.5\times10^{-17}A\cdot m^2$ via Eq. (3.5). Given $m \approx 3\times10^{-16}A\cdot m^2$, this indicates a signal-to-noise ratio of ~ 20, which is consistent with Fig. 5.9(a)-(d). Since each bacteria contains a chain of 20 or so magnetosomes, the SQUID microscope should, in principle, be able to detect one, single-domain $35nm$-diameter magnetite nanoparticle.

	Curve a	Curve b	Curve c
$\bar{f}_p$ (Hz)	31.1 ± 0.2	25.9 ± 0.2	20.7 ± 0.2
$\bar{f}_v$ (Hz)	114.2 ± 12.3	89.2 ± 9.6	74.2 ± 8.0
$\bar{f}_v/\bar{f}_p$	3.7 ± 0.4	3.4 ± 0.4	3.6 ± 0.4
ϕ_p (°)	6.7 ± 0.4	7.0 ± 0.4	7.0 ± 0.4
ϕ_v (°)	4.6 ± 0.6	5.5 ± 0.7	5.2 ± 0.7

Table 5.1: Peak frequencies and amplitudes for bacteria in oxygen.

Part II

Magnetic Immunoassay

Chapter 6

Magnetic Labeling of Biological Substances

6.1 Introduction

The experiments on magnetotactic bacteria described in Part I demonstrate the ability of the SQUID microscope to detect and characterize magnetic biological samples. The above technique can certainly be extended to microorganisms or biological substances that, like magnetotactic bacteria, are intrinsically magnetic. However, more interesting would be the extension of the range of application of the microscope to non-magnetic biological samples, by devising ways of "magnetizing" them, for example by attaching a magnetic label or tag.

The magnetic labeling of biological substances is not a new idea; it is already established as a powerful and versatile diagnostic tool in biology and medicine. Magnetic particles ranging in size from ten nanometers to several microns can be synthesized in a laboratory, bound to a suitable antibody, and used to label specific molecules, structures or microorganisms [55]. Established techniques such as magnetic cell separation use magnetic field gradients to manipulate and isolate magnetically labeled cells [56]. However, very few of these techniques actually detect the magnetic fields from the magnetic labels directly.

The extraordinary sensitivity of the SQUID microscope, as evidenced by the detection of a single magnetotactic bacterium, suggests that it could be used as a very sensitive detector of magnetically labeled substances. As explained in Section 3.3.1, the microscope

could in principle detect one single-domain 35-*nm* magnetite label. Such sensitivity would match that of the most sensitive optical labeling techniques, which can now detect the light emitted by a single fluorescent dye molecule.

In the remainder of Part II, I will discuss experiments in magnetic labeling of biological substances, using the SQUID microscope as a sensitive detector. Based on a novel concept developed by Weitschies *et al.* [57], we have developed a magnetic immunoassay which detects minute amounts of targeted biological substances. Remarkably, this method already has a sensitivity which surpasses that of standard techniques, and with the improvements outlined in the next chapter, may achieve even higher sensitivities.

6.2 The immunoassay

In biology and medicine, it is often necessary to detect small amounts of a specific biological substance. For instance, a biologist may wish to isolate a particular protein from a large array of other biomolecules, while a doctor may wish to detect small numbers of a specific pathogen—*E. coli* for example—from a patient's blood. In each case, an assay must be developed to selectively and sensitively detect the desired target. One very common approach is to utilize antibodies produced by the immune system in response to foreign substances—macromolecules or cells. An "immunoassay" uses the extraordinary specificity of an antibody to its target antigen to detect and quantify minute amounts of that antigen.

Antibodies form a diverse but related family of proteins called immunoglobulins. They consist of two identical subunits arranged in the shape of a Y. The amino acid sequences of antibodies contain regions that are largely preserved between antibodies and other regions that are highly variable. The latter, located in the arms of the Y, are responsible for the specific recognition of different antigens. The association of the antibody to the antigen involves van der Waals forces, hydrophobic interactions, hydrogen bonding, and ionic interactions. The specificity and strength of the association stems from the complementarity of structure between the antibody and the antigen [58]. In the case of a pathogen like *E. coli*, the body produces an antibody which specifically binds to an epitope, a unique surface feature located on the outer membrane of the microorganism.

In an immunoassay, the antibody is detected by labeling it with a suitable substance, in many cases a radioactive or fluorescent molecule or particle. Alternatively, an antibody can be linked to an enzyme which catalyzes a chemical reaction which can be

observed. In the standard method called Enzyme-Linked ImmunoSorbent Assay or ELISA, this latter technique is used. As shown in Figure 6.1, in ELISA, a surface is coated with an antibody (called a capture antibody) specific to the target substance. When a sample is added, the targets bind to the antibody and become immobilized on the surface. A second antibody (also specific to the target, but binding to a different site), is added and binds to the target. This antibody is conjugated with an enzyme which can change the color of a chemical substrate added at the very end. One detects the change in color due to the presence of the second antibody.

The use of an immunoassay in the detection of a substance depends on the quality of the antibody developed against the desired target. An antibody must bind strongly and specifically to a target, and must not cross-react with other substances present in the sample. As should be clear from the above description, the presence of the target is implied only from the detection of the second antibody. Thus, special care must be taken to wash away any antibodies that are not bound to their target. Since in general, only a small fraction of the antibodies actually bind, this can be difficult. In general, there is always a small portion of antibodies not bound to targets or bound nonspecifically to the surface which generates a background signal.

6.3 Magnetic immunoassays

6.3.1 Limitations of standard techniques

ELISA's can be quite sensitive, the best ones able to detect as few as 10^5 labeled antibodies. In the case of bacterial antigens, it is possible to amplify the signal by culturing the sample to grow colonies. This procedure is very common in certain sectors such as the food industry, in screening for food-borne pathogens. Assay sensitivities are greatly enhanced by this method, since in principle only one living cell is necessary to start a colony. Unfortunately, it can be prohibitively time-consuming, as culturing must take at least one or two days to generate populations large enough to be detectable. In some applications—again, the food industry—speed is of paramount importance. There is an ever-growing need for new, faster, and more sensitive techniques for the detection of pathogens [59].

Recently, magnetic immunoassay techniques have been developed in which the magnetic field generated by the magnetically labeled targets is detected directly with a

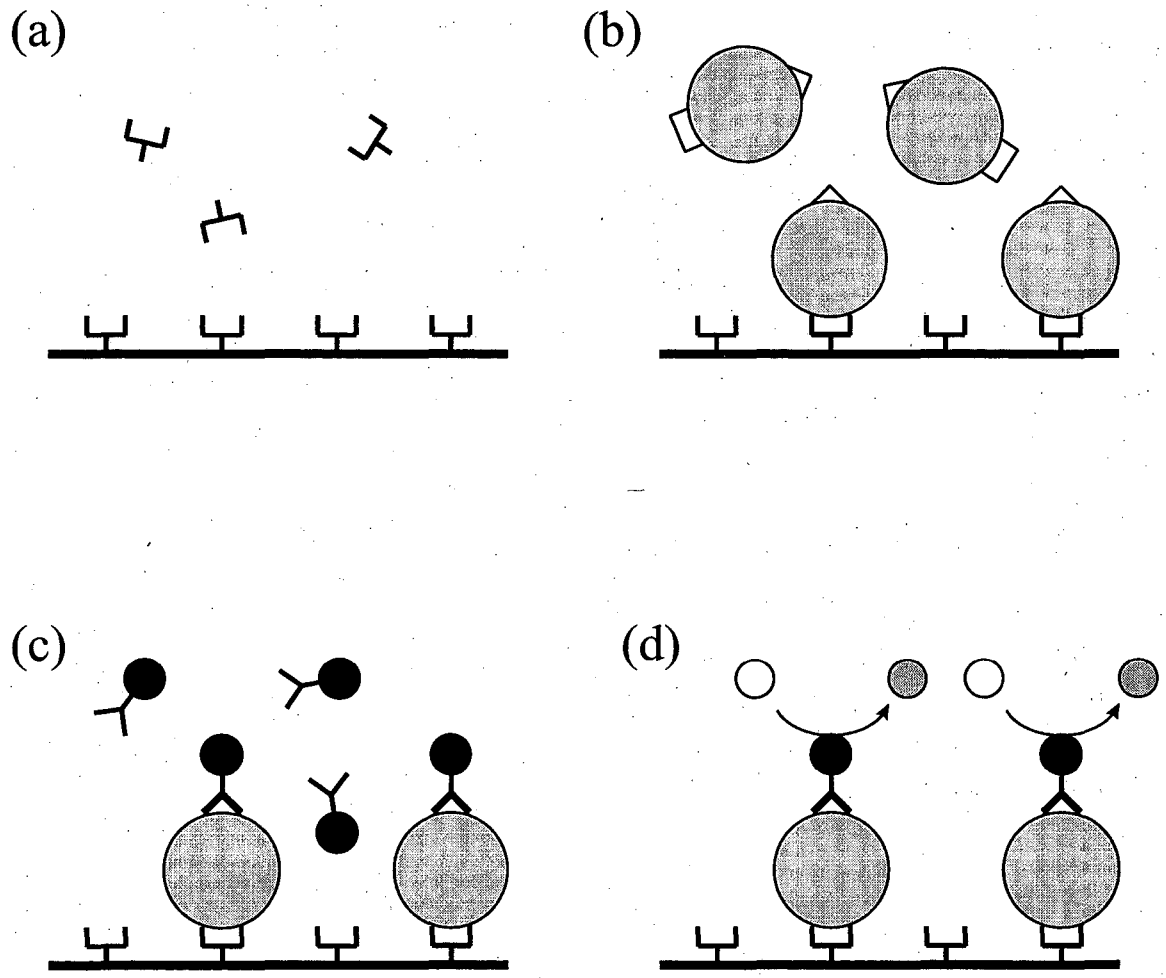

Figure 6.1: Enzyme-Linked ImmunoSorbent Assay (ELISA). (a) A surface is coated with a capture antibody. (b) The sample is added and the target molecules or cells bind to the antibody. (c) A second antibody, linked to an enzyme, is added and binds to the targets. (d) The enzyme produces a color change with the addition of a chemical substrate. In between each step, a wash is necessary to remove unbound fractions.

sensitive magnetometer [57, 60]. Weitschies *et al.* [57] have proposed a novel MAgnetic Relaxation/remanence ImmunoAssay (MARIA) using a SQUID as a magnetic field sensor. In this technique, an immobilized target is immersed in a suspension of superparamagnetic nanoparticles bound to antibodies specific to that target. A pulsed external magnetic field is applied to align the dipole moments of the particles. The SQUID detects the magnetic field from the particles bound to the target.

The basis for the assay is the nature of the relaxation of the particles after magnetization. In contrast to ferro- or ferrimagnetic particles, superparamagnetic particles do not possess a permanent magnetic dipole moment. Rather, their dipole moments may spontaneously rotate towards an "easy direction" by a process called Néel relaxation, which I will explain in the following section.

6.3.2 Néel relaxation

Magnetism is caused by exchange interactions between electronic spins. Depending on the sign of the interaction, neighboring spins either align parallel (ferromagnetism) or antiparallel (antiferromagnetism); in ferrimagnetic particles, like magnetite (Fe_3O_4), both types of interactions add up to a net parallel alignment. This ordering of spins leads to a net dipole moment in ferro- and ferrimagnetics, the direction of which is determined by the crystallographic symmetry of the material. In uniaxial materials, one direction $\hat{\mathbf{n}}$ is singled out. The energy associated with this preferred direction of alignment, called the anisotropy energy, is of the form [61]

$$E_a = -KV\left(\frac{\mathbf{m}\cdot\hat{\mathbf{n}}}{m}\right)^2 = -KV\cos^2\theta. \tag{6.1}$$

Here, K is the magnetic anisotropy constant, V the volume of the particle, m the dipole moment, and θ the angle between the moment and the anisotropy axis.

As shown in Fig. 6.2(a), the particle may be in two degenerate states, with its moment $\mathbf{m}$ pointing parallel to the anisotropy axis $\hat{\mathbf{n}}$ or antiparallel to it. The energy barrier between the two states KV is generally very large in ferromagnetic particles. However, in superparamagnetic particles, $KV \sim k_BT$, and the particle may thermally activate over the barrier from one state to the other, a process called Néel relaxation. The rate of transitions between the two states is proportional to a Boltzmann factor of the anisotropy barrier

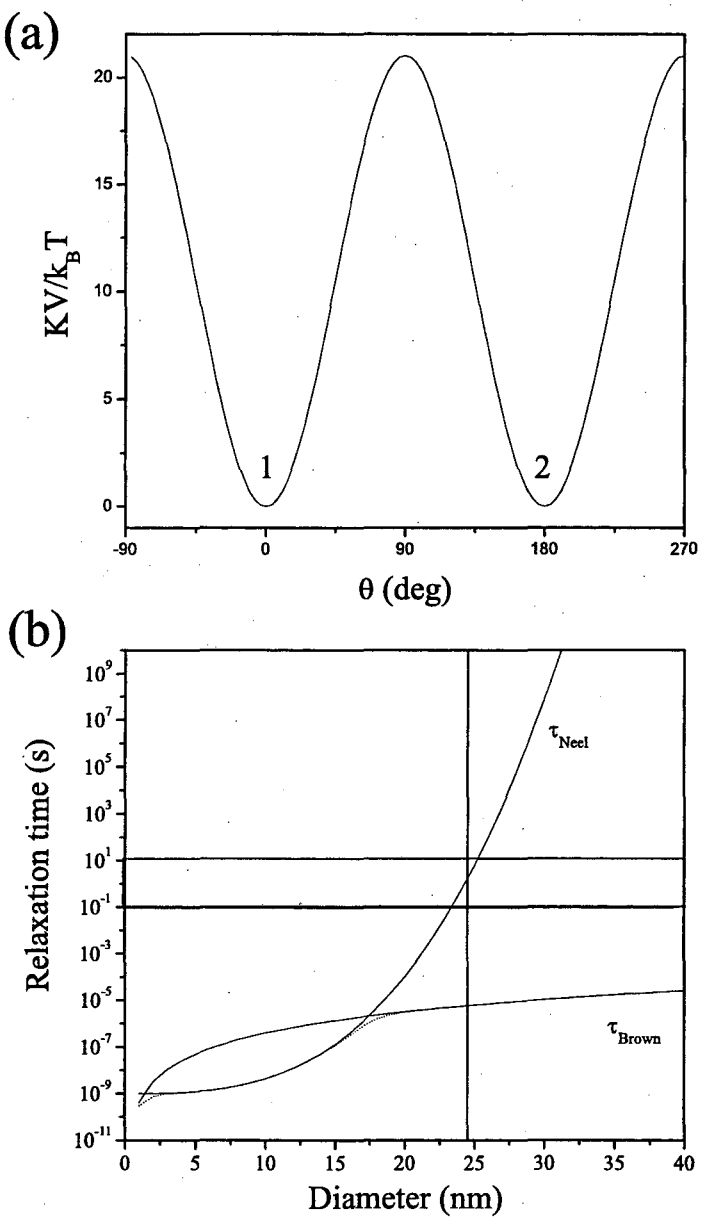

Figure 6.2: Superparamagnetism of nanoparticles. (a) The anisotropy energy of the particle has two minima. The dipole moment may lie parallel (state 1) or antiparallel (state 2) to the anisotropy axis. When the energy barrier $KV \sim k_B T$, transitions from one state to the other may occur over a measurable time. (b) Brownian and Néel relaxation times for an ideal, single domain magnetite (Fe_3O_4) nanoparticle of diameter d. For a $24nm$-diameter particle $\tau_N \sim 1s$ and $\tau_o \sim 1\mu s$.

energy KV. Thus, the lifetime of each state, the so-called Néel relaxation time, is given by

$$\tau_N = \tau_N^{(0)} \exp \frac{KV}{k_B T}, \tag{6.2}$$

where $\tau_N^{(0)}$ is generally taken to be $10^{-9}s$ [61]. For $\tau_N \sim 1s$, $KV \approx 21 k_B T$. The anisotropy constant for bulk magnetite is $K = 1.1 \times 10^4 J/m^3$, so this corresponds to a particle of diameter $\sim 24nm$. (Conversely, the dipole moment of a typical magnetosome with a diameter $40nm$ relaxes in a time $\tau_N = 10^{31}s$, longer than the age of the universe! Thus, the magnetosome is ferrimagnetic.)

In suspension, particles of that size undergo rotational Brownian motion, as I described in Section 5.2 with respect to magnetotactic bacteria. For a sphere of volume V, the Brownian relaxation time is given by

$$\tau_o = \frac{3\eta V}{k_B T} \tag{6.3}$$

(To maintain consistency with Part I, I will use the same symbol, τ_o, for Brownian rotation.) Note that the two relaxation times depend differently on the particle size; τ_N is exponential in V, τ_o is linear in V. Figure 6.2(b) plots the relaxation times for ideal single-domain magnetite particles as a function of diameter. By choosing suitably sized nanoparticles, one may achieve $\tau_N \gg \tau_o$; for example, for a $24nm$-diameter particle $\tau_N \sim 1s$ and $\tau_o \sim 1\mu s$.

6.3.3 MAgnetic Relaxation/remanence ImmunoAssay

The relaxation process which one measures is the faster of the two described above. For a particle with a diameter $> 17nm$, Brownian rotation is observed. However, if the particle is somehow immobilized, thus "freezing out" its Brownian motion, Néel relaxation is observed. It is this change in relaxation time when a particle becomes immobilized that is the basis of MARIA. Figures 6.3(a)-(c) depict the principle of the technique. In (a) an immobilized target is immersed in a suspension of superparamagnetic nanoparticles coated with antibodies specific to that target. Some fraction binds to the target, while the rest remains in suspension. A pulsed external magnetic field is applied to align the dipole moments of the particles.

When the field is turned off in (b), the free magnetic labels randomize by Brownian rotation in a few microseconds—a time scale shorter than the response time of the SQUID electronics—and they are not observed. In contrast, bound labels cannot rotate and thus

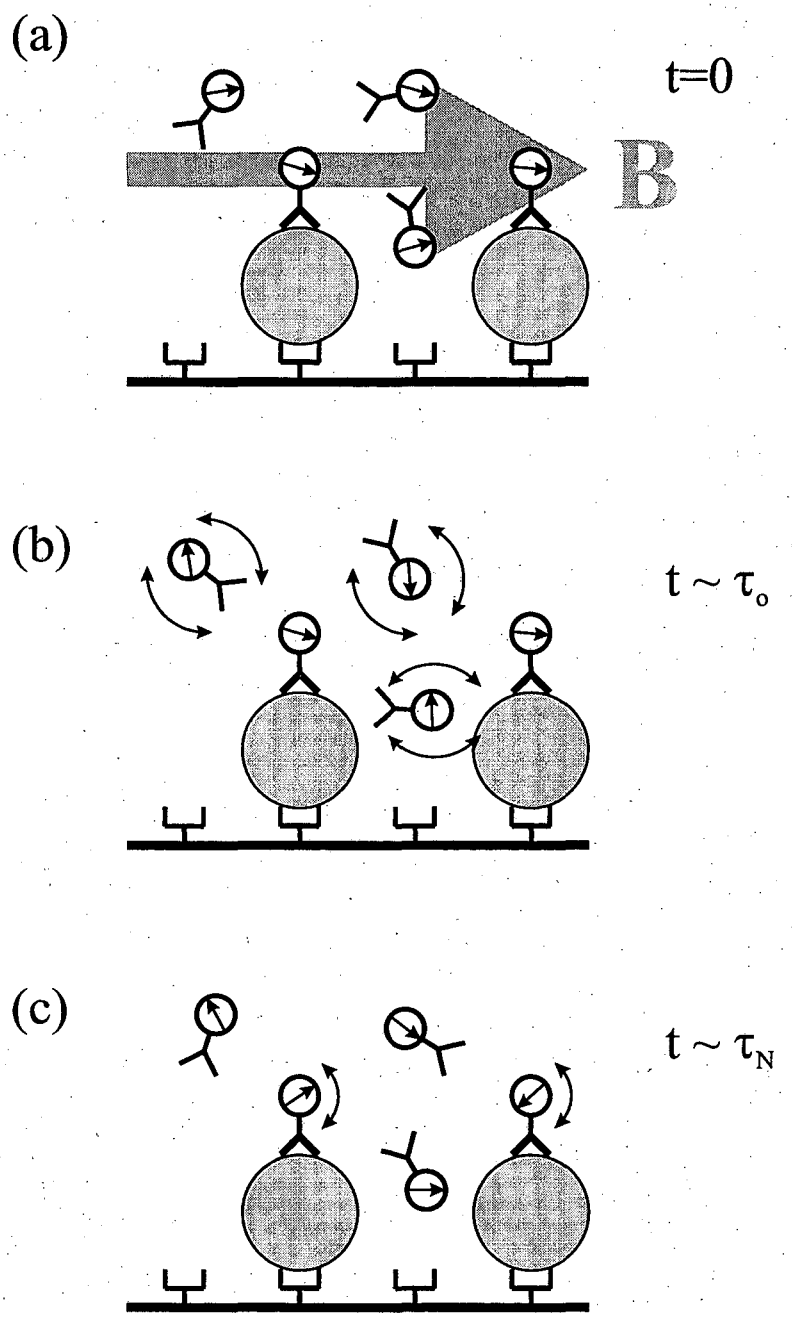

Figure 6.3: Principle of MARIA. (a) Targets are bound to a substrate (nonspecifically, or with the aid of an antibody). Superparamagnetic nanoparticles linked to an antibody against the target are added and aligned by an external magnetic field. When the field is removed, particles that are not bound to the target randomize by Brownian rotation in a very short time (b), and particles that are bound randomize slowly by Néel relaxation (c).

relax slowly by the Néel mechanism, producing a measurable field for a period of several seconds. As a result, in (c) the SQUID detects the decaying magnetic field produced *only* by the bound superparamagnetic nanoparticles.

This feature of MARIA distinguishes it from most of the standard immunoassay techniques in use today. Whereas methods like ELISA necessitate time-consuming wash steps to remove the fraction of antibodies that are not bound to their targets, MARIA avoids such matters entirely since the signal only comes from the bound fraction. Such assays are called "homogeneous" assays, since the signal is generated by a homogeneous population of bound antibodies (as opposed to a heterogeneous population of bound and unbound antibodies).

6.4 Materials and methods

6.4.1 Antigen and antibody

To test this technique with the SQUID microscope, it was necessary to obtain superparamagnetic particles of the right size [in the range defined in Fig. 6.2(b)] and a robust antigen/antibody system. In our initial studies, we used the bacteria *Listeria monocytogenes* as our target microorganism. However, we soon found that the antibody we were using cross-reacted with our control target *E. coli.* As a result, we decided on using an artificial target. We collaborated with Prof. Ray Stevens, then in the Department of Chemistry at UC Berkeley (now at Scripps Research Institute), and Prof. Mark Alper, in the Department of Molecular and Cell Biology at UC Berkeley and the Material Sciences Division at Lawrence Berkeley National Laboratory, in finding and developing a viable antibody and antigen.

A standard technique in molecular biology is the alteration of a protein of interest to include a man-made "tag". This "tag" consists of an artificial sequence of amino acids (typically 6-10 amino acids long), which is inserted at the end of the protein sequence, but does not significantly alter its conformation or function. Its use is that it can be recognized by a man-made "anti-tag" antibody, allowing the protein to be isolated and purified. The appeal of such a tool in our experiment is that the artificial nature of the antigen (the tag) and the antibody completely eliminates the problem of cross-reactivity.

Our artificial target consisted of liposomes (bilipid vesicles) carrying the human CCR5 receptor. The CCR5 protein is a trans-membrane protein which acts as the receptor

for the HIV virus in humans. The end of the protein was altered to carry a unique sequence of eight amino acids called the FLAG tag. Antibodies against this epitope were attached to superparamagnetic particles.

Yan Poon, an undergraduate assistant in Prof. Stevens research group, was chiefly responsible for making the CCR5/FLAG carrying-liposomes. Yeast cells (*Saccharomyces cerevisiae*) of the strain BJ2168 into which the CCR5 gene was cloned were used as a source of CCR5-containing membrane fragments [62]. The human CCR5 gene was inserted into the yeast's plasmid DNA [63]. The Polymerase Chain Reaction (or PCR), a technique which utilizes a special type of polymerase (a protein used in DNA replication) to duplicate a particular gene in a DNA fragment, was used to amplify the human CCR5 gene. The eight amino acid sequence, DYKDDDDK[1], which makes up the FLAG tag was introduced at the carbon end of the CCR5 protein peptide backbone (the so-called C terminus) for the purpose of serving as the antigenic site.

The yeast cells were grown to a desired density in a synthetic growth medium at 26°C, then broken up to collect the membrane bound-CCR5 proteins they had synthesized. First, they were centrifuged out of growth medium into a cell paste. Sixty grams of this paste were resuspended in a solution of 50 mM HEPES (at pH 7.5), with 10% weight by volume sucrose, and 5mM EDTA, and were broken up using a Braun Scientific (Allentown, PA) glass bead cell homogenizer. Unlysed cells were removed by ultracentrifugation at 750×g. The membrane fragments containing CCR5 were subsequently collected by ultracentrifugation at 186,000×g. All steps were carried out at 4°C and all solutions supplemented with protease inhibitors, to prevent digestion of the desired protein.

Once the membrane fragments were isolated and purified, they had to be reconstituted to form CCR5/FLAG-carrying liposomes. Liposomes were made by mixing two phospholipids (from Avanti Polar Lipids, Inc., Alabaster, AL), 1-palmitoyl-2-oleoylphosphatidylcholine (POPC) and 1-palmitoyl-2-oleoylphosphatidylglycerol (POPG) at a ratio of 60:40 (by weight), mixed in chloroform and dried under nitrogen gas. The liposomes were then resuspended in a buffer containing 50mM HEPES (pH 7.5), 150 mM NaCl, and 5mM EDTA to a concentration of $7.5mg/mL$ of total lipid. They were then sonicated for 1 hour at 4°C to homogenize their size. The solution was then diluted to a final concentration of $3.75mg/mL$ of total lipid with the same buffer as described above. The mixture was

[1]The letters represent the amino acids aspartic acid (D), tyrosine (Y), and lysine (K).

then saturated with the detergent n-nonyl-β-D-glucoside (Anatrace) by gradual addition of the detergent. Saturation was reached when the solution turbidity quickly disappeared. Finally, CCR5-containing membranes, solubilized in the detergent n-decyl-β-D-maltoside, were mixed in proportions with $10mL$ Bio-Beads SM-2 (Bio-Rad) at 4°C overnight. The resulting liposomes were collected by ultracentrifugation at 229,000×g for 2 hours. The pellet was then resuspended in $1mL$ of 50 mM HEPES (pH 7.5), 150 mM NaCl, and 5 mM EDTA.

6.4.2 Magnetic nanoparticles

Superparamagnetic particles of various sizes and cross-linked with the desired antibody can be obtained from a number of companies. Quantum Magnetics (Madison, CT) manufactures nanoparticles with our stringent size specifications (such that $\tau_N \gg \tau_o$). Their particles are manufactured from two or three 10-15nm magnetite crystals fused together into a larger core. We obtained particles with a specified average core diameter of $35 \pm 5nm$, as measured by electron microscopy. The nanoparticles were coated with bovine serum albumin (BSA) and coupled to the anti-FLAG antibody with a proprietary linker. The specified average coated particle size, measured with light scattering, was $56nm$. Figure 6.4 is a transmission electron micrograph (TEM) of these nanoparticles, deposited on a SiO-coated copper grid. Despite the vendor specifications, it is clear that there is a wide distribution of sizes, from 30 to $160nm$. The particles were stored suspended in a 10mM sodium phosphate (pH 7.5) buffer with 5% isopropanol preservative. We estimated the particle concentration to be 40nM ($2.4\times10^{13}mL^{-1}$). Over time the particles may settle out or form aggregates, but they are easily redispersed by light sonication or vortexing.

Using a low-T_c SQUID susceptometer (Magnetic Property Measurement System by Quantum Design, San Diego, CA), operated with the help of Yan-Mei (Eileen) Wang in Prof. Zettl's research group in the Department of Physics, we were able to measure the average dipole moment of the particles. The particles, in a $1mL$ dilute suspension, were placed in a sealed glass tube fitted on the end of the sample insert. We measured the magnetization of the sample at room temperature as a function of applied magnetic field (ranging from 0-100G). In a magnetic field, each particle has an energy $E = \mathbf{m}\cdot\mathbf{B} + KV(\mathbf{m}\cdot\hat{\mathbf{n}}/m)^2$. In a fluid, where the particle is free to rotate, it is energetically favorable for the dipole moment to align with the anisotropy axis. Thus, the second term in the energy is

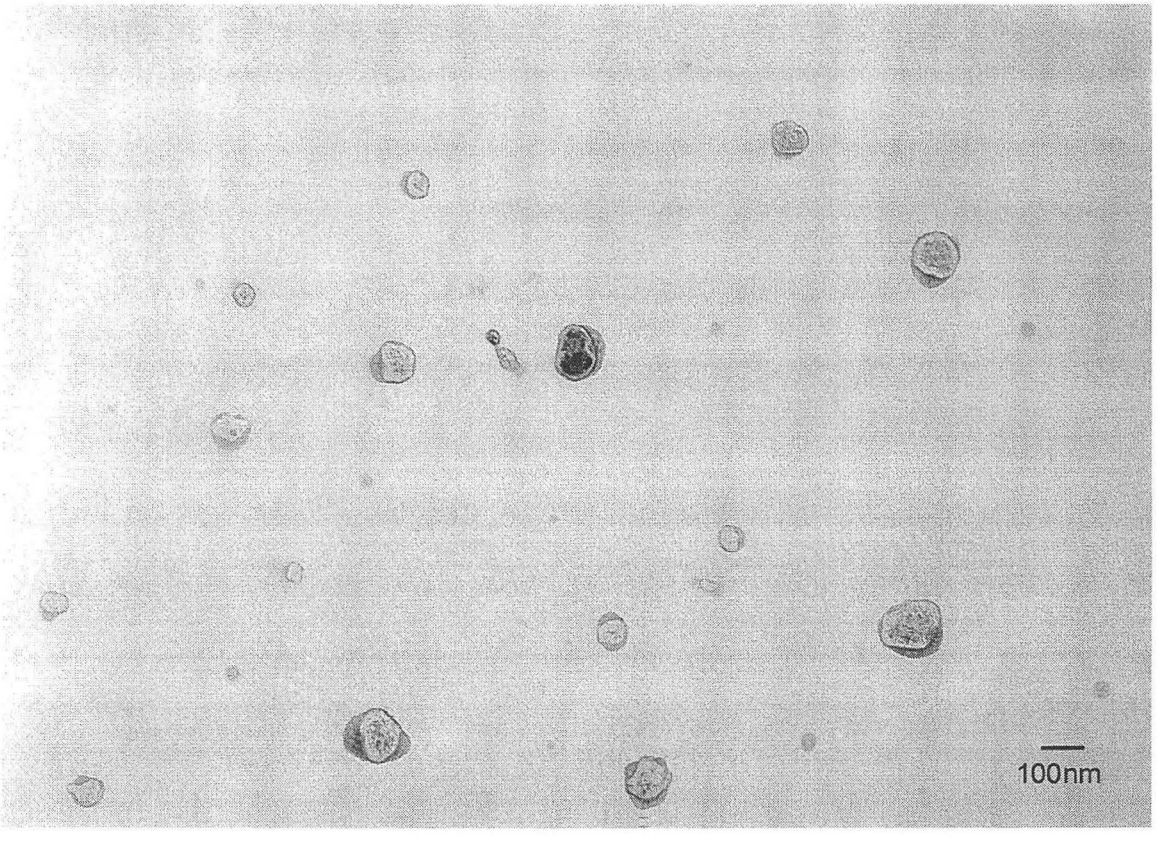

Figure 6.4: Transmission electron migrograph (TEM) of Quantum Magnetics nanoparticles, deposited on a SiO-coated copper grid.

constant, and the magnetization of the suspension of nanoparticles is simply $M = \rho_m m L(\xi)$, where $L(\xi)$ is the Langevin function (see Section 4.2.2) and $\xi = mB/k_BT$ [61]. Figure 6.5 shows a plot of the magnetization of a suspension of Quantum Magnetics nanoparticles. The data was fitted to a Langevin function to obtain a value of $m \approx 3 \times 10^{-18} A{\cdot}m^2$ for the dipole moment (note that no knowledge of the particle density ρ_m is necessary to determine m).

A magnetosome, which has a typical diameter of $35nm$, has a dipole moment of $10^{-17} A \cdot m^2$ and is permanently magnetic. On the other hand, the commercial particle, which has the same nominal diameter, has a moment that is a factor of 3 times smaller and is superparamagnetic. The diameter of the commercial particle is also much larger than that indicated by Fig. 6.2(b) for $\tau_N \sim 1s$. The difference is that the commercial particle consists of multiple domains, for which our simple models break down.

6.4.3 Sample preparation

We utilized the same sample cell integrated with the SiN vacuum window described in the bacteria experiments to carry out the magnetic immunoassay. However, rather than using the SiN window itself as a surface on which to bind the targets, we used a $6\mu m$-thick mylar sheet, which we cut into squares approximately $440\mu m$ on a side. In this way, the mylar square film could be placed in the microscope sample cell flush against the SiN vacuum window. This allowed us to have a removable, disposable sample, which facilitated experiments greatly. The added separation between the SQUID and the sample due to the mylar film, and the resultant decrease in signal was not significant. The SQUID-to-sample distance was adjusted by three micrometers to $\sim 40\mu m$, typically, limited by the angular misalignment between the SQUID chip and the SiN window.

To simplify matters, we decided against using a capture antibody. Fortunately, the liposomes readily adhered electrostatically to the mylar sheet, breaking open upon contact and uniformly coating the surface. The targets were immobilized onto the mylar surfaces by immersion. Mylar films incubated for up to an hour in suspensions of liposomes of various concentrations with bovine serum albumin (BSA); the BSA blocked non-specific binding of magnetic particles to the mylar. The most concentrated liposome suspension contained 7.4mM of lipid. The film was rinsed with a solution of phosphate buffered saline (PBS) and 0.05% Tween.

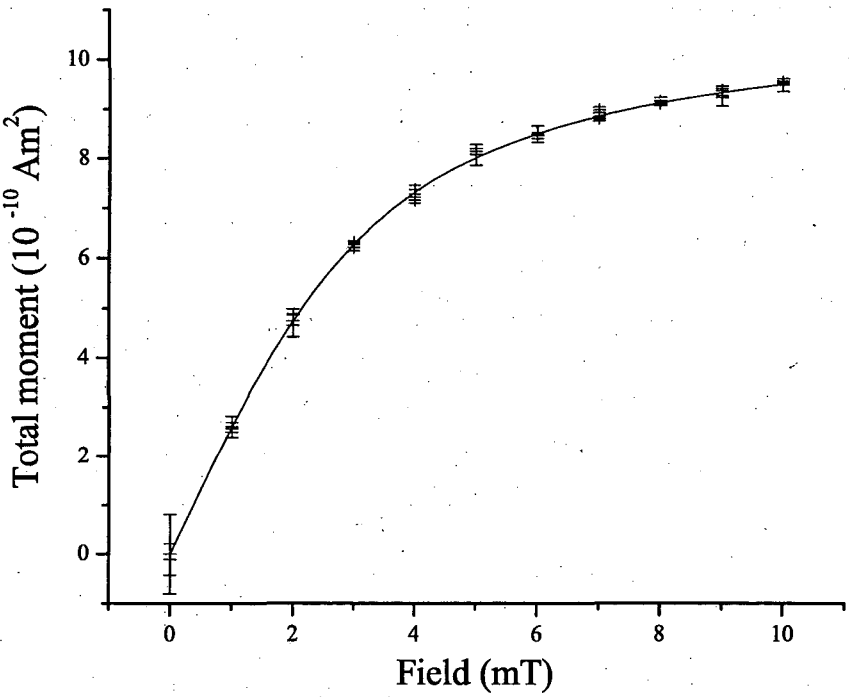

Figure 6.5: Magnetization of a suspension of superparamagnetic nanoparticles. The fit to a Langevin function yields a dipole moment of $m \approx 3 \times 10^{-18} A \cdot m^2$.

Usually, $30\mu L$ of the suspension of antibody-linked magnetic particles were added to the film in the sample cell, of which only $\sim 1\mu L$ was directly above the SQUID. We allowed up to 2 hours to elapse before taking data, to ensure that significant binding occurred. In selected experiments, the mylar samples were mixed with the magnetic particles in a separate container before transferring them to the microscope. In this case, we added $30\mu L$ PBS to the mylar in the sample cell to resuspend any unbound nanoparticles.

In the next chapter I will describe in detail the results from the MAgnetic Relaxation/remanence ImmunoAssay experiments performed with the SQUID microscope. As described above, these pilot experiments used artificial targets—the liposomes containing the CCR5 protein, tagged with FLAG. Finally, I will spend some time on modifications to the system to improve the sensitivity of the magnetic immunoassay further.

Chapter 7

SQUID Magnetic Relaxation Immunoassay

7.1 Introduction

As should be evident from the previous chapter, the magnetic immunoassay developed by Weitschies *et al.* [57] combined with the SQUID microscope should yield a very sensitive technique for the detection of biological substances. The magnetic labeling technique, by exploiting the difference in the Néel and Brownian relaxation times of superparamagnetic particles, can distinguish between labels bound to their targets and free labels. Such a homogeneous assay offers advantages over other assays. The SQUID microscope, as demonstrated in the observation of a single magnetotactic bacterium, can detect a very small dipole moment. In principle, under optimal conditions the SQUID microscope can detect the flux change due to the motion of a single-domain 35-nm magnetite nanoparticle.

In the following chapter, I will describe an implementation of the Magnetic Relaxation/remanence ImmunoAssay with the SQUID microscope. The pilot experiment presented here was designed as a diagnostic test of these newly developed methods. As mentioned in the previous chapter, rather than test the immunoassay on a real pathogen like *E. coli*, we constructed an artificial antigen consisting of liposomes containing the FLAG tag. The advantage of such an antigen is that it allows a level of control not afforded by real systems. We can control the amount of FLAG epitope present in each liposome, and minimize the cross-reactivity of anti-FLAG antibodies to our controls. The goal of

the experiment was to characterize the technique and measure its sensitivity, particularly in comparison to other standard immunoassay techniques (such as ELISA). Even at this early stage, it appears that this technique is enormously sensitive, yet it is far from being completely optimized. At the end of the chapter I will outline ways in which the system could be altered to improve the sensitivity further, by as much as two orders of magnitude.

7.2 CCR5-liposome immunoassay

7.2.1 Néel relaxation signal

To observe the Néel relaxation of the sample, we pulsed a magnetic field $B = 0.3mT$ which magnetized the nanoparticles. In the same manner as that described in Section 5.2.2, B was applied in a direction parallel to the plane of the SQUID so as to minimize the flux coupled into it directly from the coil. We were able to align the two to within 0.1°, so that less than 0.2% of B coupled to the sensor. In contrast to the bacteria experiment, we were less concerned about field uniformity and used a two-coil non-Helmholtz configuration to apply the magnetizing field. As in the bacteria relaxation measurements, to maximize the coupling of the SQUID to the field generated by the sample (which was magnetized in-plane), the SQUID was offset laterally by $220\mu m$ from the center, to the position where the perpendicular component of the field from the sample was largest. The magnetizing field B was pulsed on for $1s$ and off for $1s$; data were collected during the latter period. The time for the field to turn off, about $60\mu s$, was negligible. One hundred averages were typical.

Figure 7.1 shows a typical plot of the magnetic flux measured by the SQUID for the $1s$ data collection time interval for different samples. Since large transients generated by switching the field off obscured the relaxation signals during the first $25ms$, this time interval has been excluded. Trace A shows the signal from a mylar film coated with liposomes containing the FLAG epitope placed in a 0.4nM suspension of anti-FLAG labeled nanoparticles. The decaying magnetic flux is generated by the Néel relaxation of the nanoparticles bound to the sample. The large response indicates that a significant number of nanoparticles bind to the sample, as expected from the known, high binding affinity of anti-FLAG antibody to FLAG.

On the other hand, if a sample of liposomes containing no FLAG epitopes is placed

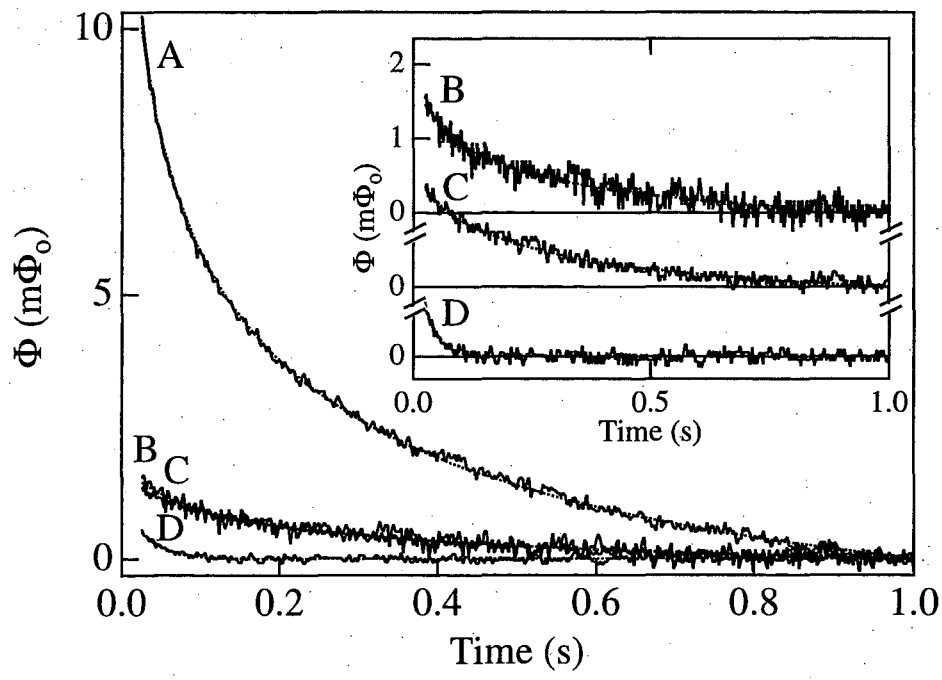

Figure 7.1: Néel relaxation. A mylar substrate with liposomes containing the FLAG epitope generates a large relaxation signal (trace A) in the presence of anti-FLAG labeled nanoparticles. Liposomes with no FLAG (trace B), and nanoparticles alone (trace C) generate very little response. A small exponential background decay (trace D) due to eddy currents in the microscope is present when there is no sample. The inset shows an expanded view of the lower three traces. Fits are in dotted lines. The background decay (trace D) was subtracted from traces A, B, and C prior to fitting.

in the same nanoparticle suspension, only a very small signal is produced, as seen in trace B in Fig. 7.1 (also in the inset, offset for clarity)[1]. A comparable response is produced by the nanoparticle suspension alone (trace C, almost superimposed over trace B in Fig. 7.1, and inset, offset for clarity). We believe these signals are due to a small fraction of particles binding non-specifically to the substrate or to the sample cell. Clearly the method can distinguish magnetic labels that bind to the target from those that do not.

The decays in the above traces are not exponential. This is because the ensemble of magnetic nanoparticles has a wide distribution of particle and core sizes, and the Néel time depends exponentially on the volume. Rather, it can be shown that for small magnetizing fields $B \ll k_B T/m$, the flux from the bound magnetic nanoparticles decays logarithmically as $\Phi(t) \propto \ln(1 + t_{mag}/t)$ [64], where t_{mag} is the magnetization time, here $1s$. Thus, the data in Fig. 7.1 are fitted to

$$\Phi(t) = \Phi_s \log[1 + t_{mag}/(t - t_o)], \tag{7.1}$$

with fitting parameters Φ_s, and t_o (t_{mag} is held constant at $1s$). The quantity Φ_s is the Néel relaxation signal amplitude, and t_o is a time offset, typically $\sim 1ms$. From Eq. (7.1), Φ_s is the change in flux between time $t \approx 50ms$ and $t = 1s$ in the relaxation signal. As shown in Fig. 7.1, the fits in dotted lines are uniformly excellent. The derivation of this logarithmic time dependence is sketched out below; for more details refer to Berkov *et al.* [64].

7.2.2 Non-exponential decay

As discussed in the previous chapter, each nanoparticle can be in one of two states corresponding to the dipole moment $\mathbf{m}$ pointing parallel (state 1) or antiparallel (state 2) to the anisotropy axis $\hat{\mathbf{n}}$. In the absence of a field the two states are degenerate and the average moment $\langle m \rangle$ is zero. In the presence of a field B, however, there is an energy difference between the two states causing one to be more populated than the other. There, the average moment $\langle m \rangle = m(n_1 - n_2)$, where $n_{1,2}$ are the populations of states 1 and 2, respectively. I have defined the states such that the moment is positive in state 1, negative in state 2.

Transitions from state 1 to state 2 and vice versa occur at a rate γ which depends on the anisotropy energy $E = KV$ and the applied magnetic field B. For $B = 0$, the inverse

[1]Generally, the noise on the decay curves is determined by the SQUID, and thus is identical to that observed in the absence of a sample and a magnetic field pulse. However, the noise on trace B in Fig. 7.1 is somewhat higher; it is likely that this increase was due to magnetic flux trapped in the SQUID.

of the rate, $1/\gamma$ is the Néel relaxation time, τ_N, as defined in Eq. (6.2). In the experiment, we magnetize the nanoparticles for a time t_{mag}. The overpopulation of state 1 with respect to state 2 clearly depends on this magnetization time:

$$n_1 - n_2 = \Delta n^{eq}(E,B)\left(1 - e^{-\gamma(E,B)t_{mag}}\right), \tag{7.2}$$

where Δn^{eq} is defined as the equilibrium overpopulation as t_{mag} goes to infinity, and depends on the energy difference due to the field. Once the sample is magnetized for a time t_{mag}, the field is turned off and each nanoparticle relaxes to its zero-field configuration. Thus, the average dipole moment is given by

$$\langle m \rangle = m\Delta n^{eq}(E,B)\left(1 - e^{-\gamma(E,B)t_{mag}}\right) e^{-\gamma(E,B=0)t} \tag{7.3}$$

as a function of time.

The exponential time dependence exhibited in Eq. (7.3) would describe the relaxation of one ideal, single-domain nanoparticle, or an absolutely homogeneous ensemble of such particles. However, a real ensemble is greatly heterogeneous, containing a wide distribution of sizes and shapes, and multiple-domain nanoparticles. As a result we must integrate Eq. (7.3) over a distribution $\rho(E)$ of anisotropy energies E

$$\langle m \rangle = \int_0^\infty dE\, \rho(E) m\Delta n^{eq}(E,B)\left(1 - e^{-\gamma(E,B)t_{mag}}\right) e^{-\gamma(E,0)t} \tag{7.4}$$

where the distribution is normalized such that $\int_0^\infty dE\, \rho(E) = 1$. Néel has shown that the transition rate γ depends quadratically on the field [65]. Thus, for small fields $B \ll E/m$, it is reasonable to assume that $\gamma(E,B) \approx \gamma(E,0) = \gamma_o e^{-E/k_BT}$ as given by Eq. (6.2) ($\gamma_o = 1/\tau_N^{(0)} = 10^9$Hz). As a result,

$$\langle m(t) \rangle = \int_0^\infty dE\, f(E,B)\left(1 - e^{-\exp(-E/k_BT)\gamma_o t_{mag}}\right) e^{-\exp(-E/k_BT)\gamma_o t}. \tag{7.5}$$

where $f(E,B) \equiv \rho(E) m\Delta n^{eq}(E,B)$.

In general, the integral in Eq. (7.5) can only be evaluated knowing the exact form of the distribution function $\rho(E)$. However, if the distribution is sufficiently broad, we can take it out of the integral, invoking the first mean-value theorem of integral calculus, which states that there is a value of energy E^* such that

$$\langle m(t) \rangle = f(E^*,B) \int_0^\infty dE\, \left(1 - e^{-\exp(-E/k_BT)\gamma_o t_{mag}}\right) e^{-\exp(-E/k_BT)\gamma_o t}. \tag{7.6}$$

The integral can then be carried out analytically by making the substitution $\Gamma \equiv e^{-E/k_BT}$, after which it takes the form

$$\text{P.V.} \int_0^1 \frac{d\Gamma}{\Gamma} (e^{-\Gamma\gamma_o t} - e^{-\Gamma\gamma_o(t_{mag}+t)}). \tag{7.7}$$

P.V. denotes the principal value, which resolves the singularity at zero. The integral, evaluated in this way, yields:

$$\langle m(t) \rangle = k_B T f(E^*, B) \ln\left(1 + \frac{t_{mag}}{t}\right) \tag{7.8}$$

valid for times $t \gg 1/\gamma_o = 10^{-9}s$. This is the logarithmic time dependence used to fit the data. For shorter times, correction terms must be included which remove the singularity at $t = 0$ [64].

7.2.3 Background response

As shown in trace D in Fig. 7.1, we detected a small signal even in the absence of liposomes and nanoparticles. The signal was unchanged when we moved the cell further away from the SQUID, demonstrating that it was not due to particles adhering to the SiN window. In the inset of Fig. 7.1, it is apparent that the decay of the signal does not follow the same, logarithmic time dependence given by Eq. (7.1) as do traces A, B, and C. As shown in Fig. 7.2, this background signal is better fit to a sum of two exponentials with time constants of $\sim 40ms$ and $\sim 4ms$. The data in the lower portion of Fig. 7.2 was taken in the same measurement bandwidth (400Hz) as trace D; the data in the inset was taken with a bandwidth five times larger (2kHz) and shows the fast ($4ms$) decay more clearly. Because the first $25ms$ were removed from the data in Fig. 7.1 this fast decay is largely absent from trace D.

The fact that this background signal does not change in amplitude when the SQUID-sample separation is increased and does not follow the same time dependence as that measured for the nanoparticles suggests that it must be generated by another source. The decay time of the coils when they are turned off was measured independently and is much faster than this decay. Response times of the SQUID and readout electronics are also much too fast to produce such an effect. We believe that this background flux is produced by eddy currents induced in nearby metal objects in the microscope. In response to a magnetic pulse, a metallic object behaves like an R/L circuit. It generates currents, which

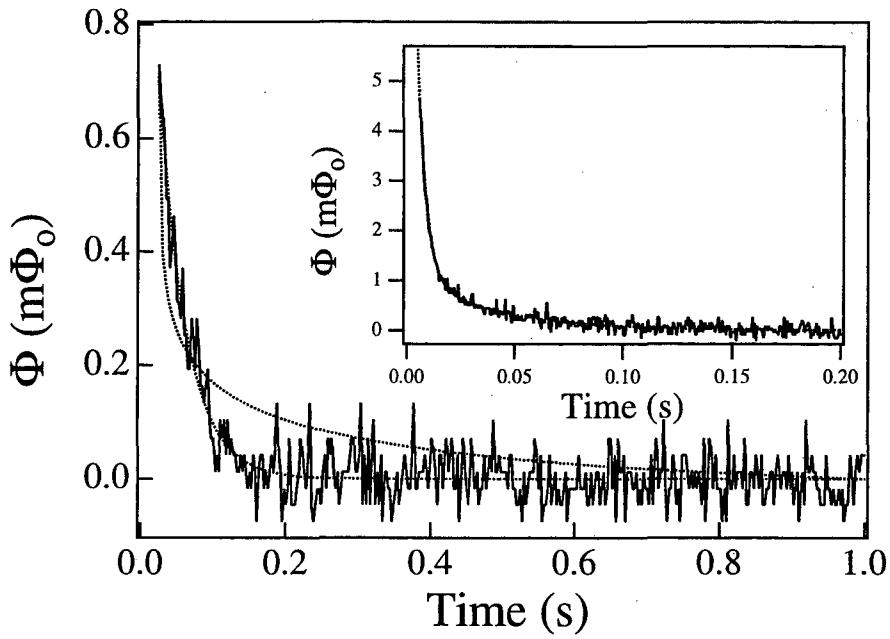

Figure 7.2: Background relaxation signal. The data is fitted to an exponential (dotted line) of amplitude $1.3m\Phi_o$ and time constant $38ms$. For comparison, a logarithmic decay of the form 7.1 is included (dotted line), and represents a best fit of the background relaxation signal to such a function. Φ_s is approximately $0.2m\Phi_o$. The trace in the inset is a measurement taken at a higher sampling rate (2kHz), and exhibits a fast decay not seen in the other trace. It is fitted to a sum of two exponentials (dotted line); one with amplitude $1.1m\Phi_o$ and time constant $39ms$, the other $17m\Phi_o$ and $4ms$.

decay with a characteristic R/L time. These eddy currents may in turn produce a decaying magnetic field which is detected by the SQUID.

Metals which are likely culprits are the brass arms (E in Fig. 3.1 in Section 3.2), the positioning micrometers (F), and the brass bellows (C). These objects are near the magnetizing coils and are near the SQUID. The μ-metal shields surrounding the microscope may also be a culprit. The shields may not only generate eddy currents in response to a field pulse, but the magnetic relaxation due to the reorientation of magnetic domains inside the μ-metal may also affect the SQUID. Due to the complex geometry of the problem, it is exceedingly difficult to estimate the amplitude and the time dependence of flux generated by eddy currents inside the metal objects mentioned above. Experimentally, Helene has noticed that moving the microscope inside the shield, closer to its μ-metal walls affects the background response. The change could be due to the smaller distance between the SQUID and the μ-metal (if it is the source), or it could be due to the reconfiguration of the field at the source due to the shield. Unfortunately, we cannot operate the microscope outside of the shields and investigate this further. Finally, we have recently constructed smaller coils. For the same magnetizing field of $0.3mT$, the background is significantly smaller. Presumably, the smaller coil size leads to smaller stray fields at the locations of the metal objects generating the signal.

Regardless of the source, this background currently sets our detection limit, since Néel relaxation signals of comparable or lower amplitude cannot be resolved accurately. I conservatively estimate that the smallest amplitude signal we can detect is $\Phi_s \approx 0.2m\Phi_o$. Fig. 7.2 displays a Néel relaxation signal of that amplitude against the background signal. In all of the experimental results that follow, each measurement of a sample is succeeded by a measurement of the background. The background trace is then subtracted from each data set to determine the amplitude Φ_s. This procedure also ensures that the sample cell is clean of residues before subsequent measurements are taken.

7.2.4 Dependence of signal on nanoparticle and liposome concentrations

For an immunoassay to be quantitative, the measured signal must have a well-defined relation to the concentration of target and the concentration of labeled antibody. Figures 7.3 and 7.4 display the dependence of the signal amplitude, Φ_s in Eq. (7.1), on the nanoparticle and liposome concentrations, respectively. In both figures, the background

contribution in the absence of a sample is subtracted from the data before determining Φ_s. The error bars are determined from the fit to Eq. (7.1), and do not account for systematic and experimental errors such as sample variability. In Fig. 7.3, the detection limit of $\sim 0.2m\Phi_o$, due to the background decay, is indicated by the horizontal dotted line. The data point at the lowest concentration is below this line and has a large error because the background has been subtracted from it.

To vary the nanoparticle concentration, mylar films with identical liposome densities were prepared. The mylar was incubated for 1 hour in a liposome suspension containing 1.5mM lipid. The films were then soaked for 2 hours in suspensions of magnetic nanoparticles diluted to different extents with PBS and 0.05% Tween. As seen in Fig. 7.3, Φ_s scales approximately linearly with the concentration of suspended particles. This result is expected since the number of particles bound to FLAG should be linear in the particle concentration, so long as the FLAG binding sites are not saturated.

To vary the liposome concentration, mylar films were incubated in various concentrations of liposomes for 1 hour, then in the same 0.4nM suspension of nanoparticles for 2 hours. As seen is Fig. 7.4, Φ_s is approximately linear in the liposome concentration, as expected since the number of FLAG epitopes on the mylar, and hence the number of bound nanoparticles (assuming a sufficient quantity are present) should scale linearly with the liposome concentration. The values of Φ_s for the highest two liposome concentrations may indicate that saturation occurs.

7.3 Calibration

7.3.1 Transmission electron microscopy

The plot in Fig. 7.3 calibrates the measured Néel relaxation signal against the concentration of nanoparticles in which the samples were incubated. Since only a small fraction of the nanoparticles in suspension bind to their targets on the mylar film, this plot does not tell us how many nanoparticles are detected by the SQUID. Indeed, a true measure of the sensitivity of this method is the minimum detectable number of nanoparticles bound to the mylar. A conversion factor between relaxation amplitude Φ_s and number of bound nanoparticles N can be measured directly, or modeled theoretically.

The most direct calibration procedure is to count the particles directly using trans-

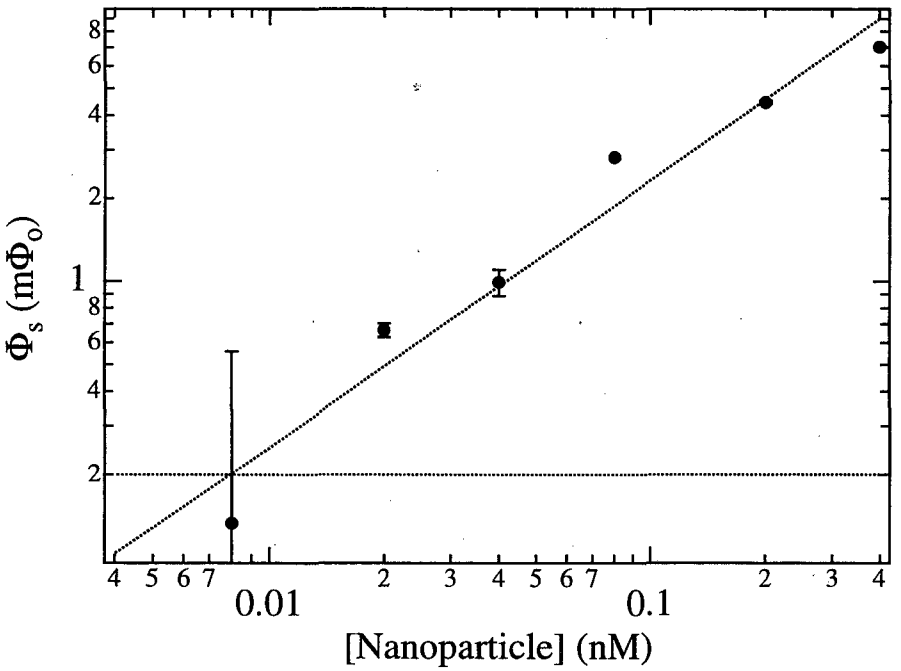

Figure 7.3: Φ_s vs. nanoparticle concentration. The amplitude of the Néel relaxation signal is measured as a function of the concentration of nanoparticles in the suspension. The number of liposomes per mylar sample is kept constant. The data at the remaining concentrations are fitted to a line of slope 0.97±0.11. The horizontal dotted line indicates our detection limit.

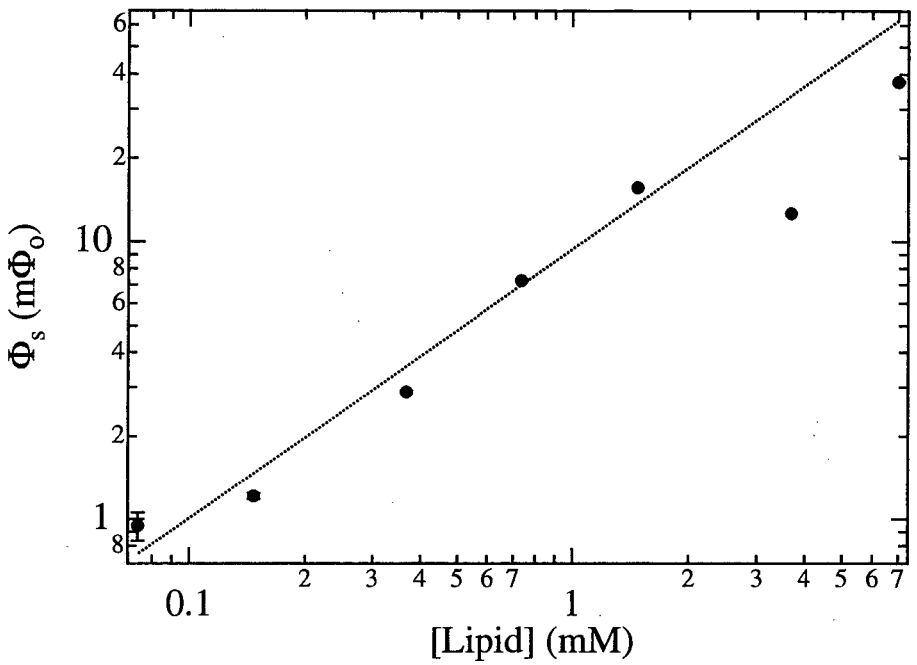

Figure 7.4: Φ_s vs. lipid concentration. Here, the Néel relaxation amplitude is measured as a function of the concentration of the liposome suspension in which the mylar samples are incubated. The concentration of nanoparticles is kept constant. At the highest concentration, the data may be rolling off due to saturation. The line fitted to the data excluding the highest two points has a slope of 0.97±0.09.

mission electron microscopy (TEM). A drop of diluted nanoparticle suspension was placed on a SiO_2-coated Cu TEM grid and allowed to evaporate, depositing particles across the grid. We imaged sections by TEM, counting the number of particles per unit area. Subsequently, several pieces of grid were cut (from the imaged area) into squares $440\mu m \times 440\mu m$ in area and their relaxation signals were measured by the SQUID. Figure 7.5 displays the results of this calibration procedure for two different nanoparticle concentrations. The signal amplitudes Φ_s from 5 or 6 squares from the same Cu grid were measured and averaged together. The average signal is plotted against the number of particles, measured by TEM. A line is fitted to the data (solid line), confined to pass through the origin. This fit yields a flux per particle $\Phi_s/N = 4 \pm 1n\Phi_o$. The estimated smallest amplitude signal that can be detected is $0.2m\Phi_o$, corresponding to a detection limit of $(5 \pm 2) \times 10^4$ nanoparticles.

What this number corresponds to in terms of number of liposomes is difficult to estimate. Since the exact number of FLAG epitopes coating the surface of each liposome is unknown, we cannot convert from number of bound nanoparticles to number of liposomes. We have attempted to count the number of liposomes on each mylar film directly by labeling them with fluorescent lipids and imaging the mylar under a fluorescence microscope. However, this method proved unsuccessful. In general, different targets will have varying numbers of binding sites for antibodies—ranging from 1 or 2 for macromolecules to thousands to millions for bacteria. Thus, the minimum detectable number of targets will vary depending on the target.

7.3.2 Theoretical modeling

It is instructive to compare the measured value of the calibration factor Φ_s/N to that which we expect from theory. An order-of-magnitude estimate for the Néel relaxation amplitude, Φ_s, may be obtained with some theoretical modeling. Equation (7.8) from Berkov *et al.* [64] expresses the average dipole moment of a distribution of nanoparticles. As in the relaxation measurements of magnetotactic bacteria (Sections 5.2.2 and 5.2.4), the SQUID only detects the component of the dipole moment parallel to the magnetizing field. Perpendicular components average out to zero. Thus, the measured flux is proportional to

$$\langle m \cos\theta \rangle = \langle \Delta n^{eq} \cos\theta \rangle k_B T \rho(E^*) \ln\left(1 + \frac{t_{mag}}{t}\right) \tag{7.9}$$

where θ is the angle between the field and the dipole moment.

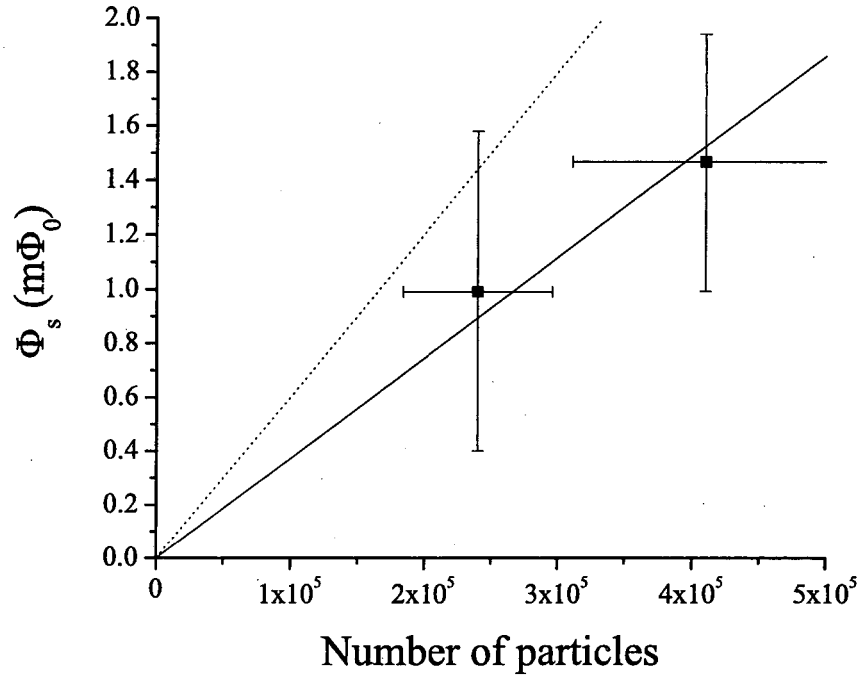

Figure 7.5: Calibration of Néel relaxation signal by transmission electron microscopy (TEM). SiO_2-coated Cu grids were deposited with nanoparticles, imaged by TEM, and measured by the SQUID. The relaxation signal amplitude Φ_s is plotted against the number of nanoparticles N for two nanoparticle concentrations. The error bars are due to the variations in the relaxation signal and in the number of nanoparticles measured from the various sections of the TEM grids. The solid line represents a best fit to the data, confined to pass through the origin. The slope $\Phi_s/N = 4 \pm 1 n\Phi_o$ per particle. The dotted line is the slope Φ_s/N estimated by theoretical modeling.

The magnetizing field generates an energy shift of $mB/k_BT\cos\theta$ in state 1 and $mB/k_BT\cos(\pi-\theta) = -mB/k_BT\cos\theta$ in state 2 of the nanoparticle. Thus, the overpopulation of state 1 with respect to state 2, Δn^{eq}, must be equal to $\tanh(mB/k_BT\cos\theta)$; for small magnetizing fields $B \ll k_BT/m$, $\Delta n^{eq} \approx mB/k_BT\cos\theta$. Taking the average in Eq. (7.9) yields

$$\langle m\cos\theta\rangle = \frac{mB}{3k_BT}\cdot k_BT\rho(E^*)\ln\left(1+\frac{t_{mag}}{t}\right) \tag{7.10}$$

One can think of the factor $mB/3k_BT$ as a polarization factor of the nanoparticles due to the magnetizing field. The factor of 1/3 comes about from the angular average over the random orientation of the nanoparticles with respect to the field. For $B = 0.3mT$ and $m = 3\times10^{-18}A\cdot m^2$, this polarization factor is equal to 0.07.

The total flux generated by the bound nanoparticles on the mylar sheet can be calculated by integrating the contribution to the flux of each particle over the sample as outlined in Appendix A. The geometrical factor $\mathcal{G}_y^{(2D)}$ defined by Eq. (A.11) in Appendix A represents the magnetic coupling between a square sample of side a, magnetized in-plane and offset laterally by $a/2$, and a SQUID of effective size ℓ_{eff} a distance z_o away. In the experiment, the mylar sheet was roughly $a = 440\mu m$ on a side, and the SQUID (a slit A-A type, with $\ell_{eff} = 128\mu m$) was $z_o = 40\mu m$ away. I assumed the nanoparticles were distributed uniformly across the substrate with a density $\sigma_m = N/a^2$, and were sufficiently dilute that magnetic interactions between them were negligible. From these parameters, $\mathcal{G}_y^{(2D)} \approx 4$. Using Eqs. (7.10) and (A.11), the Néel relaxation flux amplitude is given by

$$\Phi_s \approx N\cdot\frac{\mu_o m}{4\pi}\cdot\frac{mB}{3k_BT}\cdot\frac{\ell_{eff}}{a^2}g^{(2D)}\left(\frac{z_o}{\ell_{eff}},\frac{a}{\ell_{eff}}\right)\cdot k_BT\rho(E^*)\ln 10. \tag{7.11}$$

N is the total number of nanoparticles. The factor of ln10 arises because the data were fitted to a logarithm base 10 rather than a natural logarithm.

Equation (7.11) allows one to convert from flux relaxation amplitude Φ_s to number of bound nanoparticles N. Unfortunately, the factor $\rho(E^*)$, the anisotropy energy distribution density for the ensemble of nanoparticles evaluated at some "mean" anisotropy energy E^*, is not known precisely. Nevertheless, it is possible to make an educated estimate from the knowledge that the distribution is broad and is normalized to unity. The simplest assumption is that $\rho(E)$ is constant from the minimum energy E_{min} to the maximum energy E_{max} and zero everywhere else. Clearly, for the theory to make sense $E_{min} < E^* < E_{max}$,

so that $\rho(E^*) = 1/(E_{max} - E_{min})$ to be properly normalized. However, estimating these energies is difficult.

From Eq. (6.2), the anisotropy energy cutoffs each correspond to a Néel relaxation time: $E_{min} = k_B T \ln(\tau_N^{min}/\tau_N^{(0)})$ and $E_{max} = k_B T \ln(\tau_N^{max}/\tau_N^{(0)})$. Thus, $\rho(E^*) = 1/[k_B T \ln(\tau_N^{max}/\tau_N^{min})]$. It is easier to estimate these relaxation times. The measurement window in this experiment was $1s$ long, with a sampling rate of 400Hz. Thus, I conservatively estimate that we can resolve temporal features as fast as 2.5ms, and as slow as 1s. These times correspond to $\rho(E^*) \approx 1/6k_BT$. Because this factor depends weakly on my choice of relaxation times, even if I underestimate by several orders of magnitude I expect $\rho(E^*) \sim 1/10k_BT$.

Summarizing, the dipole moment m is $3 \times 10^{-18} A \cdot m^2$, the polarization factor $mB/3k_BT = 0.07$, $\ell_{eff}/a^2\mathcal{G}_y^{(2D)} \approx 2.6mm^{-1}$, and $k_BT\rho(E^*) \approx 0.1$. Substituting these values into Eq. (7.11), we obtain $\Phi_s/N \sim 6n\Phi_o$. Thus, our detection limit of $0.2m\Phi_o$ corresponds to $\sim 3 \times 10^4$ particles, in good agreement with the value from the TEM calibration. This theoretical calibration factor is displayed in Fig. 7.5 as the dotted line.

7.4 Discussion

7.4.1 Sensitivity

I have shown that we can detect magnetic particles selectively bound to a suitably chosen target, and that unbound particles contribute little or no signal. The experimentally determined detection limit is currently 5×10^4 magnetic particles. This corresponds to 5×10^4 targets if each is bound to a single magnetic particle, or fewer if multiple particles label each target. For instance, bacteria have thousands to millions of copies of its antigenic sites.

This detection limit is, to our knowledge, the best sensitivity yet achieved with this type of magnetic immunoassay. In comparison, similar magnetic immunoassays quote detection limits of more than 10^6 magnetic labels [57, 60]. In addition, the sensitivity and rapidity of the test compare favorably with other, more established methods. The most sensitive enzyme-linked immunosorbent assays (ELISA) are not capable of detecting fewer than 10^5 labeled antigens.

A substantial advantage of the MAgnetic Relaxation/remanence ImmunoAssay is that it can distinguish between bound and unbound magnetic labels [57]. As demonstrated

in our experiments, we are able to perform homogeneous assays, in which the labels are left in suspension together with the targets. This method obviates the need for time-consuming wash steps, which are necessary in most other techniques. Furthermore, only extremely small sample volumes are required. Although we used $30\mu L$ of nanoparticles in these experiments, the sample cell is so small that as little as $1\mu L$ of antibody-labeled nanoparticle suspension is sufficient. The sample film itself is only 0.2mm^2 in area. Small sample volumes are important in applications where materials are scarce or expensive, and allow one to concentrate target samples to a greater extent. The magnetic assay may also have advantages in its speed. Competing techniques often require days to grow cultures of the target organism, or time for amplification by other methods. In our technique, the rate limiting steps are the binding of targets to the substrate and antibody-linked nanoparticles to the target. In the future, we expect to reduce the time required for these steps significantly. The measurement itself takes only 200s, although for sufficiently large signals (where no averaging is necessary) the measurement time could in principle be as short as two seconds. In addition, the microscope can be configured in order to scan samples over the SQUID [4], allowing multiple samples to be measured and compared in one run.

7.4.2 Improvements

Four factors have been identified as limiting the sensitivity to the level achieved here. Work is already underway to improve the performance of the system. As mentioned, the background exponential decay in Fig. 7.1 is likely generated by eddy currents. While this contribution sets our detection limit at $0.2m\Phi_o$, the ultimate limit as determined by the noise in the SQUID is only $\sim 2\mu\Phi_o$ for 100 averages (the SQUID flux noise is $15\mu\Phi_o/\sqrt{Hz}$ and the effective measurement bandwidth, given by the spectral width of the decay signal, is ~ 2Hz). Thus, by eliminating the background decay completely, we would gain a factor of 100 in our detection limit for 100 averages. To reduce sources of eddy currents, Helene has designed and is currently constructing a second-generation SQUID microscope which has less metal near the SQUID. This new microscope will nevertheless have to be operated inside a μ-metal shield. To reduce contributions to the background from the shield, we hope to incorporate a cancellation scheme, as will be discussed below.

As seen in Eq. (7.11), the value of the magnetizing field B is important. For a dipole moment of $m = 3 \times 10^{-18} A \cdot m^2$ and a magnetizing field of $0.3mT$, the polarization

factor $mB/3k_BT$ is only 0.07, meaning that on average, nanoparticles are only 7% aligned to the field prior to it being removed. Joule heating prohibited us from passing more current into the coil to boost the magnetizing field. I have since built a new coil with a smaller diameter which can safely attain a field of $3mT$. This larger field increases the polarization factor to 0.6 for particles with the same moment. At this field, one can begin to observe the saturation of the magnetization of the nanoparticles. An added benefit of this new coil design is that, due to its smaller size, background relaxation signals have decreased by a factor of 10 for a field of $0.3mT$.

The magnetic coupling factor $\mathcal{G}_y^{(2D)}$ between the mylar film and the SQUID can be significantly improved. In the current configuration, a large fraction of the nanoparticles do not efficiently couple their magnetic flux to the SQUID. This is evident in the fact that the sensing area of the SQUID is an order of magnitude smaller than the area of the sample. For optimum coupling one needs the sensor area to be comparable with or greater than that of the sample. The coupling can be improved even further by cleverly designing the sensor to match the sample geometry, as described below.

As explained before and illustrated in Fig. 7.6(a), because the sample is magnetized in-plane, it is necessary to displace it laterally by half its length to a location where the perpendicular component of its field is maximum. As shown in Fig. 7.6(b), the perpendicular component of the field has the opposite sign at the other end of the sample. Thus, if it were possible to detect the flux at both ends of the sample and subtract them, one would get twice the signal. Fortunately, it is relatively straightforward to fabricate superconducting devices which can do this. A planar gradiometer, as the name implies, detects gradients in magnetic field, and consists of two superconducting loops inductively coupled in parallel to a SQUID. When a uniform field is applied [see Fig. 7.6(c)], the currents in each loop cancel out at the SQUID, thus generating zero response. In the presence of a field gradient, however, a net current flows through the SQUID generating a measurable flux [see Fig. 7.6(d)]. Such a device will shortly be fabricated. The improvement in coupling is somewhat offset by the increased flux noise of the device due to its large inductance. I estimate an improvement in signal-to-noise of 4.

An added benefit of the planar gradiometer design is that it inherently suppresses environmental sources of noise. Sources further to the detector than the sample generate fields that are much more uniform, and thus tend to be cancelled by the gradiometer. This feature could reduce the fields which produce the background relaxation signals observed

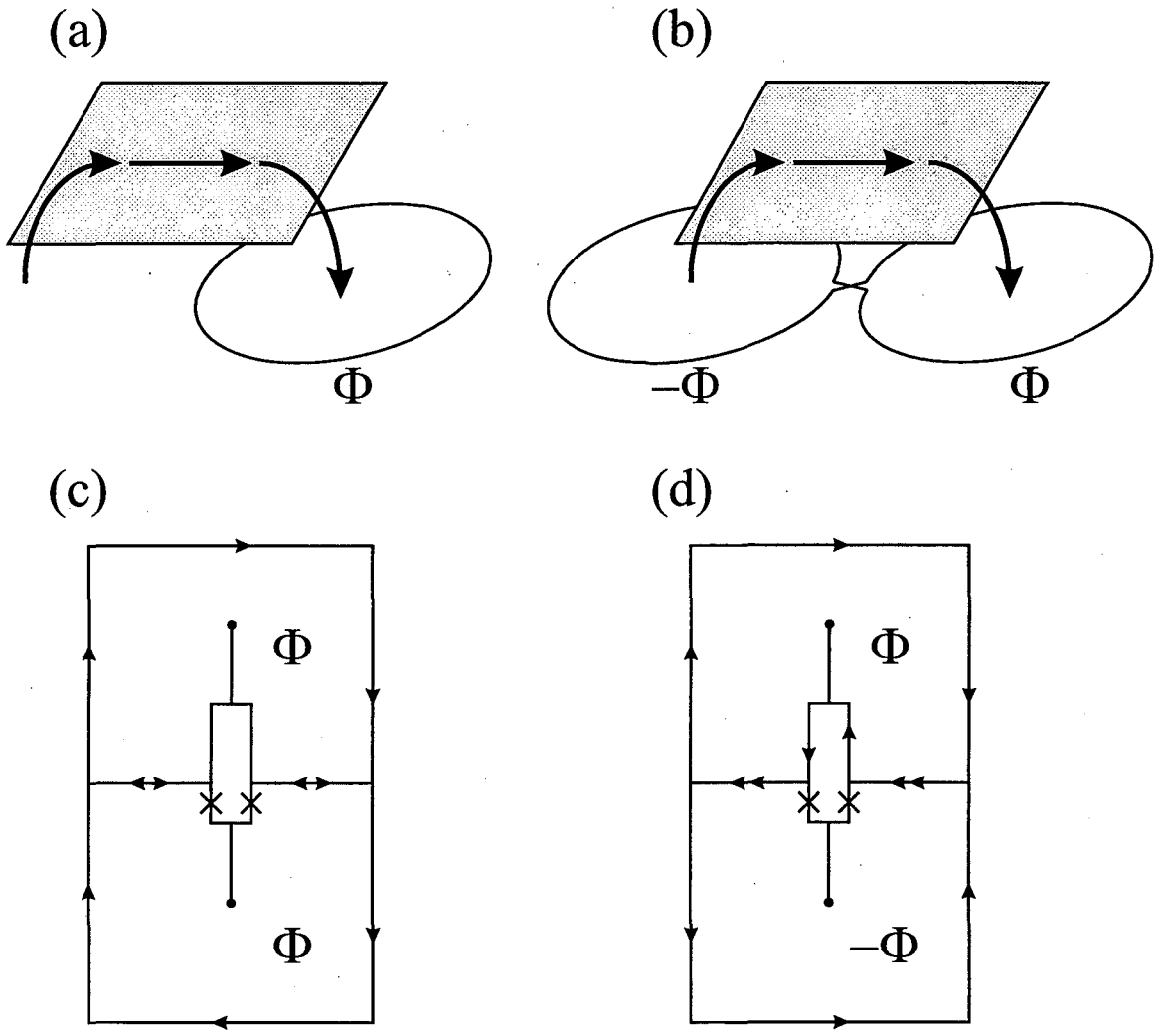

Figure 7.6: Increased coupling from a planar gradiometer. (a) A sample magnetized in-plane must be shifted laterally to couple flux into a SQUID. (b) The flux at one end of the sample is the opposite sign as that at the other end. By measuring the difference with a planar gradiometer, one detects twice the flux in (a). A planar gradiometer consists of two loops coupled to a SQUID. (c) A uniform magnetic field generates no flux inside the SQUID; (d) a gradient does.

in this experiment. Indeed, depending on the level of environmental noise rejection by the gradiometer, it may be possible to operate the SQUID microscope outside its μ-metal shield.

Finally, sensitivity is also limited by the dipole moment of the nanoparticles. As seen in Eq. (7.11), the signal scales as m^2 for low fields (near saturation, the signal scales as m). Advances in production techniques may yield superparamagnetic particles with larger moments for comparable or smaller sizes. A better production technique may also generate populations of nanoparticles with a much narrower and reproducible size distribution. As a result, $\rho(E^*)$, which scales as the inverse of the distribution width, could be increased boosting the signal further. A concerted effort is being made to manufacture nanoparticles of the desired properties here at Berkeley, in collaboration with Prof. Paul Alivisatos' laboratory in the Dept. of Chemistry.

The technique described here matches the versatility of existing immunoassay methods, while offering the potential to greatly improve upon their sensitivity. With the modifications outlined above, we expect to improve our detection limit to 50-500 magnetic particles. This can translate, perhaps, to the detection of a single target, if that target can, as expected, bind multiple labels.

Chapter 8

Conclusion

8.1 Future directions

In this thesis, I have presented two novel biological applications of the SQUID microscope. The experiments on magnetotactic bacteria described in Part I demonstrate the ability of the SQUID microscope to probe the dynamics of a live microorganism. The detection of a single bacterium—representing a dipole moment of $3 \times 10^{-16} A m^2$—swimming in an orbit demonstrates the extraordinary sensitivity of the device. As a logical extension of this result, I have argued that the microscope should, in principle, be able to detect the flux from a single magnetosome—a magnetite nanoparticle of diameter $\sim 35nm$ and moment $10^{-17} A \cdot m^2$. This sensitivity, coupled to a desire to extend this technique to non-magnetic biological samples, motivated me to pursue magnetic labeling methods. Part II described a magnetic immunoassay, based on a concept by Weitschies *et al.* [57] utilizing superparamagnetic nanoparticles coated with antibodies as labels. The model assay on liposomes containing the FLAG tag described in this thesis exhibited a sensitivity of 50000 labels, surpassing that of many standard immunoassays, including ELISA. Shortly, this technique will be improved to increase its sensitivity and will be extended to real biological pathogens, like the bacteria *Listeria monocytogenes*.

Two key results from these experiments—the ability to detect a small dipole moment, and the ability to magnetically label biological substances—point the way towards what I believe should be the next step in the evolution of the SQUID microscope. A recent exciting trend in the field of biophysics has been the development of techniques to probe the properties of biological molecules at the single molecule level. Optical tweezers, atomic

force microscopy (AFM), near-field scanning optical microscopy (NSOM), fluorescence resonance energy transfer (FRET), and many others enable one to push, pull, twist, and probe individual biomolecules. Already, single molecule biophysics has radically altered the way we look at biological macromolecules. The results described in this thesis suggest that the SQUID microscope has the potential to become a single molecule probe. Its utility, however, depends on two factors: whether it can match the sensitivity of current techniques, and whether it can answer questions that cannot be addressed by these methods.

One of the recurring themes in this thesis work has been that the SQUID microscope is much more sensitive to rotations than to translations of a dipole moment. This was in evidence in the measurements of the rotational Brownian motion of magnetotactic bacteria, the rotation of a single bacterium swimming in an orbit, or the rotation of the dipole moment of a nanoparticle due to Néel relaxation. Because the SQUID can only detect displacements by distances comparable to its relatively large size ℓ_{eff}, translations couple much less efficiently. In contrast, single molecule techniques are generally much more sensitive to translations than to rotations. For instance, translations as small as a few nanometers can easily be detected by optical tweezers. Rotations must be detected either by measuring the polarization of the light emitted by a fluorescent molecule, or by coupling the rotation to a displacement. For example, the rotary motor protein F_1-ATPase was studied by detecting the displacement of a long ($> 0.5\mu m$) actin filament attached to its rotary axis [66]. The drawback of such a method is that the probe is many times bigger than the molecule it is attached to, and the dynamics are entirely dominated by the drag on the probe. The appeal of a SQUID technique would be that such an experiment could be carried out with a much smaller magnetic nanoparticle. The complementarity of the SQUID to these techniques makes it an appealing alternative.

One advantage to using magnetic labels is that they can be manipulated using magnetic fields and field gradients. Strick *et al.* [67] used a rotating permanent magnet to pull and twist a strand of DNA labeled with a superparamagnetic bead. One end was attached to a glass cover slip by an antibody, the other end was labeled with biotin and attached to the streptavidin-coated magnetic bead[1]. The authors determined the restoring force of the DNA as a function of its twist by measuring the displacement of the bead. One could imagine a similar SQUID experiment in which the rotation of the magnetic bead is

[1]Biotin binds very strongly to the proteins avidin and streptavidin. It is the strongest non-covalent interaction found in biology.

measured directly. In this way, it would appear possible to determine the restoring torque of the DNA strand, a quantity the authors were unable to measure. The mechanical properties of DNA are an important determinant in how it is compactified inside the chromosome, and a current area of study.

8.2 Attaining single nanoparticle sensitivity

I believe such an experiment would be one in which the SQUID microscope could greatly contribute. The remaining issue is whether the microscope can indeed achieve a sensitivity of one magnetic nanoparticle. Again, the observation of single bacterium orbits with ample signal-to-noise suggests that it is. The answer clearly depends on the magnetic nanoparticle used. In such an application, the requirements for the nanoparticles are very different than in the immunoassay. There is no need to distinguish between bound and unbound particles, since the molecule is labeled with the magnetic particle prior to the experiment. Rather, one wishes to maximize the dipole moment.

The dipole moment of a single magnetotactic bacterium $3\times10^{-16}A\cdot m^2$—a moment we know we can detect—corresponds to a single-domain magnetite nanoparticle of diameter $\sim 100nm$. Ferromagnetic nanoparticles with a diameter much larger than $\sim 30nm$ are difficult to synthesize in the laboratory, as they tend to form aggregates due to magnetic interactions. Furthermore, particles larger than $\gtrsim 120nm$ tend to form multiple domains. Superparamagnetic particles synthesized in the laboratory, consisting of multiple domains or aggregates of smaller particles, may reach sizes up to several microns. When magnetized to saturation, they can possess a large dipole moment[2]. However, once magnetized they undergo Néel relaxation. Nevertheless, this may not be an issue if the dynamics that are probed are faster than the Néel relaxation process.

The most obvious—and ideal—solution is to use the magnetosomes from magnetotactic bacteria directly. They are single-domain, permanently magnetic with a moment $\sim10^{-17}A\cdot m^2$, and come enveloped in their own biological membrane, making the conjugation of chemical groups easy. Nakamura *et al.* [68] have had success in extracting bacterial magnetosomes for use as immunological labels in magnetic separation assays. The difficulty lies in breaking up the magnetosome chain, which is held together by strong magnetic

[2]Strick *et al.* [67] used a $2.8\mu m$ superparamagnetic bead (Dynal, M280) with a vendor-specified susceptibility $\chi = M/H \approx 0.13$, corresponding to a dipole moment of $3.6\times10^{-16}A\cdot m^2$ in a $0.3mT$ magnetizing field.

interactions. The yield of their process also appears to be low.

For the sake of argument, I will assume that ferromagnetic or superparamagnetic nanoparticles with a "canonical" dipole moment of $10^{-17} A \cdot m^2$ are available. Recalling the discussion of Section 3.3.1, I calculated that such a dipole moment would produce a maximum flux of $80\mu\Phi_o$ into a SQUID with $\ell_{eff} = 40\mu m$, $z_o = 15\mu m$ away, parameters representing optimal coupling. If the dipole rotates 360° at some frequency with a spectral width of 1Hz, and the intrinsic SQUID noise at that frequency is $10\mu\Phi_o/\sqrt{Hz}$, then the signal-to-noise is 16, with no signal averaging. This result suggests that there is ample room to achieve one-particle sensitivity. However, since the flux decreases rather dramatically as the particle is moved away from the SQUID, this is only provided one can guarantee optimal coupling.

Thus, the real issue is not the sensitivity, but ensuring that the coupling between the nanoparticle and the SQUID is maximized. After all, the microscope was able to detect individual bacteria, but only on the rare occasion that one passed over the SQUID sensing area. One solution would be to scan the sample cell over the SQUID until a nanoparticle is found. However, this may be time-consuming, and ensuring that a SQUID-sample separation of $15\mu m$ is maintained throughout the scan may be technically challenging. Another would be to equip the SQUID microscope with a powerful optical objective with which to view the sample cell and locate nanoparticles (which could be fluorescently labeled). The sample cell could then be displaced to position the nanoparticle over the SQUID.

An appealing alternate to these solutions would be to integrate optical tweezers with the SQUID microscope. The advantage of such an apparatus would be the ability to manipulate the molecules and probes of interest. For instance, a magnetic nanoparticle attached to a DNA strand could be trapped by the optical tweezers and placed directly over the SQUID, in a region of optimal coupling. Since the tweezers do not apply a torque, the particle would be free to rotate. The integration of optical tweezers with the SQUID microscope would only require an objective and a low-power laser. Furthermore, the optical trap could be used in parallel with the SQUID to measure displacements of the magnetic bead. The correlation of its translation and rotation in the trap in response to the forces and torques generated by the DNA would make an interesting measurement. The complementarity of the SQUID to single molecule techniques suggests merging the two technologies together. I believe such "two-probe" systems (magnetic and optical) could make the SQUID microscope a useful biological tool.

Appendix A

The flux transfer function

A.1 Introduction

The measurements described in this thesis all involve detecting a magnetic dipole (or a distribution of dipoles) with a SQUID in close proximity. In order to correctly interpret these measurements it is necessary to derive a "flux transfer function" which determines the flux threading the SQUID due to a single dipole a certain distance away. To calculate the flux from a distribution of dipoles, I simply integrate the flux transfer function over that distribution.

Quite generally, the magnetic flux from a source a distance $\mathbf{r}$ away is given by an integral of the source field $\mathbf{B}$ over the SQUID area S:

$$\Phi(\mathbf{r}) = \int_S \mathbf{B}(\mathbf{r} - \mathbf{r}') \cdot \hat{\mathbf{n}}\, dA'. \tag{A.1}$$

For a uniform magnetic field the flux reduces to $\Phi = B \cdot A_{eff}$. This expression is sufficient to model sources in the "far field limit," where B is slowly-varying over the SQUID area S. However, in the "near field," it is necessary to carry out the integration above explicitly. Roughly speaking, the crossover between the two regimes occurs when the source is a distance of order $(A_{eff})^{1/2}$ away from the SQUID. The applications of the SQUID microscope in this thesis involve SQUID-sample separations either equal to or smaller than this length scale, so an expression for the flux transfer function in the near-field limit is clearly needed.

A.2 Point dipole sources

The simplest approach to this problem is to model the SQUID as a square pickup loop of side $\ell_{eff} = (A_{eff})^{1/2}$. Even though this completely ignores the exact geometry of the SQUID washer and effects such as flux focusing from the superconducting film, it proves to be quite adequate for our purposes. Thus, consider a square loop of side ℓ_{eff} centered at the origin of the "SQUID" reference frame as drawn in Fig. A.1. A dipole m is oriented at angles θ, ϕ and is located a distance $\mathbf{r}$ from the origin. The flux $\Phi(\mathbf{r}, \theta, \phi, \ell_{eff})$ threading the SQUID is given by,

$$\Phi(\mathbf{r}, \theta, \phi, \ell_{eff}) = \int_{-\ell_{eff}/2}^{\ell_{eff}/2} dx' \int_{-\ell_{eff}/2}^{\ell_{eff}/2} dy'\, B_z(x - x', y - y', z, \theta, \phi), \tag{A.2}$$

where B_z is given by,

$$B_z(x, y, z, \theta, \phi) = \frac{\mu_o m}{4\pi} \left\{ \left(-\frac{1}{r^3} + \frac{3z^2}{r^5} \right) \cos\theta + \left(\frac{3xz}{r^5} \right) \sin\theta \cos\phi + \left(\frac{3yz}{r^5} \right) \sin\theta \sin\phi \right\}, \tag{A.3}$$

and $r^2 = x^2 + y^2 + z^2$.

The integral (A.2) is lengthy but may be solved analytically. The result is

$$\Phi(x, y, z, \theta, \phi, \ell_{eff}) = \Phi_z \cos\theta + \Phi_x \sin\theta \cos\phi + \Phi_y \sin\theta \sin\phi \tag{A.4}$$

where the functions Φ_z, Φ_x, Φ_y are defined as

$$\begin{aligned} \Phi_i(x, y, z, \ell_{eff}) \;=\; & \frac{\mu_o m}{4\pi} \left\{ g_i\left(x - \frac{\ell_{eff}}{2}, y - \frac{\ell_{eff}}{2}, z \right) - g_i\left(x + \frac{\ell_{eff}}{2}, y - \frac{\ell_{eff}}{2}, z \right) \right. \\ & \left. - g_i\left(x - \frac{\ell_{eff}}{2}, y + \frac{\ell_{eff}}{2}, z \right) + g_i\left(x + \frac{\ell_{eff}}{2}, y + \frac{\ell_{eff}}{2}, z \right) \right\} \end{aligned} \tag{A.5}$$

for $i = x, y, z$, and g_z, g_x, g_y are given by

$$\begin{aligned} g_z(x, y, z) &= \frac{1}{x^2 + z^2} \frac{xy}{\sqrt{x^2 + y^2 + z^2}} + \frac{1}{y^2 + z^2} \frac{xy}{\sqrt{x^2 + y^2 + z^2}} \\ g_x(x, y, z) &= \frac{1}{x^2 + z^2} \frac{yz}{\sqrt{x^2 + y^2 + z^2}} \\ g_y(x, y, z) &= \frac{1}{y^2 + z^2} \frac{xz}{\sqrt{x^2 + y^2 + z^2}}. \end{aligned} \tag{A.6}$$

The functions Φ_z, Φ_x, Φ_y describe the contributions to the flux from a single dipole oriented along the $\hat{z}$-, $\hat{x}$-, and $\hat{y}$-axes, respectively.

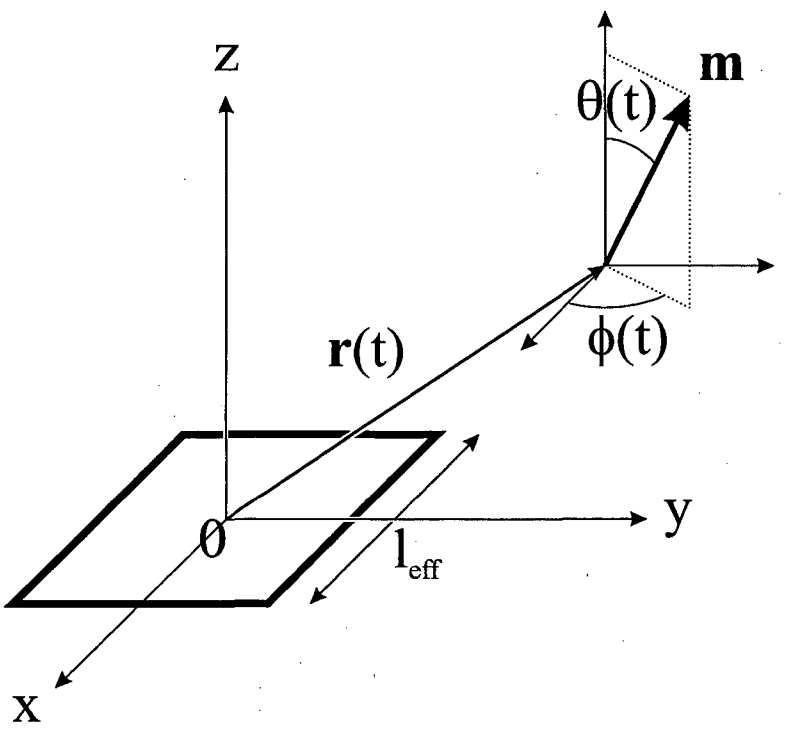

Figure A.1: SQUID reference frame. The SQUID is modeled as a square pickup loop of length $\ell_{eff} = (A_{eff})^{1/2}$ and centered on the origin of the reference frame. The $\hat{z}$-axis is defined normal to the SQUID, the $\hat{x}$- and $\hat{y}$-axes in the plane. A point dipole of moment m is located a distance $\mathbf{r}(t)$ from the origin, and is oriented at angles $\theta(t)$ and $\phi(t)$.

The above expressions are quite cumbersome. It is sometimes more convenient to express the flux transfer function in Fourier space (for example, see Appendix C). Equation (A.2) can be seen as a convolution of the field and a windowing function equal to unity for $|x|, |y| < \ell_{eff}/2$ and zero everywhere else. Taking the spatial Fourier transform in x and y is straightforward:

$$\begin{aligned}
\tilde{\Phi}_z(k_x, k_y, z, \ell_{eff}) &= \frac{\mu_o m}{4\pi} \ell_{eff}^2 \left[\frac{\sin(k_x \ell_{eff}/2)}{k_x \ell_{eff}/2}\right] \left[\frac{\sin(k_y \ell_{eff}/2)}{k_y \ell_{eff}/2}\right] k e^{-k|z|} \\
\tilde{\Phi}_x(k_x, k_y, z, \ell_{eff}) &= \frac{\mu_o m}{4\pi} \ell_{eff}^2 \left[\frac{\sin(k_x \ell_{eff}/2)}{k_x \ell_{eff}/2}\right] \left[\frac{\sin(k_y \ell_{eff}/2)}{k_y \ell_{eff}/2}\right] i k_x e^{-k|z|} \\
\tilde{\Phi}_y(k_x, k_y, z, \ell_{eff}) &= \frac{\mu_o m}{4\pi} \ell_{eff}^2 \left[\frac{\sin(k_x \ell_{eff}/2)}{k_x \ell_{eff}/2}\right] \left[\frac{\sin(k_y \ell_{eff}/2)}{k_y \ell_{eff}/2}\right] i k_y e^{-k|z|}
\end{aligned} \tag{A.7}$$

with $k \equiv \sqrt{k_x^2 + k_y^2}$. Note that the functions are sharply peaked in the region $|k_x|, |k_y| < 1/\ell_{eff}$.

A.3 Distributions of dipoles

For a sample which consists of a distribution of dipoles, it is necessary to integrate Eq. (A.5) over the distribution. For instance, in Section 5.2.1 I calculate the flux noise power spectrum due to an ensemble of magnetotactic bacteria with density $\rho_b(\mathbf{r})$. The coupling of flux noise from the bacteria to the SQUID is described by a noise spectrum geometrical factor $\mathcal{G}_i^{(s)}$

$$\mathcal{G}_i^{(s)} = \int d^3\mathbf{r}\, \rho_b(\mathbf{r}) \Phi_i^2(\mathbf{r}, \ell_{eff}), \tag{A.8}$$

with $i = x, y, z$. This integral can be carried out numerically for a given sample size and cell density. One simplification is to assume a uniform distribution ρ_b, another is to assume an infinitely large sample. Since the flux from a dipole infinitely far away is vanishingly small, this does not introduce a significant error. Thus we can write

$$\mathcal{G}_i^{(s)} = \int_{-\infty}^{\infty} dx \int_{-\infty}^{\infty} dy \int_{z_o}^{\infty} dz\, \rho_b \Phi_i^2(x, y, z, \ell_{eff}) = \left(\frac{\mu_o m}{4\pi}\right)^2 \rho_b \ell_{eff} \cdot g^{(s)}\left(\frac{z_o}{\ell_{eff}}\right), \tag{A.9}$$

where z_o is the SQUID-sample separation[1]. The last equation is written so as to clarify the dependences of $\mathcal{G}_i^{(s)}$ on the many variables at play; the bacteria parameters m and ρ_b are on

[1]One can write this expression in Fourier space as well. From Parseval's theorem $\mathcal{G}_i^{(s)} = \int d^3\mathbf{r}\, \Phi_i^2(\mathbf{r}) = (2\pi)^{-2} \int dz \int d^2\mathbf{k}\, |\tilde{\Phi}_i(\mathbf{k}, z)|^2$. From this and Eq. (A.7), it should be evident that $\mathcal{G}_z^{(s)} = 2\mathcal{G}_x^{(s)} = 2\mathcal{G}_y^{(s)}$.

one side, the SQUID parameters ℓ_{eff} and z_o on the other. The function $g^{(s)}$ is dimensionless and depends only on the ratio z_o/ℓ_{eff}. It is a "universal" geometrical factor in the sense that noise data from different SQUIDs with different SQUID-sample separations should all fall on the same curve.

In Section 5.2.2 I calculate the response from an ensemble of bacteria to an applied magnetic field along the $\hat{y}$-axis. There, the coupling is described by a response function geometrical factor $\mathcal{G}_y^{(r)}$

$$\mathcal{G}_y^{(r)} = \int_{-\infty}^{\infty} dx \int_0^{\infty} dy \int_{z_o}^{\infty} dz\, \rho_b \Phi_y(x,y,z,\ell_{eff}) = \frac{\mu_o m}{4\pi} \rho_b \ell_{eff}^2 \cdot g^{(r)}\left(\frac{z_o}{\ell_{eff}}\right). \qquad \text{(A.10)}$$

As above, I assume that the cell density is uniform and the sample is infinitely large. However, as explained in Section 5.2.2, the SQUID is offset in the y direction to maximize coupling (Φ_y is odd in y. If there were no offset, $\mathcal{G}_y^{(r)}$ would be zero). The offset is about half the SiN sample well length, so that the center of the SQUID is at the edge of the well. To account for the offset, the limits of integration in y are set at 0 to ∞. Again, $\mathcal{G}_y^{(r)}$ can also be written in terms of a universal, dimensionless function $g^{(r)}$.

In Section 7.3.2 I calculate the relaxation from a $440\times440\mu m$ sheet of magnetite nanoparticles, uniformly distributed with a surface density σ_m. The geometrical factor for a sample of dimension a is

$$\mathcal{G}_y^{(2D)} = \int_{-a/2}^{a/2} dx \int_0^{a} dy\, \sigma_m \Phi_y(x,y,z,\ell_{eff}) = \frac{\mu_o m}{4\pi} \sigma_m \ell_{eff} \cdot g^{(2D)}\left(\frac{z_o}{\ell_{eff}}, \frac{a}{\ell_{eff}}\right). \qquad \text{(A.11)}$$

The three universal geometrical functions defined above are plotted in Figs. A.2(a)-(c). Where available, I included data points from actual SQUID measurements, which fit remarkably well.

A.4 Sampling volume

It is clear from the expressions calculated above that dipoles far away from the SQUID contribute a very small flux compared to dipoles close to it. Thus, for a sample which consists of a distribution of dipoles over some large volume, the SQUID only detects a small fraction in its vicinity. The so-called "sampling volume" of the SQUID may be calculated using the expressions derived above.

Consider a cube of side s uniformly magnetized with a dipole moment density ρ_b

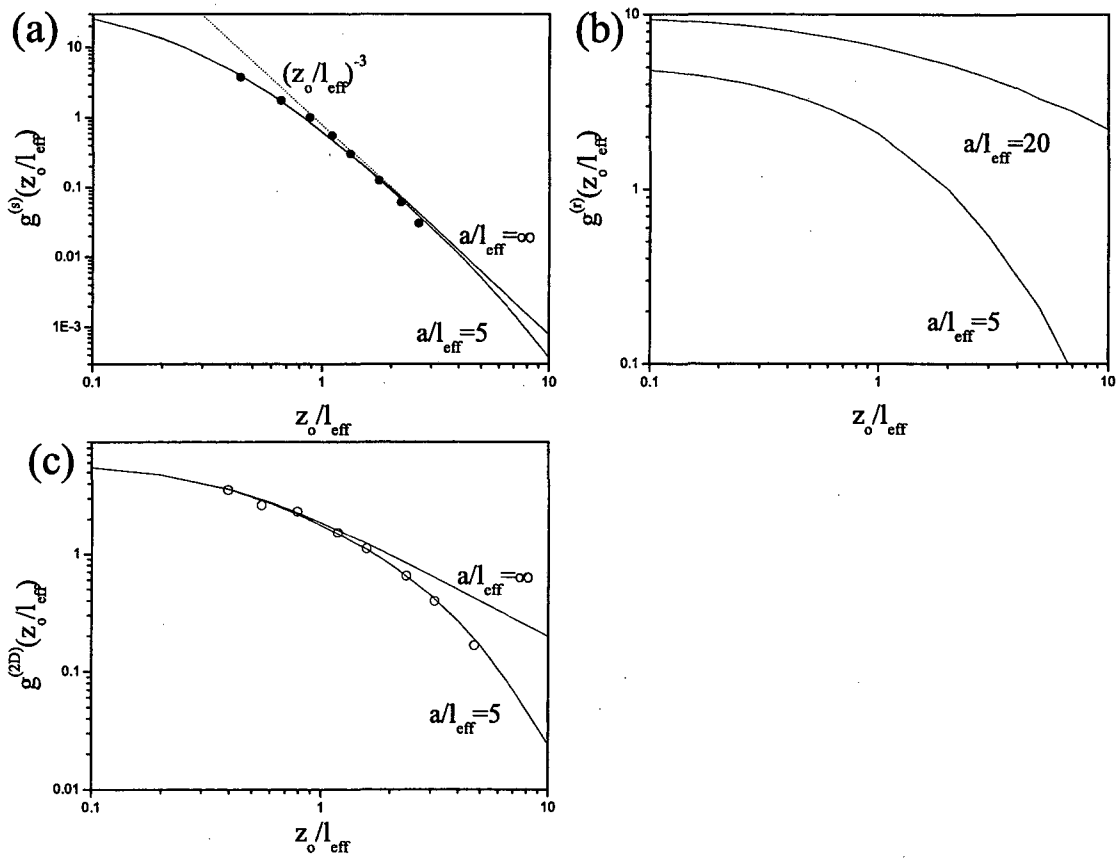

Figure A.2: Geometrical factors $g^{(s)}$ for noise measurements (a), $g^{(r)}$ for response function measurements (b), and $g^{(2D)}$ from a 2D sheet of dipoles (c) as a function of z_o/ℓ_{eff}. Data from two SQUIDs: slit A-C type (filled circles) and slit A-A type (open circles) included where available. Deviations from the curve for large z_o may be due to finite sample size.

a minimum distance z_o away from a SQUID. The flux is given by

$$\mathcal{G}_z^{(r)}(s, z_o, \ell_{eff}) = \int_{-s/2}^{s/2} dx \int_{-s/2}^{s/2} dy \int_{z_o}^{s+z_o} dz\, \rho_b \Phi_z(x, y, z, \ell_{eff}). \tag{A.12}$$

The ratio of this flux for a sample of finite size s to that for a sample of infinite size,

$$\frac{\mathcal{G}_z^{(r)}(s, z_o, \ell_{eff})}{\mathcal{G}_z^{(r)}(\infty, z_o, \ell_{eff})} = \frac{g^{(r)}(s/\ell_{eff}, z_o/\ell_{eff})}{g^{(r)}(\infty, z_o/\ell_{eff})} \tag{A.13}$$

saturates to unity as s increases as shown in Fig. A.3. The point at which this ratio begins to saturate corresponds to the sampling volume.

Defining the saturation point is a little arbitrary; the dotted lines in the plot indicate 90% and 95% saturation. Note that the sampling volume also depends on the separation z_o. Although the absolute flux through the SQUID clearly decreases as z_o increases, it is generated from a proportionately larger volume (the curves in Fig. A.3 are normalized so that the decrease in absolute flux with increasing z_o is not shown). Loosely speaking, the SQUID "sees" a volume which extends out like a cone from its center, with regions near the point of the cone contributing more than regions further out.

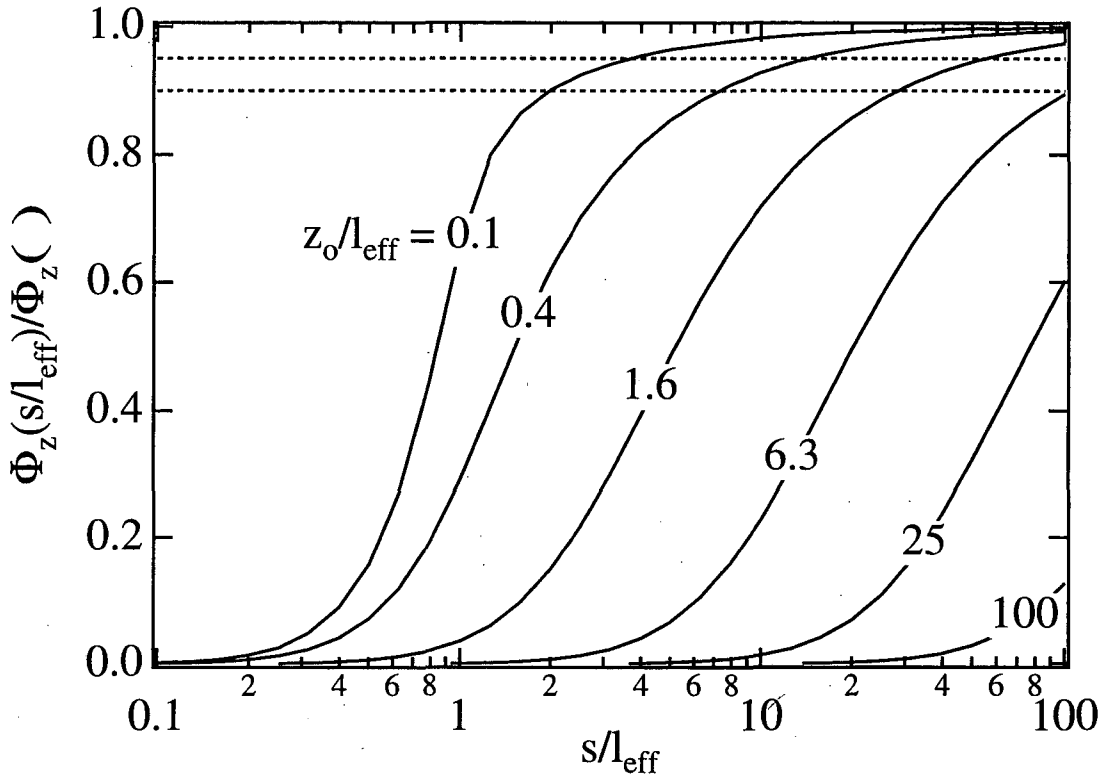

Figure A.3: Sampling volume of a SQUID. The ratio of the flux from a sample of size s to the flux from a sample of infinite size is plotted against s/ℓ_{eff} for several various SQUID-sample separations z_o/ℓ_{eff} (ℓ_{eff} is fixed). The ratio saturates to unity when the sample size is the sampling volume of the SQUID. The two dotted lines indicate 90% and 95% saturation.

Appendix B

Calculations of Autocorrelation and Response Function

B.1 The Fokker-Planck equation

Microorganisms exist in a world very different from ours. Due to their small size, inertial forces are much smaller than viscous forces (a regime known as the low-Reynolds number regime. The Reynolds number is a dimensionless ratio of inertial to viscous forces) [69]. Life in the microscopic universe is also subject to fluctuations much more than in the macroscopic world. Thus a formalism which takes into account the Brownian nature of the motion is needed to model the dynamics of microorganisms. Generally there are two approaches to this problem: the Langevin equation, a Newton equation of motion for the fluctuating variables $\{q(t)\}$ which includes a fluctuating force $\mathcal{F}(t)$; and the Fokker-Planck equation, a diffusion-like equation for the probability density associated with those variables, $W(\{q\},t)$. For most processes these two approaches are equivalent [70].

In this thesis I adopt the latter formalism since it turns out to be very convenient and powerful for the quantities I need to calculate. In our experiments we either measured the flux response function $\langle\Phi(t)\rangle$ or the flux autocorrelation function $C_\Phi(t) = \langle\Delta\Phi(t)\Delta\Phi(0)\rangle$. Consider Ψ, a function of a set of dynamical variables $\{q(t)\}$, i.e. $\Psi(t) = \Psi(\{q(t)\})$. In the case of the bacteria, for example, the function can be the flux, which depends on the positions $\mathbf{r}(t)$ and orientations $\theta(t)$, $\phi(t)$ of the dipole moments of each cell.

In the Fokker-Planck formalism the response function is given by

$$\langle \Psi(t) \rangle = \int \{dq\} W_1(\{q\}, t) \Psi(\{q\}), \tag{B.1}$$

where W_1 is the probability that the dynamical variables equal $\{q\}$ at time t. W_1 satisfies a Fokker-Planck equation specific to the dynamics exhibited by the variables $\{q\}$.

The autocorrelation function for Ψ can also be formulated in the context of the Fokker-Planck equation; C_Ψ can be written as

$$\begin{aligned} C_\Psi(t) &\equiv \langle \Delta\Psi(t) \Delta\Psi(0) \rangle = \langle (\Psi(t) - \langle \Psi(t) \rangle) \cdot (\Psi(0) - \langle \Psi(0) \rangle) \rangle \\ &= \langle \Psi(t)\Psi(0) \rangle - \langle \Psi(t) \rangle \langle \Psi(0) \rangle. \end{aligned} \tag{B.2}$$

Note that at $t = 0$, C_Ψ is equal to the variance of Ψ. The second line in Eq. (B.2) consists of two terms; the second can be calculated from Eq. (B.1), the first from

$$\langle \Psi(t)\Psi(0) \rangle = \int \{dq\} \int \{dq_o\}\, W_2(\{q\}, t; \{q_o\}, 0) \Psi(\{q\}) \Psi(\{q_o\}) \tag{B.3}$$

where W_2, the *joint probability density*, is the probability that at time t the dynamical variables are equal to $\{q\}$ *and* that at time 0 they are equal to $\{q_o\}$. W_2 is related to the *transition* or *conditional probability density* $P(\{q\}, t|\{q_o\}, 0)$, the probability that *if* the dynamical variables equal $\{q_o\}$ at time 0, they will equal $\{q\}$ at a later time t [70]:

$$\begin{aligned} W_2(\{q\}, t; \{q_o\}, 0) &= P(\{q\}, t|\{q_o\}, 0) \cdot W_{st}(\{q_o\}) \quad \text{for } t \geq 0 \\ &= P(\{q_o\}, -t|\{q\}, 0) \cdot W_{st}(\{q\}) \quad \text{for } t \leq 0. \end{aligned} \tag{B.4}$$

W_{st} is the stationary, or equilibrium, probability distribution. Note that the initial conditions for $P(\{q\}, t|\{q_o\}, 0)$ must be a delta function:

$$P(\{q\}, 0|\{q_o\}, 0) = \delta(\{q\} - \{q_o\}). \tag{B.5}$$

Thus one can think of the transition probability density P as the Green's function of the Fokker-Planck equation.

Equation (B.4) gives an expression relating the joint probability distribution W_2 to the transition probability density P. The probability W_1 introduced in Eq. (B.1) can also be written in terms of P:

$$\begin{aligned} W_1(\{q\}, t) &= \int \{dq_o\}\, W_2(\{q\}, t; \{q_o\}, 0) \\ &= \int \{dq_o\}\, P(\{q\}, t|\{q_o\}, 0) \cdot W_{st}(\{q_o\}). \end{aligned} \tag{B.6}$$

Therefore, the transition probability density P can be used to calculate all of the quantities of interest in our experiments: the flux autocorrelation function and the flux response function.

B.2 Rotational Brownian motion

B.2.1 Autocorrelation function

In Section 5.2.1 I argued that the dynamics of non-motile magnetotactic bacteria are dominated by rotational Brownian motion. The motion of the cells—specifically, their dipole moments, since that is what is detected by the SQUID—is equivalent to that of a particle moving in a random walk on the surface of a unit sphere. As mentioned above, inertial forces are so small that they may be ignored entirely in this analysis. The dynamical variables are the angles $\theta(t)$ and $\phi(t)$ which describe the orientation of the dipole moments with respect to the SQUID. The Fokker-Planck equation describing this process is given by a diffusion equation involving the angular part of the Laplacian ∇^2:

$$\frac{\partial W}{\partial t} = D_r \left(\frac{1}{\sin\theta} \frac{\partial}{\partial \theta} \sin\theta \frac{\partial W}{\partial \theta} + \frac{1}{\sin^2\theta} \frac{\partial^2 W}{\partial \phi^2} \right). \tag{B.7}$$

D_r is the rotational diffusion coefficient, given by $k_B T/\alpha_r$, where α_r is the rotational drag coefficient.

Solutions of Eq. (B.7) can be written as linear combinations of the spherical harmonics $Y_{\ell m}(\theta, \phi)$. The transition probability density $P(\theta, \phi, t|\theta_o, \phi_o, 0)$ which solves this Fokker-Planck equation is given by

$$P(\theta, \phi, t|\theta_o, \phi_o, 0) = \sum_{\ell=0}^{\infty} \sum_{m=-\ell}^{\ell} Y^*_{\ell m}(\theta_o, \phi_o) Y_{\ell m}(\theta, \phi) e^{-\ell(\ell+1)D_r t} \tag{B.8}$$

which has the correct initial condition [19]

$$P(\theta, \phi, 0|\theta_o, \phi_o, 0) = \frac{1}{\sin\theta} \delta(\theta - \theta_o)\delta(\phi - \phi_o). \tag{B.9}$$

Using Eq. (B.4) I can calculate the joint probability density. The stationary probability distribution W_{st} is just the probability that the orientation angles θ, ϕ take on any value in 4π of solid angle; $W_{st} = 1/4\pi$, and

$$W_2(\Omega, t; \Omega_o, 0) = \frac{1}{4\pi} \sum_{\ell=0}^{\infty} \sum_{m=-\ell}^{\ell} Y^*_{\ell m}(\Omega_o) Y_{\ell m}(\Omega) e^{-\ell(\ell+1)D_r|t|}, \tag{B.10}$$

where $\Omega = \{\theta, \phi\}$.

As shown in Appendix A and discussed in Section 5.2.1, the flux $\Phi(t)$ from a dipole is a linear combination of the angular factors $\cos\theta$, $\sin\theta\cos\phi$, and $\sin\theta\sin\phi$ [see Eq. (5.4)]. Thus, the flux autocorrelation function $C_\Phi(t) \equiv \langle\Delta\Phi(t)\Delta\Phi(0)\rangle$ consists of angular autocorrelation functions like $\langle\cos\theta(t)\cos\theta(0)\rangle$, etc. which can be calculated using Eqs. (B.3) and (B.10). For instance

$$\langle\cos\theta\cos\theta_o\rangle = \frac{1}{4\pi}\sum_{\ell,m} e^{-\ell(\ell+1)D_r|t|} \cdot \underbrace{\int_0^\pi \sin\theta d\theta \int_0^{2\pi} d\phi\, \cos\theta\, Y_{\ell m}(\theta,\phi)}_{\sqrt{\frac{4\pi}{3}}\delta_{\ell,1}\delta_{m,0}} \cdot \underbrace{\int_0^\pi \sin\theta_o d\theta_o \int_0^{2\pi} d\phi_o\, \cos\theta_o\, Y^*_{\ell m}(\theta_o,\phi_o)}_{\sqrt{\frac{4\pi}{3}}\delta_{\ell,1}\delta_{m,0}}$$
$$= \frac{1}{3}e^{-2D_r|t|}. \tag{B.11}$$

The great advantage in expressing W_2 in terms of spherical harmonics $Y_{\ell,m}$ is that the three angular factors are themselves expressible in terms of spherical harmonics:

$$\cos\theta = \sqrt{\frac{4\pi}{3}}Y_{1,0}, \quad \sin\theta\cos\phi = \sqrt{\frac{2\pi}{3}}(-Y_{1,1} + Y_{1,-1}), \quad \sin\theta\sin\phi = \sqrt{\frac{2\pi}{3}}i(Y_{1,1} + Y_{1,-1}). \tag{B.12}$$

The orthonormality of spherical harmonics makes the evaluation of integrals like (B.11) trivial. It is a simple exercise to calculate

$$\langle\sin\theta\cos\phi\sin\theta_o\cos\phi_o\rangle = \langle\sin\theta\sin\phi\sin\theta_o\sin\phi_o\rangle = \frac{1}{3}e^{-2D_r|t|}. \tag{B.13}$$

Furthermore, all cross-terms must identically go to zero, since they consist of pairs of orthogonal spherical harmonics.

B.2.2 Response function

In the measurements described in Section 5.2.2, a magnetic field aligned the bacteria. At time $t = 0$, it was turned off and the cells reoriented themselves at random. This relaxation process is described by the response function $\langle\Phi(t)\rangle$, which I will calculate from the probability distribution W_1 as outlined above.

It is convenient to define the coordinate axes such that the magnetic field lies along the $\hat{z}$-axis. Thus, the angle between a cell's dipole moment $\mathbf{m}$ and the field $\mathbf{B}$ is θ. I assume

that prior to turning off the field ($t \leq 0$) the bacteria have reached equilibrium with the aligning field. Thus, the stationary probability distribution W_{st} of the orientation of the cells is now (see Section 4.2.2)

$$W_{st}(\theta, \phi) = \frac{\xi}{4\pi \sinh \xi} e^{\xi \cos\theta} \tag{B.14}$$

with $\xi \equiv mB/k_BT$. The factor preceding the Boltzmann factor normalizes the distribution.

For $t \geq 0$, the field is zero, and the Fokker-Planck equation (B.7) is still valid. Thus, using Eqs. (B.6) and (B.14) I calculate the probability distribution W_1. After some algebra, I find

$$\begin{aligned} W_1(\theta, \phi, t) &= \sum_{\ell,m} \int d\Omega_o \, Y^*_{\ell m}(\Omega_o) Y_{\ell m}(\Omega) e^{-\ell(\ell+1)D_r t} \frac{\xi}{4\pi \sinh \xi} e^{\xi \cos\theta_o} \\ &= \sum_{\ell=0}^{\infty} \sqrt{\frac{2\ell+1}{4\pi}} \frac{i_\ell(\xi)}{i_0(\xi)} Y_{\ell 0}(\theta, \phi) e^{-\ell(\ell+1)D_r t}, \end{aligned} \tag{B.15}$$

where the functions $i_\ell(\xi)$ are modified spherical Bessel functions of order ℓ [71] of the argument $\xi \equiv mB/k_BT$ (for instance, $i_0(\xi) = \sinh\xi/\xi$, $i_1(\xi) = \cosh\xi/\xi - \sinh\xi/\xi^2$, $\cdots$). From there, it is again a simple matter to calculate the flux response $\langle \Phi(t) \rangle$ from the standard angular factors $\cos\theta$, $\sin\theta\cos\phi$, and $\sin\theta\sin\phi$:

$$\langle \cos\theta(t) \rangle = \frac{i_1(\xi)}{i_0(\xi)} e^{-2D_r t} = L(\xi) e^{-2D_r t}. \tag{B.16}$$

Note that I recover the Langevin function $L(\xi) \equiv \coth\xi - 1/\xi$. This must necessarily be so, since at $t = 0$ Eq. (B.16) must agree with Eq. (4.1). The other angular response functions are zero, $\langle \sin\theta(t)\cos\phi(t) \rangle = \langle \sin\theta(t)\sin\phi(t) \rangle = 0$, since they are orthogonal to the field.

B.3 Rotational Brownian motion in a magnetic field

B.3.1 Autocorrelation function

In Section 5.2.3 we measured the flux noise due to magnetotactic bacteria in the presence of a field. The Fokker-Planck equation (B.7) must be modified to include the torque $\mathbf{m} \times \mathbf{B} = mB\sin\theta$ applied to the dipole by the field [72]:

$$\frac{\partial W}{\partial t} = D_r \left(\frac{1}{\sin\theta} \frac{\partial}{\partial\theta} \sin\theta \frac{\partial W}{\partial\theta} + \frac{1}{\sin^2\theta} \frac{\partial^2 W}{\partial\phi^2} + \frac{1}{\sin\theta} \frac{\partial}{\partial\theta} \sin\theta \cdot \xi \sin\theta W \right). \tag{B.17}$$

Unfortunately this equation cannot be solved analytically. The spherical harmonics $Y_{\ell,m}$ are no longer eigenfunctions of the Fokker-Planck equation since the torque term converts each $Y_{\ell,m}$ to a linear combination of $Y_{\ell-1,m}$ and $Y_{\ell+1,m}$. However, it is still convenient to express any solutions to Eq. (B.17) in terms of spherical harmonics by the same arguments made in the previous section. The joint probability distribution which solves Eq. (B.17) has the general form:

$$W_2(\Omega,t;\Omega_o,0)=\frac{1}{4\pi}\sum_{\ell,\ell',m}A_{\ell,\ell',m}(\xi,D_r|t|)Y^*_{\ell m}(\Omega_o)Y_{\ell' m}(\Omega). \tag{B.18}$$

Algorithms exist for calculating $A_{\ell,\ell',m}(\xi,|t|)$ numerically. However, in the limit $\xi \ll 1$, one can use perturbation theory [73]. Since the perturbation term is not diagonal, I expect the lowest order corrections to be $\mathcal{O}(\xi^2)$. After some algebra, I find

$$\langle\cos\theta\cos\theta_o\rangle-\langle\cos\theta\rangle\langle\cos\theta_o\rangle=\left(\frac{1}{3}-\frac{13\xi^2}{180}\right)e^{-2(1+\frac{\xi^2}{10})D_r|t|}+\frac{\xi^2}{180}e^{-6D_r|t|}+\mathcal{O}(\xi^4). \tag{B.19}$$

Note that at $t=0$, Eq. (B.19) agrees with (4.2) up to $\mathcal{O}(\xi^4)$. Furthermore, setting $\xi=0$ I recover Eq. (B.11). Finally,

$$\begin{aligned}\langle\sin\theta\cos\phi\sin\theta_o\cos\phi_o\rangle&=\left(\frac{1}{3}-\frac{19\xi^2}{720}\right)e^{-2(1+\frac{3\xi^2}{40})D_r|t|}+\frac{\xi^2}{240}e^{-6D_r|t|}+\mathcal{O}(\xi^4)\\&=\langle\sin\theta\sin\phi\sin\theta_o\sin\phi_o\rangle.\end{aligned} \tag{B.20}$$

Again I recover Eq. (B.13) for $\xi=0$. Note that there are two different decay times for components parallel and perpendicular to the field.

In the opposite limit $\xi \gg 1$, it is also possible to obtain an analytical solution to Eq. (B.17) by making a simplifying approximation. In the limit of large field, I can assume that the angle θ between the field and the dipole moment is small. Thus, the potential due to the field is harmonic and the Fokker-Planck equation can be solved analytically. Expanding to lowest order in θ (ϕ can take on any value), Eq. (B.17) becomes

$$\frac{\partial W}{\partial t}=D_r\left(\frac{1}{\theta}\frac{\partial}{\partial\theta}\theta\frac{\partial W}{\partial\theta}+\frac{1}{\theta^2}\frac{\partial^2 W}{\partial\phi^2}+\frac{1}{\theta}\frac{\partial}{\partial\theta}\theta\cdot\xi\theta W\right). \tag{B.21}$$

The exact solution for the joint probability density is given by [72]

$$W_2(\Omega,t;\Omega_o,0)=\frac{\xi^2}{(2\pi)^2}\frac{1}{1-e^{-2\xi D_r|t|}}\exp\left(-\xi\frac{\theta^2-2\theta\theta_o e^{-\xi D_r|t|}\cos(\phi-\phi_o)+\theta_o^2}{2(1-e^{-2\xi D_r|t|})}\right). \tag{B.22}$$

The angular autocorrelation functions are also calculated by expanding to lowest order in θ. The results are as follows:

$$\langle \cos\theta \cos\theta_o \rangle - \langle \cos\theta \rangle \langle \cos\theta_o \rangle = \frac{1}{\xi^2} e^{-2\xi D_r |t|}$$
$$\langle \sin\theta \cos\phi \sin\theta_o \cos\phi_o \rangle = \frac{1}{\xi} e^{-\xi D_r |t|} = \langle \sin\theta \sin\phi \sin\theta_o \sin\phi_o \rangle. \tag{B.23}$$

Note that in this limit the diffusion constant $D_r = k_B T/\alpha_r$ has effectively been replaced by $\xi D_r = mB/\alpha_r$. Again, there is a decay constant for the component parallel to the field and another for perpendicular components.

B.3.2 Response function

In Section 5.2.4, we turned on a magnetic field at $t = 0$ and measured the response function as the magnetotactic bacteria aligned to the field. The same approach can be used to calculate the response function as above, only this time using Eq. (B.17).

Again I use perturbation theory in the low field limit $\xi \ll 1$. The probability distribution W_1 is of the form

$$W_1(\Omega, t) = \frac{1}{4\pi} \sum_{\ell,m} A_{\ell,m}(\xi, D_r|t|) Y_{\ell m}(\Omega), \tag{B.24}$$

and must satisfy the initial condition $W_1(\Omega, 0) = 1/4\pi$ and approach Eq. (B.14) as $t \to \infty$. After some algebra, I calculate the angular response functions of $\cos\theta$, $\sin\theta\cos\phi$, and $\sin\theta\sin\phi$

$$\langle \cos\theta(t) \rangle = \left(\frac{\xi}{3} - \frac{\xi^3}{45}\right) - \left(\frac{\xi}{3} - \frac{\xi^3}{60}\right) e^{-2(1+\frac{\xi^2}{10})D_r t} + \frac{\xi^3}{180} e^{-6D_r t} + \mathcal{O}(\xi^4), \tag{B.25}$$

valid up to $\mathcal{O}(\xi^4)$. Again, by symmetry $\langle \sin\theta(t)\cos\phi(t) \rangle = \langle \sin\theta(t)\sin\phi(t) \rangle = 0$. Note that at $t = 0$, $\langle \cos\theta \rangle = 0$, while as $t \to \infty$ Eq. (B.25) approaches $L(\xi)$, in the limit of $\xi \ll 1$.

The large field limit $\xi \gg 1$ is somewhat more problematic, since the assumption that θ is small is clearly invalid for short times after the field has been turned on. Thus, solutions to Eq. (B.21) are only valid for long times, when the dipole moment is close to being fully aligned with the field. One approach is to calculate the conditional probability density $P(\theta, t|, \theta_o, 0)$ assuming the initial angle θ_o is small. Then, using Eqs. (B.1) and (B.6), I calculate $\langle \cos\theta \rangle$ in terms of θ_o. This solution, valid for small θ_o, is extended to large values of θ_o by making the correspondence $1 - \theta_o^2/2 \approx \cos\theta_o$. Averaging over all of

the possible initial angles yields

$$\langle \cos\theta(t) \rangle = \left(1 - \frac{1}{\xi}\right)\left(1 - e^{-2\xi D_r t}\right), \tag{B.26}$$

which is 0 at $t = 0$, and approaches $L(\xi)$ for $\xi \gg 1$ as $t \to \infty$.

Appendix C

Modeling of the Dynamics of Motile Bacteria

C.1 Low-frequency behavior

Modeling the dynamics of motile bacteria is a much more difficult task than modeling those of nonmotile cells. As explained in Section 5.3, the translational motion of the cells across the SQUID cannot be ignored. Whereas in the previous analysis, the SQUID geometry came in only as a geometrical factor to scale the data, here it is inextricably linked to the dynamics. The dynamical variables are now the orientation of the dipole moment, $\theta(t)$ and $\phi(t)$, and the position vector $\mathbf{r}(t)$. Worse still, these variables are coupled to each other, since the velocity vector $\mathbf{v}(t) = \dot{\mathbf{r}}(t)$ points along the dipole moment $\mathbf{m}$.

A complete model would appear to be one which treats each bacterium as a self-propelled dipole moment which can rotationally diffuse. It is relatively straightforward to write down the equations of motion for such a model, but another matter entirely to solve them. One approach is to run computer simulations. Helene carried out extensive computer simulations but I will not discuss them in detail here, except to say that they qualitatively agree with the results that I will present shortly. Another, more practical approach is to simplify the problem to a more solvable one to gain a qualitative understanding of the data.

With this in mind, the addition of the position as a dynamical variable makes the flux autocorrelation function take the form

$$\langle \Phi(t)\Phi(0) \rangle = \int d^3\mathbf{r} \int d^3\mathbf{r}_o \int d\Omega \int d\Omega_o \, \Phi(\mathbf{r},\Omega)\Phi(\mathbf{r},\Omega) W_2(\mathbf{r},\Omega,t;\mathbf{r}_o,\Omega_o,0), \qquad \text{(C.1)}$$

where $\Omega = \{\theta, \phi\}$. I have not been able to calculate an analytical expression for the joint probability density W_2 for the model presented above. However, if I am only interested in time scales over which the cells swim a distance comparable to the size of the SQUID, I can make some simplifying assumptions. If the speed of the cell v is large, or the rotational diffusion constant D_r small, the cell swims in a roughly straight line for a large distance. If this "persistence length", given by v/D_r is much greater than the SQUID size ℓ_{eff}, I am justified in ignoring the rotational diffusion of the cell over the time scale of interest. Taking $v \sim 100\mu m/s$ and $D_r = 0.1s^{-1}$ (see Section 5.2), $v/D_r \sim 1mm$, much greater than ℓ_{eff} for any of the SQUIDs used.

In this limit, the orientation of each cell θ, ϕ is constant, and the position is simply given by $\mathbf{r} = \mathbf{r}_o + \mathbf{v}t$, with $\mathbf{v}$ pointing along the cell's orientation. The joint probability density W_2 is then

$$W_2(\mathbf{r}, \Omega, t; \mathbf{r}_o, \Omega_o, 0) = \frac{\rho_b}{4\pi}\delta^3(\mathbf{r} - \mathbf{r}_o - \mathbf{v}t)\delta^2(\Omega - \Omega_o). \tag{C.2}$$

For simplicity I ignore the boundaries of the sample container, in particular the SiN vacuum window. Equation (C.1) becomes

$$\langle \Phi(t)\Phi(0)\rangle = \int d^3\mathbf{r}\,\rho_b \int \frac{d\Omega}{4\pi}\,\Phi(\mathbf{r} - \mathbf{v}t, \Omega)\Phi(\mathbf{r}, \Omega). \tag{C.3}$$

This integral can be solved numerically. However, it is more instructive to simplify the model further and attempt to obtain an analytical expression. Since I am interested in the effect of the SQUID geometry on the flux autocorrelation function—particularly, showing that the spectrum knee frequency is related to ℓ_{eff}—I will only consider motion of the bacteria across the SQUID pickup area, and ignore motion normal to the SQUID plane. Henceforth, I will set $v_z = 0$.

At this point it is convenient to use the Fourier space representation of the flux transfer function as described in Appendix A. Note that Eq. (C.3) is a convolution, so that taking the Fourier transform in x and y leads to

$$\langle \Phi(t)\Phi(0)\rangle = \int \frac{d^2\mathbf{k}}{(2\pi)^2} \int dz\,\rho_b \int \frac{d\Omega}{4\pi}\,|\tilde{\Phi}_{\mathbf{k}}(z, \Omega)|^2 e^{i\mathbf{k}\cdot\mathbf{v}t}. \tag{C.4}$$

The Fourier transform in x and y of the flux, $\tilde{\Phi}_{\mathbf{k}}(z, \Omega)$ is given by

$$\tilde{\Phi}_{\mathbf{k}}(z, \Omega) = \tilde{\Phi}_{\mathbf{k},z}(z)\cos\theta + \tilde{\Phi}_{\mathbf{k},x}(z)\sin\theta\cos\phi + \tilde{\Phi}_{\mathbf{k},y}(z)\sin\theta\sin\phi, \tag{C.5}$$

where the components $\tilde{\Phi}_{\mathbf{k},x,y,z}(z)$ are defined in Appendix A [see Eq. A.7]. Note that the quantity in the exponential $\mathbf{k}\cdot\mathbf{v}t = k_x vt\sin\theta\cos\phi + k_y vt\sin\theta\sin\phi$, is a function of the same angles θ, ϕ since the velocity vector $\mathbf{v}$ lies in the same direction as the dipole moment.

Carrying out the average over all the possible orientations θ, ϕ of the bacteria, all cross-terms average out to zero and one is left with

$$\langle\Phi(t)\Phi(0)\rangle = \int_{-\infty}^{\infty}\frac{d^2\mathbf{k}}{(2\pi)^2}\int_{z_o}^{\infty}dz\,\rho_b\left\{|\tilde{\Phi}_{\mathbf{k},z}(z)|^2\left(j_0(kvt)-\frac{j_1(kvt)}{kvt}\right)\right.$$
$$\left.+\,|\tilde{\Phi}_{\mathbf{k},x}(z)|^2\frac{k_y^2}{k^2}j_2(kvt)+|\tilde{\Phi}_{\mathbf{k},y}(z)|^2\frac{k_x^2}{k^2}j_2(kvt)\right\} \qquad \text{(C.6)}$$

where the functions j_ℓ are spherical Bessel functions order ℓ and $k \equiv \sqrt{k_x^2+k_y^2}$. I have used the fact that $|\tilde{\Phi}_{\mathbf{k},x}|^2 + |\tilde{\Phi}_{\mathbf{k},y}|^2 = |\tilde{\Phi}_{\mathbf{k},z}|^2$ [see Eq. (A.7)].

For the model described, Eq. (C.6) is exact and may be integrated analytically. One may get a qualitative picture of the behavior of this integral by looking carefully at each term. The time-dependent part of the first term, $j_0(kvt) - j_1(kvt)/kvt$, is sharply peaked near $k = 0$ with a width that scales as $1/vt$. In the second term $j_2(kvt)$ oscillates rapidly and tends to average out to a small value. Thus, one can ignore that term, as well as any small oscillatory behavior for $kvt \gg 1$. The Fourier transform of the flux transfer function $\tilde{\Phi}_{\mathbf{k},z}(z)$ is sharply peaked in an annular region $|k| \sim 1/\ell_{eff}$ for $z_o/\ell_{eff} \ll 1$, and oscillates to zero for $|k| \gg 1/\ell_{eff}$ [see Eq. (A.7)].

Thus, the integral qualitatively behaves in the following manner: for $vt \lesssim \ell_{eff}$, the factor $j_0(kvt) - j_1(kvt)/kvt$ overlaps the peak in the flux transfer function and the integral is large; for $vt \gtrsim \ell_{eff}$ that factor overlaps progressively less of the peak, and the integral decays to zero as $t \to \infty$. The autocorrelation function decays in time with a characteristic time constant that scales as ℓ_{eff}/v. Figure C.1 plots the autocorrelation function (C.6) for a particular value of z_o and ℓ_{eff}; the inset shows that the time constant of the decay is linear in ℓ_{eff} for $\ell_{eff} > z_o$.

This model demonstrates that the knee frequency in the spectrum for motile cells corresponds to the rate at which bacteria swim across the SQUID sensing area, in agreement with the computer simulations run independently by Helene. However, it does not address the issue of the non-Lorentzian shape of the spectrum. For frequencies greater than $\sim v/\ell_{eff}$, Eq. (C.6) predicts a $1/f^2$ fall-off in the spectrum. Unfortunately, I am unable to come up with a mathematical model which reproduces the $1/f^\nu$, $\nu \approx 2.4$ behavior of the data. Thus, the form of the low-frequency spectrum will not be derived analytically in this thesis.

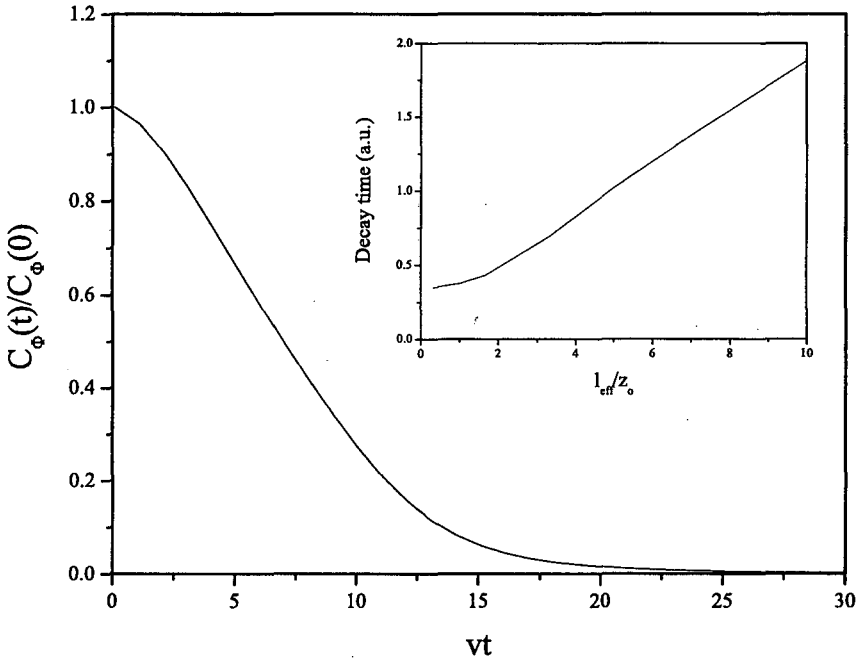

Figure C.1: Flux autocorrelation function for motile cells swimming across the SQUID area. The trace shown, obtained for the parameter $z_o/\ell_{eff} = 0.15$, decays in a characteristic decay time. The inset plots the decay time as a function of SQUID effective size ℓ_{eff}. For $\ell_{eff} > z_o$, the decay time scales linearly with ℓ_{eff}.

Instead, I will use an empirical function that is fitted to the data: a modified Lorentzian with an exponent ν

$$S_\Phi(f) = C_\Phi(0)\frac{\nu}{2}\sin\frac{\pi}{\nu}\cdot\frac{2\tau_m}{1+(2\pi|f|\tau_m)^\nu}. \tag{C.7}$$

The prefactor ensures that the sum rule $\int_{-\infty}^{\infty} S_\Phi(f)\,df = C_\Phi(0)$ is satisfied. (The sum rule is easily obtained by taking the inverse Fourier transform of S_Φ and setting $t = 0$.)

C.2 Rotational and vibrational modes

In the following I calculate the effect of the vibrational and rotational motions of the bacteria on the measured flux noise power spectrum $S_\Phi(f)$ of the SQUID. First I determine the flux $\Phi(t)$ generated at the SQUID by such motion. Then, I calculate the autocorrelation function $C_\Phi(t)$ of this flux, and its Fourier transform, the spectral density $S_\Phi(f)$.

Consider a bacterium at position $\mathbf{r}(t)$ measured from the center of the SQUID, undergoing the motion depicted in Fig. 5.7. A bacteria (primed) reference frame is defined such that $\hat{z}'$ lies along the direction of motility, and a lab (unprimed) frame with $\hat{z}$ normal to the SQUID. The equation of motion for the magnetic dipole moment $\mathbf{m}'$ in the primed frame is

$$\begin{aligned}
\mathbf{m}' &= m\,\hat{z}'\,[\cos\phi_p\cos\phi_v - \sin\phi_p\sin\phi_v\sin(2\pi f_v t+\delta_v)] \\
&+ m\,\hat{x}'\,[\sin\phi_p\cos\phi_v\cos(2\pi f_p t+\delta_p) + \cos\phi_p\sin\phi_v\cos(2\pi f_p t+\delta_p)\sin(2\pi f_v t+\delta_v) \\
&- \sin\phi_v\sin(2\pi f_p t+\delta_p)\cos(2\pi f_v t+\delta_v)] \\
&+ m\,\hat{y}'\,[\sin\phi_p\cos\phi_v\sin(2\pi f_p t+\delta_p) + \cos\phi_p\sin\phi_v\sin(2\pi f_p t+\delta_p)\sin(2\pi f_v t+\delta_v) \\
&+ \sin\phi_v\cos(2\pi f_p t+\delta_p)\cos(2\pi f_v t+\delta_v)]\,,
\end{aligned} \tag{C.8}$$

where ϕ_v, ϕ_p, f_v, f_p are defined in the figure, and δ_v and δ_p are phases. The subscripts v and p refer to vibration and precession, respectively. Note that f_v and f_p are defined with opposite sign, since the cell body counterrotates with respect to the flagellum. The orientation $\theta(t)$, $\varphi(t)$ of the bacteria with respect to the SQUID is arbitrary, and varies as the bacteria swims. The equation of motion for $\mathbf{m}$ in the lab frame is then easily obtained

by a suitable transformation $\mathbf{T}(\theta, \varphi)$:

$$\mathbf{T}(\theta,\varphi) = \begin{pmatrix} \cos\theta\cos\varphi & -\sin\varphi & \sin\theta\cos\varphi \\ \cos\theta\sin\varphi & \cos\varphi & \sin\theta\sin\varphi \\ -\sin\theta & 0 & \cos\theta \end{pmatrix} \tag{C.9}$$

so that $\mathbf{m} = \mathbf{T}(\theta, \varphi)\mathbf{m}'$. The result is lengthy and not particularly illuminating, and will not be included here.

The flux $\Phi(t)$ generated at the SQUID by each bacterium is determined from the components of $\mathbf{m}$ along $\hat{x}$, $\hat{y}$, and $\hat{z}$ in the SQUID reference frame, and the geometrical factors $\Phi_{x,y,z}(\mathbf{r}(t), \ell_{eff})$ defined in Appendix A. It is important to note at this juncture that the time dependence of the flux comes from two sources, one slowly varying, the other fast. The variables $\mathbf{r}(t)$, $\theta(t)$, and $\varphi(t)$ which are responsible for the random motility of the bacteria, generate the low-frequency part of the noise spectrum ($\lesssim 0.1$Hz). The fast variables, responsible for the vibration and precession of the cells, occur at much higher frequencies f_v, f_p (10-100Hz). A reasonable simplification for this calculation is that the two do not couple to each other and may treated independently. In other words, in the low-frequency regime, the cells' vibration and precession average out, and in the high-frequency regime, the cells' orientation and position are constant.

With this in mind, I calculate the autocorrelation function, $C_\Phi(t) \equiv \langle \Phi(t)\Phi(0) \rangle$ averaging over all of the degrees of freedom of the system: the positions $\mathbf{r}$, orientations θ, φ, frequencies $f_{v,p}$, and phases $\delta_{v,p}$ of each bacteria in the ensemble. Note that I do not average over the angles $\phi_{v,p}$ since these are presumably uniquely determined by the frequencies.

The averages are long and tedious to carry out, but simplify the expressions greatly, since many terms (including all cross-terms) average to zero. The averages over the phases are simple:

$$\begin{aligned} \langle \sin(2\pi f t + \delta)\sin\delta \rangle_\delta &= \langle \cos(2\pi f t + \delta)\cos\delta \rangle_\delta = \frac{1}{2}\cos(2\pi f t) \\ \langle \sin(2\pi f t + \delta)\cos\delta \rangle_\delta &= -\langle \cos(2\pi f t + \delta)\sin\delta \rangle_\delta = \frac{1}{2}\sin(2\pi f t). \end{aligned} \tag{C.10}$$

The autocorrelations for the slow variables $\mathbf{r}(t)$, $\theta(t)$, and $\varphi(t)$ get lumped together. Some terms depend only on slow variables, others on both fast and slow variables. A further simplification is to assume that ϕ_v and ϕ_p are small and keep only lowest-order terms. This

leads to the following concise result, which consists of only two terms

$$\begin{aligned} C_\Phi(t) &= C_\Phi(0)\left\{(1-\phi_v^2-\phi_p^2)\cdot j(t)\right. \\ &+ \left.\left\langle \phi_p^2\cos(2\pi f_p t)+\phi_v^2\cos(2\pi(f_v-f_p)t)\right\rangle_{f_v,f_p}\cdot h(t)\right\}, \end{aligned} \tag{C.11}$$

with $C_\Phi(0) = \mathcal{G}^{(s)}/3$ ($\mathcal{G}^{(s)}$ is defined in Appendix A). (Note that I have not yet averaged over the frequencies f_v, f_p.)

The functions $j(t)$ and $h(t)$ appear from the autocorrelations of the position $\mathbf{r}(t)$ and orientation $\theta(t)$ and $\varphi(t)$. Although the exact form of j and h is unknown at this point, they are normalized so that $j(0) = 1 = h(0)$. The whole expression is normalized such that at $t = 0$, $C_\Phi(0) = \langle\Phi^2\rangle = \mathcal{G}^{(s)}/3$ independent of dynamics (this condition is true for nonmotile cells as well). The second term is responsible for the peaks at f_p and $f_v - f_p$ in the measured spectra. Thus, in the expression above, the first term (with $j(t)$) is slow, while the second term (with $h(t)$) is dominated by the oscillatory behavior and is fast. As discussed above, I may set $h(t) = h(0) = 1$ with minimal error, since the vibration and rotation occur so rapidly that I may ignore the swimming of the cell in that time scale.

The averages over f_v and f_p are carried out with a suitable probability distribution. A Gaussian peaked at frequency $\bar{f}_{v,p}$ and with width $\Delta_{v,p}$ is a reasonable assumption:

$$\langle\cdots\rangle_{f_v} \approx (2\pi\Delta_v^2)^{-1/2}\int_0^\infty df_v\, e^{-(f_v-\bar{f}_v)^2/2\Delta_v^2}\cdots, \tag{C.12}$$

which is properly normalized in the limit that $\Delta_{v,p}/\bar{f}_{v,p}$ is adequately small.

Following the average over f_v and f_p in Eq. (C.11), I take the Fourier transform and obtain

$$\begin{aligned} S_\Phi(f) &= C_\Phi(0)\left\{ (1-\phi_v^2-\phi_p^2)\cdot\tilde{J}(f)\right. \\ &+ \frac{\phi_v^2}{2}(2\pi\Delta_1^2)^{-1/2}\left(e^{-(f-\bar{f}_1)^2/2\Delta_1^2}+e^{-(f+\bar{f}_1)^2/2\Delta_1^2}\right) \\ &+ \left.\frac{\phi_p^2}{2}(2\pi\Delta_2^2)^{-1/2}\left(e^{-(f-\bar{f}_2)^2/2\Delta_2^2}+e^{-(f+\bar{f}_2)^2/2\Delta_2^2}\right)\right\}, \end{aligned} \tag{C.13}$$

where $\bar{f}_1 \equiv \bar{f}_p$, $\Delta_1 \equiv \Delta_p$, $\bar{f}_2 \equiv \bar{f}_v - \bar{f}_p$, and $\Delta_2^2 \equiv \Delta_v^2 + \Delta_p^2$. The function $\tilde{J}(f)$ will not be derived analytically; instead, I use the modified Lorentzian in Eq. (C.7). Equation (C.13) must satisfy the sum rule $\int_{-\infty}^{\infty} S_\Phi(f)\, df = C_\Phi(0)$. It is trivial to verify that Eq. (C.13) indeed satisfies this condition.

Equations (C.13) and (C.7) together are the fitting function for the measured spectra. The angular amplitudes $\phi_{p,v}$ can be determined from the ratio of the spectral densities at the peak frequencies and at 0. Ignoring all small terms I find

$$\phi_{p,v}^2 \approx 2\sqrt{2\pi}\nu \sin\frac{\pi}{\nu}\left(\tau_m \Delta_{1,2}\right) \frac{S_\Phi(\bar{f}_{1,2})}{S_\Phi(0)} \tag{C.14}$$

which is Eq. (5.13).

Bibliography

[1] Y. R. Chemla, H. L. Grossman, T. S. Lee, J. Clarke, M. Adamkiewicz, and B. B. Buchanan. A new study of bacterial motion: superconducting quantum interference device microscopy of magnetotactic bacteria. *Biophys. J.*, 76:3323–3330, 1999.

[2] Y. R. Chemla, H. L. Grossman, Y. Poon, R. McDermott, R. Stevens, M. D. Alper, and J. Clarke. Ultrasensitive magnetic biosensor for homogeneous immunoassay. *Proc. Nat. Acad. Sci. USA*, 97(26):14268–14272, 2000.

[3] D. Koelle, R. Kleiner, F. Ludwig, E. Dantsker, and J. Clarke. High-transition temperature superconducting quantum interference devices. *Rev. Mod. Phys.*, 71(3):631–686, 1999.

[4] T. S. Lee, E. Dantsker, and J. Clarke. High-transition temperature superconducting quantum interference device microscope. *Rev. Sci. Instrum.*, 67:4208–4215, 1996.

[5] J. Clarke. SQUID fundamentals. In Harold Weinstock, editor, *SQUID Sensors: Fundamentals, Fabrication and Applications*, volume 329 of *NATO ASI Series*, pages 1–62, Netherlands, 1996. Kluwer Academic Publishers.

[6] R. C. Jaklevic, J. Lambe, A. H. Silver, and J. E. Mercereau. Quantum interference effects in Josephson tunneling. *Phys. Rev. Lett.*, 12(7):159–160, 1964.

[7] J. E. Zimmerman, P. Thiene, and J. T. Harding. Design and operation of stable rf-biased superconducting point-contact quantum devices, and a note on the properties of perfectly clean metal contacts. *J. Appl. Phys.*, 41:1572–1580, 1970.

[8] A. H. Miklich, D. Koelle, E. Dantsker, D. T. Nemeth, J. J. Kingston, R. F. Kromann, and J. Clarke. Bicrystal YBCO dc SQUIDs with low noise. *IEEE Trans. Appl. Supercond.*, 3:2434–2437, 1993.

[9] J. E. Zimmerman and J. E. Mercereau. Quantized flux pinning in superconducting niobium. *Phys. Rev. Lett.*, 13(4):125–126, 1964.

[10] L. N. Vu and D. J. Van Harlingen. Design and implementation of a scanning SQUID microscope. *IEEE Trans. Appl. Supercond.*, 3(1):1918–21, 1993.

[11] J. R. Kirtley, M. B. Ketchen, C. C. Tsuei, J. Z. Sun, W. J. Gallagher, Lock See Yu-Jahnes, A. Gupta, K. G. Stawiasz, and S. J. Wind. Design and applications of a scanning SQUID microscope. *IBM J. Res. Dev.*, 39(6):665–68, 1995.

[12] F. C. Wellstood, Y. Gim, A. Amar, R. C. Black, and A. Mathai. Magnetic microscopy using SQUIDs. *IEEE Trans. Appl. Supercond.*, 7(2):3134–38, 1997.

[13] J. R. Wikswo, Jr., Y. P. Ma, N. G. Sepulveda, S. Tan, I. M. Thomas, and A. Lauder. Magnetic susceptibility imaging for nondestructive evaluation (using SQUID magnetometer). *IEEE Trans. Appl. Supercond.*, 3:1995–2002, 1993.

[14] J. R. Wikswo, Jr. High resolution magnetic imaging: cellular action current and other applications. In Harold Weinstock, editor, *SQUID Sensors: Fundamentals, Fabrication and Applications*, volume 329 of *NATO ASI Series*, pages 307–360, Netherlands, 1996. Kluwer Academic Publishers.

[15] J. R. Kirtley and J. P. Wikswo, Jr. Scanning SQUID microscopy. *Annu. Rev. Mater. Sci.*, 29:117–48, 1999.

[16] R. C. Black. *Magnetic microscopy using a superconducting quantum interference device.* PhD thesis, University of Maryland, 1995.

[17] T. S. Lee. *Cold SQUIDs and Hot Samples.* PhD thesis, University of California, Berkeley, 1997.

[18] T. S. Lee, Y. R. Chemla, E. Dantsker, and J. Clarke. High-T_c SQUID microscope for room temperature samples. *IEEE Trans. Appl. Supercond.*, 7:3147–3150, 1997.

[19] J. D. Jackson. *Classical Electrodynamics.* John Wiley & Sons, New York, second edition edition, 1975.

[20] R. P. Blakemore. Magnetotactic bacteria. *Science*, 190:377–379, 1975.

[21] R. P. Blakemore, R. B. Frankel, and A. J. Kalmijn. South-seeking magnetotactic bacteria in the southern hemisphere. *Nature*, 286:384–385, 1980.

[22] R. B. Frankel, R. P. Blakemore, F. F. Torres de Araujo, D. M. S. Esquivel, and J. Danon. Magnetotactic bacteria at the geomagnetic equator. *Science*, 212:1269–1270, 1981.

[23] S. Spring and K. H. Schleifer. Diversity of magnetotactic bacteria. *System. Appl. Microbiol.*, 18:147–153, 1995.

[24] R. P. Blakemore. Magnetotactic bacteria. *Ann. Rev. Microbiol.*, 36:217–238, 1982.

[25] F. G. Rodgers, R. P. Blakemore, N. A. Blakemore, R. B. Frankel, D. A. Bazylinski, D. Maratea, and C. Rodgers. Intercellular structure in many-celled magnetotactic prokaryote. *Arch. Microbiol.*, 154:18–22, 1990.

[26] D. A. Bazylinski. Structure and function of the bacterial magnetosome. *ASM News*, 61(7):337–343, 1995.

[27] H. C. Berg. *Random Walks in Biology.* Princeton University Press, New Jersey, 1983.

[28] G. M. Viswanathan, S. V. Buldyrev, S. Havlin, M. G. E. da Luz, E. P. Raposo, and H. E. Stanley. Optimizing the success of random searches. *Nature*, 401(6756):911–914, 1999.

[29] R. B. Frankel. Magnetic guidance of organisms. *Ann. Rev. Biophys. Bioeng.*, 13:85–103, 1984.

[30] A. J. Kalmijn. Biophysics of geomagnetic field detection. *IEEE Trans. Magn.*, 17:1113–1124, 1981.

[31] R. B. Frankel, D. A. Bazylinski, M. S. Johnson, and B. L. Taylor. Magneto-aerotaxis in marine coccoid bacteria. *Biophys. J.*, 73:994–1000, 1997.

[32] R. B. Frankel, D. A. Bazylinski, and D. Schüler. Biomineralization of magnetic iron minerals in magnetotactic bacteria. *Supramol. Sci.*, 5:383–390, 1998.

[33] D. Schüler. Formation of magnetosomes in magnetotactic bacteria. *J. Molec. Microbiol. Biotechnol.*, 1(1):79–86, 1999.

[34] C. Rosenblatt, F. F. Torres de Araujo, and R. B. Frankel. Light scattering determination of magnetic moments of magnetotactic bacteria. *J. Appl. Phys.*, 53:2727–2729, 1982.

[35] C. Rosenblatt, F. F. Torres de Araujo, and R. B. Frankel. Birefringence determination of magnetic moments of magnetotactic bacteria. *Biophys. J.*, 40:83–85, 1982.

[36] R. B. Proksch, T. E. Schäffer, B. M. Moskowitz E. D. Dahlberg, D. A. Bazylinski, and R. B. Frankel. Magnetic force microscopy of the submicron magnetic assembly in a magnetotactic bacterium. *Appl. Phys. Lett.*, 66:2582–2584, 1995.

[37] D. M. S. Esquivel and H. G. P. Lins de Barros. Motion of magnetotactic microorganisms. *J. Exp. Biol.*, 121:153–163, 1986.

[38] Y. A. Gorby, T. J. Beveridge, and R. P. Blakemore. Characterization of the bacterial magnetosome membrane. *J. Bacteriol.*, 170:834–841, 1988.

[39] R. B. Frankel, G. C. Papaefthymiou, R. P. Blakemore, and W. O'Brien. Fe_3O_4 precipitation in magnetotactic bacteria. *Biochim. Biophys. Acta*, 763:147–159, 1983.

[40] A. S. Bahaj, P. A. B. James, D. C. Ellwood, and J. H. P. Watson. Characterization and growth of magnetotactic bacteria: implications of clean up of environmental pollution. *J. Appl. Phys.*, 73:5394–5396, 1993.

[41] E. A. Wolin, M. J. Wolin, and R. S. Wolfe. Formation of methane by bacterial extracts. *J. Biol. Chem.*, 238:2882–2886, 1963.

[42] F. Reif. *Fundamentals of Statistical Physics and Thermal Physics.* McGraw-Hill Publishing Co., New York, 1965.

[43] M. M. Tirado and J. G. de la Torre. Rotational dynamics of rigid, symmetric top macromolecules. application to circular cylinders. *J. Chem. Phys.*, 73:1986–1993, 1980.

[44] H. Scher, M. F. Shlesinger, and J. T. Bendler. Time-scale invariance in transport and relaxation. *Physics Today*, pages 26–34, Jannuary 1991.

[45] A. S. Bahaj, P. A. B. James, and F. D. Moeschler. An alternate method for the estimation of the magnetic moment of non-spherical magnetotactic bacteria. *IEEE Trans. Magn.*, 32:5133–5135, 1996.

[46] C. Rosenblatt, R. B. Frankel, and R. P. Blakemore. A birefringence relaxation determination of rotational diffusion of magnetotactic bacteria. *Biophys. J.*, 47:323–325, 1985.

[47] J. Klafter, M. F. Shlesinger, and G. Zumofen. Beyond Brownian motion. *Physics Today*, pages 33–39, February 1996.

[48] G. M. Viswanathan, V. Afanasyev, S. V. Buldyrev, E. J. Murphy, P. A. Prince, and H. E. Stanley. Lévy flight search patterns of wandering albatrosses. *Nature*, 381:413–415, 1996.

[49] H. C. Berg. Torque generation by the flagellar motor. *Biophys. J.*, 68:63s–167s, 1995.

[50] G. Lowe, M. Meister, and H. C. Berg. Rapid rotation of flagellar bundles in swimming bacteria. *Nature*, 325:637–640, 1987.

[51] A. M. Spormann and R. S. Wolfe. Chemotactic, magnetotactic and tactile behaviour in a magnetic spirillum. *FEMS Microbiol. Lett.*, 22:171–177, 1984.

[52] S. Chandrasekhar. Stochastic problems in physics and astronomy. *Rev. Mod. Phys.*, 15(1):1–89, 1943.

[53] P. D. Frymier, R. M. Ford, H. C. Berg, and P. T. Cummings. Three-dimensional tracking of motile bacteria near a solid planar surface. *Proc. Nat. Acad. Sci.*, 92:6195–6199, 1995.

[54] M. Ramia, D. L. Tullock, and N. Phan-Thien. The role of hydrodynamic interactions in the locomotion of microorganisms. *Biophys. J.*, 65:755–778, 1993.

[55] U. Häfeli, W. Schütt, J. Teller, and M. Zborowski, editors. *Scientific and Clinical Applications of Magnetic Microspheres.* Plenum, New York, 1997.

[56] I. Šafařík and M. Šafaříková. Use of magnetic techniques for the isolation of cells. *J. Chromatogr. B.*, 722:33–53, 1999.

[57] W. Weitschies, R. Kötitz, T. Bunte, and L. Trahms. Determination of relaxing or remanent nanoparticle magnetization provides a novel binding-specific technique for the evaluation of immunoassays. *Pharm. Pharmacol. Lett.*, 7:5–8, 1997.

[58] D. Voet, J. G. Voet, and C. W. Pratt. *Fundamentals of Biochemistry.* John Wiley & Sons, Inc., New York, 1998.

[59] R. R. Meer and D. L. Park. Immunochemical detection methods for Salmonella spp., Escherichia coli O157:H7 and Listeria monocytogenes in foods. *Rev. Env. Cont. Toxicol.*, 142:1–12, 1995.

[60] K. Enpuku, T. Minotani, T. Gima, Y. Kuroki, Y. Itoh, M. Yamashita, Y. Katakura, and S. Kuhara. Detection of magnetic nanoparticles with Superconducting QUantum Interference Device (SQUID) magnetometer and application to immunoassays. *Jpn. J. Appl. Phys.*, 38:L1102–L1105, 1999.

[61] E. Blums, A. Cebers, and M. M. Maiorov. *Magnetic fluids.* Walter de Gruyter, New York, 1997.

[62] E. W. Jones. Tackling the protease problem in Saccharomyces cerevisiae. *Methods Enzymol.*, 194:428–453, 1991.

[63] N. David, M. Gee, B. Andersen, F. Naider, J. Thorner, and R. Stevens. Expression and purification of the Saccharomyces cerevisiae alpha-factor receptor (Ste2p), a 7-transmembrane-segment G protein-coupled receptor. *J. Biol. Chem.*, 272:15553–15561, 1997.

[64] D. V. Berkov and R. Kötitz. Irreversible relaxation behaviour of a general class of magnetic systems. *J. Phys. Condens. Matter*, 8:1257–1266, 1996.

[65] L. Néel. Theory of the magnetic after-effects in ferromagnetics in the form of small particles, with applications to baked clays. *Ann. Geophys.*, 5:99–119, 1949.

[66] H. Noji, R. Yasuda, M. Yoshida, and Jr. K. Kinosita. Direct observation of the rotation of F_1-ATPase. *Nature*, 386:299–302, 1997.

[67] T. R. Strick, J.-F. Allemand, D. Bensimon, A. Bensimon, and V. Coquette. The elasticity of a single supercoiled DNA molecule. *Science*, 271:1835–1837, 1996.

[68] N. Nakamura, K. Hashimoto, and T. Matsunaga. Immunoassay method for the determination of immunoglobulin G using bacterial magnetic particles. *Anal. Chem.*, 63:268–272, 1991.

[69] E. M. Purcell. Life at low Reynolds number. *Am. J. Phys.*, 45:3–11, 1977.

[70] H. Risken. *The Fokker-Planck Equation: Methods of Solution and Applications.* Springer-Verlag, Berlin, 1989.

[71] M. Abramowitz and I. A. Stegun. *Handbook of Mathematical Functions.* Dover Publications, New York, 1972.

[72] N. G. van Kampen. The turning of magnetotactic bacteria. *J. Stat. Phys.*, 80:23–33, 1995.

[73] M. A. Martsenyuk, Yu. L. Raĭkher, and M. I. Shliomis. On the kinetics of magnetization of suspensions of ferromagnetic particles. *Sov. Phys.-JETP*, 38(2):413–416, 1974.

Ernest Orlando Lawrence Berkeley National Laboratory
One Cyclotron Road | Berkeley, California 94720

Prepared for the U.S. Department of Energy under Contract No. DE-AC03-76SF00098